

2008

The effect of convection and shear on the damping and propagation of pressure waves

Barry Vincent Kiel
University of Dayton

Follow this and additional works at: https://ecommons.udayton.edu/graduate_theses

Recommended Citation

Kiel, Barry Vincent, "The effect of convection and shear on the damping and propagation of pressure waves" (2008). *Graduate Theses and Dissertations*. 3916.
https://ecommons.udayton.edu/graduate_theses/3916

This Dissertation is brought to you for free and open access by the Theses and Dissertations at eCommons. It has been accepted for inclusion in Graduate Theses and Dissertations by an authorized administrator of eCommons. For more information, please contact mschlange1@udayton.edu, ecommons@udayton.edu.

THE EFFECT OF CONVECTION AND SHEAR ON THE DAMPING AND
PROPAGATION OF PRESSURE WAVES

Dissertation

Submitted to

The College of Engineering of the

UNIVERSITY OF DAYTON

in Partial Fulfillment of the Requirements for

The Degree

Doctor of Philosophy in Mechanical Engineering

by

Barry Vincent Kiel

UNIVERSITY OF DAYTON

Dayton, Ohio

August, 2008

APPROVED BY:



Ahmed R. Kashani, Ph.D.
Faculty Advisor



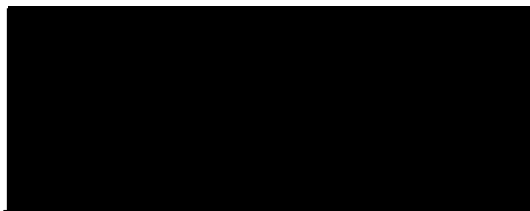
Youssef N. Raffoul, Ph.D.
Committee Member



Jamie S. Ervin, Ph.D.
Committee Member



John J. Schauer, Ph.D.
Committee Member



Kevin R. Hallinan, Ph.D.
Chair, Department of Mechanical Engineering

ABSTRACT

THE EFFECT OF CONVECTION AND SHEAR ON THE DAMPING AND PROPAGATION OF PRESSURE WAVES

Name: Kiel, Barry, V.
University of Dayton

Advisor: Dr A. Reza Kashani

Combustion instability is the positive feedback between heat release and pressure in a combustion system. Combustion instability occurs in the both air breathing and rocket propulsion devices, frequently resulting in high amplitude spinning waves. If unchecked, the resultant pressure fluctuations can cause significant damage. Models for the prediction of combustion instability typically include models for the heat release, the wave propagation and damping. Many wave propagation models for propulsion systems assume negligible flow, resulting in the wave equation.

In this research the effect of flow on wave propagation was studied both numerically and experimentally. Two experiential rigs were constructed, one with axial flow to study the longitudinal waves, the other with swirling flow to study circumferential waves. The rigs were excited with speakers and the resultant pressure was measured simultaneously at many locations. Models of the rig were also developed. Equations for wave propagation were derived from the Euler Equations. The resultant resembled the wave equation with three

additional terms, two for the effect of the convection and a one for the effect of shear of the mean flow on wave propagation.

From the experimental and numerical data several conclusions were made. First, convection and shear both act as damping on the wave propagation, reducing the magnitude of the Frequency Response Function and the resonant frequency of the modes. Second, the energy extracted from the mean flow as a result of turbulent shear for a given condition is frequency dependant, decreasing with increasing frequency. The damping of the modes, measured for the same shear flow, also decreased with frequency. Finally, the two convective terms cause the anti-nodes of the modes to no longer be stationary. For both the longitudinal and circumferential waves, the anti-nodes move through the domain even for mean flow Mach numbers less than 0.10. It was concluded that convection causes the spinning waves documented in inlets and exhausts of gas turbine engines, rocket combustion chambers, and afterburner chambers. As a result, the effects of shear must be included when modeling wave propagation, even for mean flows less than $< \text{Mach } 0.10$.

ACKNOWLEDGEMENTS

This research could not have occurred been completed without the direct and indirect support of many people. Thanks go to my advisor Dr. Reza Kashani for teaching me the ins and outs of acoustics modeling and experimentation. I would like to thank the Turbine Engine Division and Dr. Bill Copenhaver for the funding that enabled me to purchase the hardware and software that was vital to this research. I would also like to thank Dr. Robert Hancock and Mr. Carlos Arana for their patience and the latitude they gave me in relation to my schedule to ensure I had the time to complete the classes and research required to finish. I would like to thank Mr. Dale Shouse, Mr. Dwight Fox, Mr. Glen Boggs, Dr. Sivaram Gogineni, and Mr. Steve Pennington for supporting the procurement and fabrication of the experimental part of this research. Finally I would like to thank my family, Dawn and Nathan Kiel for persevering right along with me and my many long hours at the library and the laboratory.

TABLE OF CONTENTS

ABSTRACT	iii
ACKNOWLEDGEMENTS	v
I. INTRODUCTION	1
Motivation.....	1
Review of Acoustic Modeling and Experiments	6
Objective and Outline of the Research	12
II. WAVE PROPAGATION EQUATIONS WITH CONVECTION AND SHEAR	16
III. ANALYTICAL SOLUTIONS TO THE ONE-DIMENSIONAL WAVE PROPAGATION EQUATIONS	27
IV. NUMERICAL MODELS	29
COMSOL MULTIPHYSICS.....	29
Speaker/Driver Model.....	31
V. EXPERIMENTAL SETUP	36
Blower, Experimental Rigs, and Speaker/Driver.....	37
High Speed Pressure, Pitot Probe, and Hot Wire Measurements	43
Data Acquisition System, FRF, and Mode Shape Measurement.....	49
VI. TURBULENCE AND SHEAR	58
VII. RESULTS AND DISCUSSION	62
Frequency Response Function (FRF) Data.....	63
Mode Shapes	77
Damping From FRF Data	83
Correlation of Turbulence Data to Damping	90
Analytical Solutions in the Limit and Damping	93
Numerical and Experimental Transient Analysis	95
VIII. CONCLUSIONS AND RECOMMENDATIONS	137
Conclusions.....	137
Recommendations.....	140
BIBLIOGRAPHY	141
APPENDICES	146
Appendix 1. Conservation of Mass.....	146
Appendix 2. Conservation of Momentum	147
Appendix 3. Separation of Variables Solution to the Acoustic Wave Equation	149
Appendix 4. Derivation of the Solutions for the Damped Wave Equation	152
Appendix 5. Derivation of the Solutions for the Convective Wave Equation.....	155

LIST OF ILLUSTRATIONS

FIGURE 1-1. THERMOACOUSTICALLY EXCITED SPINNING MODE IN A MODEL ROCKET ENGINE EXPERIMENT (BIBIK ET AL, (2008))	4
FIGURE 1-2 MACH NUMBER DEPENDENCE OF PROPAGATING WAVE PRESSURE FOR A FORCED LONGITUDINAL WAVE (INGARD AND SINGHA (1973))	10
FIGURE 4-4 EXPERIMENTAL DRIVER SYSTEM.....	32
FIGURE 4-5 TRANSFER FUNCTION OF THE DRIVER ASSEMBLY	35
FIGURE 5-1 EXPERIMENTAL APPARATUS	36
FIGURE 5-2 BLOWER AND CONTROLLER.....	37
FIGURE 5-3 ALLEN BRADLEY CONTROLLER	38
FIGURE 5-4 LONGITUDINAL MODE EXPERIMENTAL RIGS.....	39
FIGURE 5-5 SIDE VIEW OF CIRCUMFERENTIAL RIG	40
FIGURE 5-6 CIRCUMFERENTIAL RIG WITH THERMOCOUPLE AND KULITE PRESSURED TRANSDUCERS	41
FIGURE 5-7 CLOSE-UP OF THE SWIRLER MOUNTED TO THE INLET FLANGE.....	41
FIGURE 5-8 CLOSE-UP VIEW OF SPEAKER/DRIVER RIG	42
FIGURE 5-9 SKETCH OF KULITE XTE HIGH SPEED PRESSURE TRANSDUCER.....	43
FIGURE 5-10 PITOT PROBE	45
FIGURE 5-11 CALIBRATION DATA FOR TSI 1210 HOT WIRE PROBES.....	49
FIGURE 5-12 SCXI CHASSIS AND SCXI DATA ACQUISITION CARDS.	51
FIGURE 5-13 EXAMPLE FRF CURVE	56
FIGURE 6-1 TURBULENT ENERGY SPECTRA (HINZE, 1987).....	59
FIGURE 7-1 FREQUENCY RESPONSE FUNCTION MAGNITUDE PLOT OF THE FIRST AND SECOND MODES OF THE LONGITUDINAL RIG MODELED USING COMSOL	65
FIGURE 7-2 FRF OF A SECOND ORDER DAMPED SYSTEM	66
FIGURE 7-1 FEA FRF AT THE CENTER PRESSURE NODE FOR INCREASING MACH NUMBER	67
FIGURE 7-4 FRF MAGNITUDE OF THE 1M BY 0.0158M (1/2 INCH) DIAMETER LONGITUDINAL RIG, MACH NUMBER = 0.0	69
FIGURE 7-5 FRF MAGNITUDE OF THE 1M BY 0.0158M (1/2 INCH) DIAMETER LONGITUDINAL RIG, MACH NUMBER = 0.10	69
FIGURE 7-7 FRF MAGNITUDE OF THE 1M BY 0.0158M (1/2 INCH) DIAMETER LONGITUDINAL RIG, MACH NUMBER = 0.30	70
FIGURE 7-8 FRF MAGNITUDE FOR THE CENTER TRANSDUCER OF THE 0.0504 METER (2 INCH) DIAMETER LONGITUDINAL RIG FOR A RANGE OF MACH NUMBERS	72
FIGURE 7-9 FRF MAGNITUDE OF THE CIRCUMFERENTIAL RIG WITH NO FLOW	73
FIGURE 7-11 FRF MAGNITUDE OF THE CIRCUMFERENTIAL RIG, FLOW = 0.05 KG/S	74
FIGURE 7-12 FRF MAGNITUDE OF THE CIRCUMFERENTIAL RIG, FLOW = 0.09 KG/S	75
FIGURE 7-13 FRF MAGNITUDE OF THE CIRCUMFERENTIAL RIG, FLOW = 0.13 KG/S	75
FIGURE 7-14 FEA MODE SHAPE OF THE FIRST MOD OF THE SPEAKER DRIVER.....	77
FIGURE 7-15 FEA MODE SHAPE OF THE SECOND MODE OF THE SPEAKER DRIVER	77
FIGURE 7-16 MODE SHAPE FOR THE LONGITUDINAL RIG, FIRST MODE	79

FIGURE 7-17 MODE SHAPE FOR THE LONGITUDINAL RIG, SECOND MODE	79
FIGURE 7-18 MODE SHAPE FOR THE LONGITUDINAL RIG, THIRD MODE	80
FIGURE 7-19 MODE SHAPE FOR THE LONGITUDINAL RIG, FOURTH MODE.....	80
FIGURE 7-20 MODE SHAPE FOR THE LONGITUDINAL RIG, FIFTH MODE	81
FIGURE 7-21 MODE SHAPE FOR THE SECOND THROUGH SEVENTH MODES OF THE CIRCUMFERENTIAL RIG WITHOUT FLOW	82
FIGURE 7-22 MODE SHAPE FOR THE CIRCUMFERENTIAL RIG, THIRD MODE.....	82
FIGURE 7-23 EXAMPLE CURVE FIT FOR 1 M LONG BY 0.0508 M DIAMETER EXPERIMENTAL RIG, MACH NUMBER = 0.10	84
FIGURE 7-24 RIG PRESSURE DROP VERSUS MACH NUMBER FOR THE THREE 1 METER LONG EXPERIMENTAL RIGS	86
FIGURE 7-25 RESONANT FREQUENCY VS. DAMPING RATIO FOR THE FIRST MODE OVER A RANGE OF MACH NUMBERS AND EXPERIMENTAL RIGS.....	87
FIGURE 7-26 RESONANT FREQUENCY VS. DAMPING RATIO FOR THE SECOND MODE OVER A RANGE OF MACH NUMBERS AND EXPERIMENTAL RIGS	87
FIGURE 7-27 RESONANT FREQUENCY VERSUS DAMPING COEFFICIENT FOR THE THIRD MODE OVER A RANGE OF MACH NUMBERS AND EXPERIMENTAL RIGS	88
FIGURE 7-28 RESONANT FREQUENCY VS. DAMPING COEFFICIENT FOR THE FOURTH MODE OVER A RANGE OF MACH NUMBERS AND EXPERIMENTAL RIGS	88
FIGURE 7-29 RESONANT FREQUENCY VS. DAMPING COEFFICIENT FOR THE FIFTH MODE OVER A RANGE OF MACH NUMBERS AND EXPERIMENTAL RIGS	89
FIGURE 7-30 TURBULENT KINETIC ENERGY (TKE) SPECTRUM FOR 1M LONG, 0.0508M (2 INCH) DIAMETER EXPERIMENTAL RIG	91
FIGURE 7-31 TURBULENT KINETIC ENERGY (TKE) SPECTRUM FOR 1M LONG, 0.0254M (1 INCH) DIAMETER EXPERIMENTAL RIG	91
FIGURE 7-32 TURBULENT KINETIC ENERGY (TKE) SPECTRUM FOR 1M LONG, 0.0158M (1/2 INCH) DIAMETER EXPERIMENTAL RIG	92
FIGURE 7-33 RESPONSE OF THE 1-D ACOUSTIC WAVE EQUATION, FIRST LONGITUDINAL MODE.....	100
FIGURE 7-34 TIME RESPONSE 1-D ACOUSTIC WAVE EQUATION, SECOND LONGITUDINAL MODE.....	103
FIGURE 7-35 TIME SERIES OF CONVECTIVE WAVE EQUATION FOR THE FIRST MODE, MACH NUMBER = 0.10.....	108
FIGURE 7-36 TIME SERIES OF CONVECTIVE WAVE EQUATION FOR THE SECOND MODE, MACH NUMBER = 0.10.....	112
FIGURE 7-37 EXPERIMENTAL TIME SERIES OF THE LONGITUDINAL RIG FOR THE FIRST MODE, MACH NUMBER = 0.10.....	117
FIGURE 7-38 EXPERIMENTAL TIME SERIES OF THE LONGITUDINAL RIG FOR THE SECOND MODE, MACH NUMBER = 0.10	120
FIGURE 7-39 EXPERIMENTAL TIME SERIES OF THE CIRCUMFERENTIAL RIG FOR THE FOURTH MODE WITH NO FLOW.....	124
FIGURE 7-40 FINITE ELEMENT MODEL OF THE CIRCUMFERENTIAL RIG, PLANE SLICE THROUGH THE SWIRLER	125
FIGURE 7-41 NUMERICAL TIME SERIES OF THE CIRCUMFERENTIAL RIG FOR THE FIRST CIRCUMFERENTIAL MODE (MODE 3), MACH NUMBER = 0.10	129

FIGURE 7-42 EXPERIMENTAL TIME SERIES OF THE CIRCUMFERENTIAL RIG FOR THE FIRST CIRCUMFERENTIAL MODE (MODE 4), BLOWER MASS FLOW OF 0.054 KG/S	132
FIGURE 7-43 EXPERIMENTAL TIME SERIES OF THE CIRCUMFERENTIAL RIG FOR THE FIRST CIRCUMFERENTIAL MODE (MODE 4), BLOWER MASS FLOW OF 0.090 KG/S	135

LIST OF TABLES

TABLE 7-1 DAMPING OF 1.0 M LONG, 0.0508M DIAMETER EXPERIMENTAL RIG.....	85
TABLE 7-2 DAMPING OF 1.0 M LONG, 0.0254 M DIAMETER EXPERIMENTAL RIG	85
TABLE 7-3 DAMPING OF 1.0 M LONG, 0.0158 M DIAMETER EXPERIMENTAL RIG	85

LIST OF SYMBOLS/ABBREVIATIONS

a	speed of sound
C_v	constant volume specific heat
C_p	constant pressure specific heat
d	total derivative
FEA	Finite Element Analysis
FRF	Frequency Response Function
i	current
M	Mach number
m	mass
ODE	Ordinary Differential Equation
p	pressure
PDE	Partial Differential Equation
q	volume velocity
R	empirical viscous constant
RTSI	Real Time System Integration
t	time dimension
T	temperature
TKE	Turbulent Kinetic Energy ($u'u'$)
u	avail velocity
v	transverse velocity
v	voltage
x	axial dimension
y	transverse position
γ	ratio of specific heat
δ	partial derivative
ρ	density
ω	frequency
ω_n	natural frequency
ω_d	resonant frequency
ζ	damping ratio
\bar{u}	mean velocity
u'	fluctuating velocity
\dot{m}	mass flow

I. INTRODUCTION

Motivation

Over the past 50 years combustion instabilities have been reported in all types of propulsion systems including rockets, scramjets and gas turbine combustors and augmenters (Lovett et al. (1999, 2005), Poinso et al. (1986), Dowling and Stow (2003), and Bibik et al. (2008)). The problem, though, is as old as engineering. In the Theory of Sound, Rayleigh (1945) discusses Higgins and his observation of the **"singing flame"** in 1777. In 1878 Rayleigh (1878) was the first to propose a phenomenological explanation of combustion instability. In his famous paper, Rayleigh described combustion instability as follows; **"If heat be periodically communicated to, and abstracted from, a mass of air vibrating in a cylinder bounded by a piston, the effect produced will depend upon the phase of the vibration at which the transfer of heat takes place. If heat be given to the air at the moment of greatest condensation or to be taken from it at the moment of greatest rarefaction, the vibration is encouraged. On the other hand, if heat be given at the moment of greatest rarefaction, or abstracted at the moment of greatest condensation, the vibration is discouraged"**.

Pressure fluctuations resulting from combustion instability can cause catastrophic loss of the engine in two ways. First, the fluctuating pressure acts as a forcing function to the structure of the engine system. As the peak magnitude grows, it can excite mechanical parts in the propulsion system causing them to fail. The failure of mechanical parts often results in catastrophic loss of the engine. Second, most combustion systems utilize cooled liners to protect internal parts in the engine from the tremendous heat load generated by combustion. In combustion systems with cooled liners, coolant (air) is forced through perforations in a metal liner. The flow rate of the coolant is a function of the pressure drop across the liner. Fluctuating chamber pressure causes cyclic changes in pressure drop across the liner which can drive excessive wall heat transfer. The result is excessive heat load to the liner and internal parts of the engine, causing these parts to operate well above their designed conditions. The excessive heat flux can result in failure of the wall structures and internal parts (Genda et al. (1993), Anderson et al. (1995), Lovett et al (2004)).

Another interesting aspect of combustion instabilities is the existence of spinning transverse waves. In standing waves the locations of the minimum/maximum/zero pressure are fixed in space. Unlike standing waves, spinning waves do not have fixed minimum/maximum/zero pressure locations. Instead these locations move in time. Spinning tangential waves have plagued rocket engine development since the 1950s (Bibik et al. (2008), Lubarski et al. (2008)). High performance turbofan gas turbine engines have been evolving since the early 1970s. The flow rate of high performance military gas turbine

engines has been increasing to achieve ever increasing thrust goals. To achieve the required flow rates, the radius of the engine has increased almost two fold. As a result, the frequencies of the tangential and radial modes have been decreasing with the trend of increasing radius (Lovett (2004)). From communications with the designers of the major manufacturers of afterburning gas turbine engines, spinning acoustic modes have become prevalent as the size of the engine has increased.

In their recent research at Georgia Institute for Technology, the group of engineers lead by Dr Benn Zinn has been able to replicate a spinning mode in a laboratory scale rig (Bibik (2008), Lubarski (2008)). Figure 1-1 is a series of images of the "severe tangential instability" captured in their research rig. The images detail clockwise rotation of the instability. These images correspond to bulk combustor swirl in the clockwise direction. In their research they were able to control the tangential instability through the use of active control and baffles. Combustion systems are not the only systems that suffer from spinning wave propagation modes. In the inlet and exhaust ducts of gas turbine engines the fan is a major source of organized sound and unorganized noise. This noise is known to excite spinning tangential modes in the inlet and exhaust ducts (Tyler and Sofrin (1963), Tam (1971), Nallasamy et al. (2000), and Zhang et al (2004)).

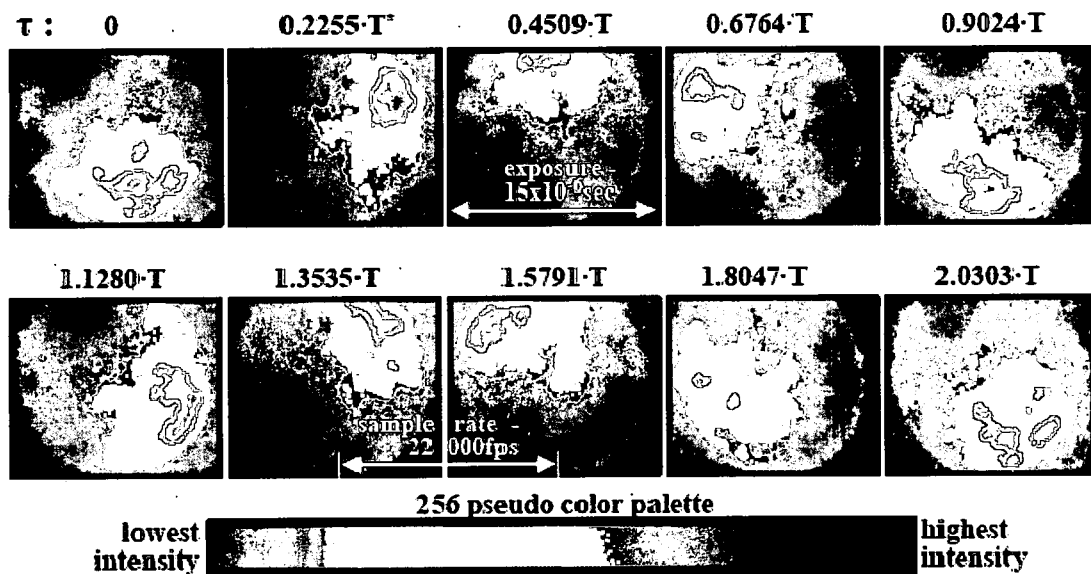


Figure 1-1. Thermo-acoustically Excited Spinning Mode in a Model Rocket Engine Experiment (Bibik et al, (2008))

During the development of high performance augmenters over the past 50 years the conditions in the augmenters have undergone radical changes, see Figure 1-1. In the 1950's and 1960's high performance gas turbine engines employed the turbojet cycle. Afterburners were quickly added to engines to improve takeoff thrust and increase the speed of the aircraft. In these engines the augmenters operated at relatively low Mach numbers, ~ 0.1 . To improve engine thrust to weight and specific fuel consumption the turbofan engine cycle was perfected for gas turbine engines. This advanced cycle as well as significant improvements in high temperature materials resulting in higher turbine exit temperatures and turbine exit Mach numbers. These conditions took the augmenters Mach numbers to ~ 0.3 , into the subsonic compressible range. Advances in technology in the 1980s pushed thrust to weight even higher while

further reducing specific fuel consumption. As a result turbine exit Mach number has increased further. Super-cruising high performance gas turbines typically have turbine exit Mach numbers ~ 0.4 . Future systems that would require hyper cruise and partial augmentation are expected to have even higher inlet Mach numbers to the augmenter, ~ 0.5 .

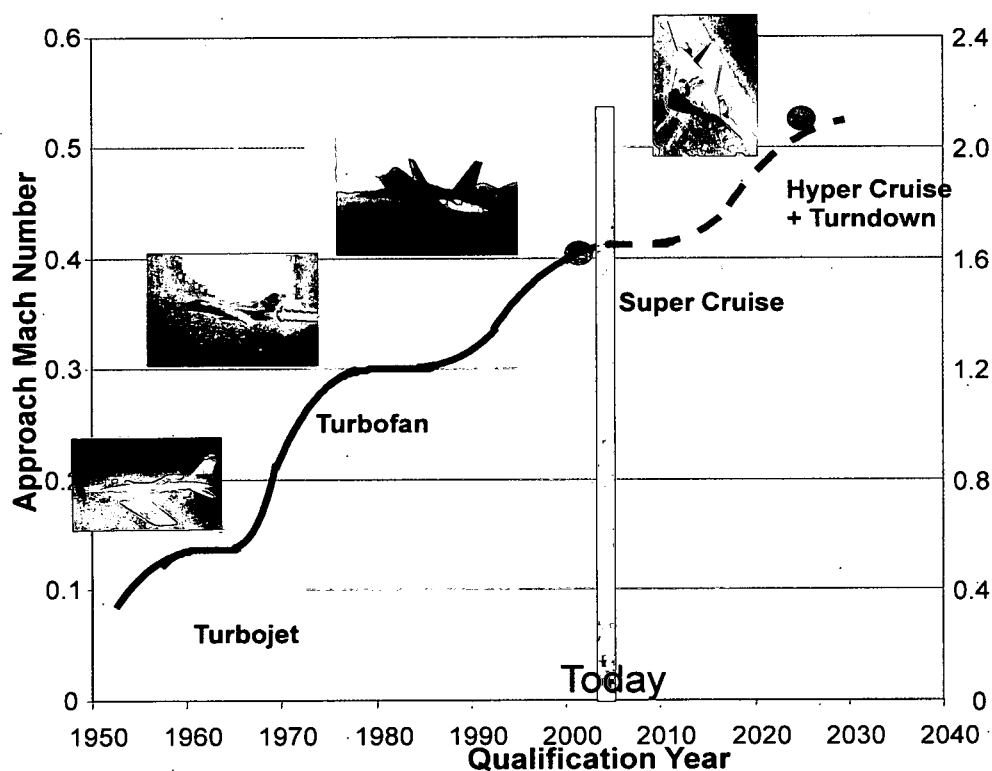


Figure 1-1 Changes in Augmenter Approach Mach Number for the Last 50 Years

Review of Acoustic Modeling and Experiments

For over 50 years several authors have been working in the area of acoustics and the effect of fluid motion on wave propagation. The research has been concentrated in two time periods. Early, in the 1960s and 1970s, there was a considerable body of work driven by the emerging gas turbine industry. The research studied sound propagation in inlet and exhaust ducts. Later in the 1990's and in this decade, a resurgence of study of wave propagation has occurred. This later research is centered around the study of wave propagation through large L/D ducts as applicable to catalytic converters. In each of these time periods, the research was comprised of two main areas. One area of research concentrated on the effect of the fluid motion on the propagation of upstream and downstream waves. In this research, a uniform or plug flow velocity profile was assumed. The second area of research focused on the effect of the boundary layer shear and liner or wall applications on wave propagation.

For actual duct flows in gas turbine engines and internal combustion engine applications, the walls of the duct have various treatments to reduce acoustic noise generation. These wall treatments and the shear flow at the wall effect the boundary conditions used to solve the governing equations. The effect of shear and wall treatments have been studied in depth over the past 40 years as well for both the gas turbine and internal combustion engine applications. Pridmore-Brown (1958) was the first to propose a sophisticated mathematical model for the effects of shear flow. In his research, Pridmore-Brown used

cylindrical coordinates and assumed steady fully developed flow with constant properties. In the transverse (denoted by r) direction, a velocity profile was assumed. From these assumptions Pridmore-Brown derived the wave equation:

$$\frac{\partial^2 p}{\partial t^2} + 2aM \frac{\partial^2 p}{\partial x \partial t} - a^2 (1 - M^2) \frac{\partial^2 p}{\partial x^2} - 2\rho \frac{\partial M_r}{\partial r} \frac{\partial v_r}{\partial z} = 0 \quad (1-1)$$

Acoustic flows with shear are sometimes called Pridmore-Brown flows and solutions to Equation 1-1 are sometimes called Pridmore-Brown solutions. The second and third terms in Equation 1-1 represent the effects of convection of the wave propagation. The last term in 1-1 represents the effect of the velocity profile or shear on the wave propagation.

In his work, Pridmore-Brown studied the effect of the shear layer on the downstream propagating wave. He concluded that shear has a dramatic effect on the attenuation across the spectrum of waves in a duct. He concluded that shear has little effect on the attenuation of plane waves at lower frequencies. This is not true, though, of the high frequency waves. In high frequency waves the shear layer acts to refract sound and concentrate it in the shear layer. Pridmore-Brown observed 100 db amplification of waves in the shear layer region at some conditions.

Many authors since Pridmore-Brown have studied the problem of shear and wall treatments on wave propagation. Hersh and Catton (1973) concluded that the frequency dependence noted by Pridmore-Brown was strongly

connected to the size of the developing boundary layer. They concluded that as the wave length of the pressure wave becomes smaller than the thickness of the boundary layer, the sound is refracted into the center of the duct. This refraction of the pressure waves with wave lengths smaller than the boundary layer thickness explains the increase of sound in the boundary layer. Following Hersh and Catton, several researchers have studied the problem of shear and various wall applications over the years, (Zaho and Morris (2005), Boucheron et al. (2005), Dokumaci (1995, 1998, 2002) Peate and Karthik et al. (2000) Kirby (1999), Gogate and Munjal (1992), Schauer (1978), Eversman (1971a), Mungar and Gladwell (1969), Mungar and Plumblee (1969) Cantrell et al. (1963)). In this body of research, the velocity profile at the wall and the wall boundary conditions are varied across a broad range to represent different acoustic applications. Each of these papers discusses the effect of acoustic applications on broadband attenuation. They all note the importance of the decreased attenuation of the downstream moving wave.

Several authors have studied the problem of wave propagation in ducts with uniform flow (Morse and Ingard (1968), Eversman (1970, 1971b), Ingard and Singhai (1973, 1974), Gogate and Munjal (1992), Dokumaci (1995)). In this research one-dimensional axial flow is assumed. The flow is considered to be steady, without shear, and having constant properties. These assumptions are made to make the problem both analytically and computationally tractable. The analysis begins with the continuity and momentum equations. The relationship between pressure and density is assumed to be isentropic, resulting in:

$$\partial p = a^2 \partial \rho \quad (1-2)$$

From this relationship and the governing equations the authors derive the wave Equation:

$$\frac{\partial^2 p}{\partial t^2} + a^2 M \frac{\partial^2 p}{\partial x \partial t} - a^2 (1 - M^2) \frac{\partial^2 p}{\partial x^2} = 0 \quad (1-3)$$

The effect of convection enters Equation 1-3 in both in the cross derivative of pressure term as well as with the scaling of wave speed by $(-M^2)$ on the pure spatial derivative.

In their research of wave propagation, Eversman (1970, 1971b) and Ingard and Singhal (1975) both show that the pressure waves take the form:

$$x > 0$$

$$p(x, t) = f\left(t + \frac{x}{1 + M}\right) \quad (1-4)$$

$$x < 0$$

$$p(x, t) = f\left(t + \frac{x}{1 - M}\right) \quad (1-5)$$

The waves travel at different speeds depending if they are traveling with or against the flow. Eversman concluded that the waves were "Doppler" shifted by the fluid motion. Eversman also showed that this Doppler shift in the wave

propagation causes a decrease in the attenuation of the wave propagating downstream, and an increase in the attenuation of the upstream wave. For Mach 0.5, there is a 30 percent increase in the frequency where the peak attenuation occurs.

Ingard and Singhai (1973, 1974) studied wave propagation in the presence of uniform flow, experimentally and analytically. In their research, they set up a tube with flow. The tube also had an acoustic source in the middle. Figure 1-2 depicts their analytical and experimental results. The flow was

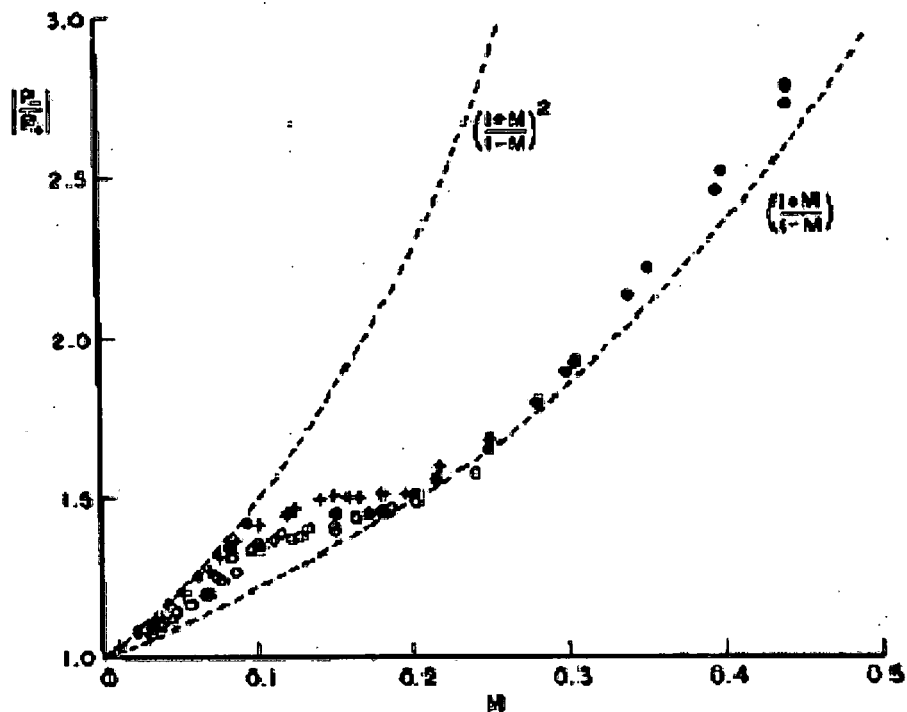


Figure 1-2 Mach Number Dependence of Propagating Wave Pressure for a Forced Longitudinal Wave (Ingard and Singha (1973))

driven with the source at a known frequency and the pressure along the upstream and downstream of the source were measured as a function of Mach number. They found that for flows with lower Mach < 0.1 the ratio followed the curve:

$$\frac{p_+}{p_i} = \frac{(1 + M)^2}{(1 - M)^2} \quad (1-6)$$

For higher Mach numbers, $M > 0.2$ the pressure ratio followed a different curve:

$$\frac{p_+}{p_i} = \frac{(1 + M)}{(1 - M)} \quad (1-7)$$

Between these two, the pressure ratio was approximately constant at a value of 1.5. Ingard and Singhai concluded that the condition of the source velocity produced these different results. For $M < 0.1$ the source air was assumed to have a laminar profile. For $M > 0.2$ the forced air was assumed to have a turbulent profile. Substituting either laminar or turbulent boundary conditions for forcing into the governing equations reproduced the asymptotic relationship seen in Figure 1-2. Thus, they determined that the propagation of the waves in a forced flow is sensitive to the boundary conditions of the source or driven flow.

Objective and Outline of the Research

It is not the intent of this research to model the complex behavior in the inlet, exhaust, main combustor, or augmentor of a gas turbine engine. The intent of this research is to better understand the phenomenological effect of flow on wave propagation in ducts similar to afterburners. Much experimental work was conducted to understand the phenomenology of wave propagation with mean flow by Ingard and Eversman in the 1970s. With the tools available to them at the time they were able to ascertain a much better understanding of the effect of flow. In their paper, Ingard and Singhal (1974) admit that with the instruments available that the accuracy of the measurement "is not particularly great". With the advent of high speed computers, high speed pressure and velocity measurement devices, and multi channel high speed data acquisition systems, the measurement quality has improved dramatically. From these improved data, this research attempts to better understand the nature of wave propagation in systems with flow. Unlike the previous studies, this research attempts to capture the effect of flow on the entire shape of longitudinal and transverse modes in both frequency and time domains.

In this research, the importance of the turbulent shear and its effect on damping were obtained by comparing the high speed pressure and turbulence data. It was found that turbulent shear causes the damping to be frequency dependant. It was also found that the trend in the frequency change was sometimes counter to intuition. In this research the importance of convection and

its effect on the movement of the minimum/maximum/zero of the pressure waves was also ascertained. Movement of the minimum/maximum/zero in the presence of convection was modeled and captured experimentally. The motion caused by convection is directly attributed to the spinning waves reported previously in the introduction. This finding is important, especially for combustion systems with low, $M < 0.1$, but appreciable flow. Ignoring the effects of convection and shear is ill advised when studying thermo acoustics in any combustion system with flow.

To this end, the dissertation is divided into 8 chapters. The second chapter is a description of the governing equations for wave propagation with flow. The conservation equations for mass and momentum are not derived in Chapter 2. The conservation equations are instead derived in Appendices 2 and 3. Chapter 2 utilizes the governing equations to formulate the governing equation(s) for wave propagation with flow. The governing equation(s) for wave propagation with flow include both the effects of shear and convection. For simplicity viscous effects are neglected.

Analytical solutions to the equations were derived in this research. Chapter 3 outlines the separation of variables approach to obtaining the analytical solutions for the acoustic wave equation, convective wave equation, and "damped" wave equation. The analytical solution to the "damped" wave equation is outlined in the text books by Denneweyer (1968) and Weinberg (1965). The solution to the damped wave equation is used to compare the effect of convection on wave propagation. The governing equations for wave

propagation were also used to construct numerical models. Chapter 4 outlines the numerical modeling approach. In this research the commercially available Finite Element Analysis (FEA) solver COMSOL Multiphysics was used for model solution.

Chapter 5 outlines the experimental approach for the research. Both a longitudinal and a circumferential rig were used in the research to study wave propagation. The layout of these rigs is described in Chapter 5. Also described in Chapter 5 are the various data acquisition techniques employed. A data acquisition system was constructed to obtain multiple channels of high speed pressure from pressure transducers and turbulent velocity data from hot wire measurements. Other channels were also required to obtain data for the estimation of experimental wave speed. A Pitot probe was also utilized to measure the flow velocity at the exit of the longitudinal rig. The data acquisition system was used to gather pressure and temperature data for the estimation of flow Mach number as a function of blower motor speed.

In Chapter 6 there is a brief discussion of turbulent shear. The point of this chapter is to introduce various concepts of turbulent flow. The chapter establishes a link between turbulent shear and energy extraction from the mean flow and acoustics. In the chapter it is argued that turbulence acts to convert kinetic energy from the mean flow and energy from the acoustics into turbulence kinetic energy. This "conversion" makes the energy "unavailable" to the mean flow and the acoustics. The result of turbulence is damped acoustic modes.

Chapter 7 discusses the many numerical and experimental results of the research. Initially frequency response function (FRF) and turbulence data are presented for the longitudinal and circumferential rigs. These data lend insight into the effect of flow (convection, shear, and viscosity) on the damping of the waves. The FRF data were compared to the turbulence spectrum obtained from the hot wire. The main conclusion from the FRF data was the turbulent spectrum extracts energy at different rates over the spectrum. The result is that damping from turbulence is not constant over the range of frequencies of interest. The FRF data also provide the frequencies for excitation of the resonant modes for time series analysis. In the second section of Chapter 7 the pressure time series data is presented from the models and experiments. The main conclusion from the time series data is that convection causes the wave propagation to change dramatically. It is proven numerically and experimentally that convection causes the anti-nodes of the wave propagation to move as a function of time. This motion is the spinning of the tangential waves mentioned earlier in this introductory chapter.

The final chapter is for discussion of the conclusions of the research and recommendations. After the last chapter the references are listed. Finally there are 5 appendices.

II. WAVE PROPAGATION EQUATIONS WITH CONVECTION AND SHEAR

An equation for the propagation of pressure waves can be derived using the conservation equations for mass and momentum with some assumptions applied. The derivation of the continuity and momentum equations is carried out in Appendices 2 and 3, respectively. The results from these Appendices are repeated here. Equation 2-1 is the continuity equation. Equations 2-2, and 2-3 are the x and y momentum equations. The last two terms in each of the momentum equation are the viscous terms. These terms are simply expressed here as the viscosity multiplied by a function, f_1 and f_2 , of the axial, u , and transverse, v , velocities.

$$\frac{\partial \rho}{\partial t} + \rho \frac{\partial u}{\partial x} + u \frac{\partial \rho}{\partial x} + \rho \frac{\partial v}{\partial x} + v \frac{\partial \rho}{\partial x} = 0 \quad (2-1)$$

$$\rho \frac{\partial u}{\partial t} + \rho u \frac{\partial u}{\partial x} + \rho v \frac{\partial u}{\partial y} = -\frac{\partial p}{\partial x} + \nu f_1(u, v) \quad (2-2)$$

$$\rho \frac{\partial v}{\partial t} + \rho u \frac{\partial v}{\partial x} + \rho v \frac{\partial v}{\partial y} = -\frac{\partial p}{\partial y} + \nu f_2(u, v) \quad (2-3)$$

The first assumption applied to the continuity and momentum equations is that the variables can be split into mean and fluctuating parts. The variables represented in this form are:

$$p = \bar{p} + p'$$

$$\rho = \bar{\rho} + \rho'$$

$$u = \bar{u} + u'$$

$$v = \bar{v} + v'$$

These are termed the perturbed variables. Substituting the perturbed variables into the continuity equation results in:

$$\begin{aligned} \frac{\partial(\bar{\rho} + \rho')}{\partial t} + (\bar{\rho} + \rho') \frac{\partial(\bar{u} + u')}{\partial x} + (\bar{u} + u') \frac{\partial(\bar{\rho} + \rho')}{\partial x} \\ + (\bar{\rho} + \rho') \frac{\partial(\bar{v} + v')}{\partial y} + (\bar{v} + v') \frac{\partial(\bar{\rho} + \rho')}{\partial x} = 0 \end{aligned} \quad (2-5)$$

Next several assumptions are made about the mean and fluctuating quantities. The experimental rig is a cylinder and is symmetric about any angle, theta. The mean flow is assumed to only be along the long axis of the cylinder. With the assumptions of symmetry and axial mean flow, statements can be made about the mean flow and derivatives of the mean flow.

$$\bar{u} = \bar{u}(y)$$

$$\frac{\partial \bar{u}}{\partial t} = \frac{\partial \bar{u}}{\partial x} = 0; \frac{\partial \bar{u}}{\partial y} \neq 0$$

$$\bar{v} = 0$$

$$\frac{\partial \bar{v}}{\partial x} = \frac{\partial \bar{v}}{\partial y} = \frac{\partial \bar{v}}{\partial t} = 0$$

The mean pressure and density are also assumed to be constant.

$$\bar{p} = C$$

$$\frac{\partial \bar{p}}{\partial x_i} = \frac{\partial \bar{p}}{\partial t} = 0$$

$$\bar{\rho} = C$$

$$\frac{\partial \bar{\rho}}{\partial x_i} = \frac{\partial \bar{\rho}}{\partial t} = 0$$

Finally, products of fluctuating quantities are assumed to be small.

$$a'b' = 0$$

$$a' \frac{\partial b'}{\partial x_i} = 0$$

Applying the above assumptions, Equation 2-5 takes the final form:

$$\frac{\partial \rho'}{\partial t} + \bar{\rho} \frac{\partial u'}{\partial x} + \bar{u} \frac{\partial \rho'}{\partial x} + \bar{\rho} \frac{\partial v'}{\partial y} = 0 \quad (2-6)$$

Substituting the perturbed variables into the x-momentum equation (Equation 2-2) results in:

$$\begin{aligned} & (\bar{\rho} + \rho') \frac{\partial (\bar{u} + u')}{\partial t} + (\bar{\rho} + \rho') (\bar{u} + u') \frac{\partial (\bar{u} + u')}{\partial x} + (\bar{\rho} + \rho') (\bar{v} + v') \frac{\partial (\bar{u} + u')}{\partial y} \\ & = - \frac{\partial (\bar{p} + p')}{\partial x} + \nu f_1(u, v) \end{aligned}$$

Applying the assumptions the x-momentum equation becomes:

$$\bar{\rho} \frac{\partial u'}{\partial t} + \bar{\rho} \bar{u} \frac{\partial u'}{\partial x} + \bar{\rho} \bar{v}' \frac{\partial \bar{u}}{\partial y} = - \frac{\partial p'}{\partial x} + \nu f_1(u, v) \quad (2-7)$$

Substituting the perturbed variables into the y-momentum equation (Equation 2-3) yields:

$$\begin{aligned}
& (\bar{\rho} + \rho') \frac{\partial(\bar{v} + v')}{\partial t} + (\bar{\rho} + \rho')(\bar{u} + u') \frac{\partial(\bar{v} + v')}{\partial x} + (\bar{\rho} + \rho')(\bar{v} + v') \frac{\partial(\bar{v} + v')}{\partial y} \\
& = -\frac{\partial(\bar{p} + p')}{\partial y} + \nu f_2(u, v)
\end{aligned}$$

Applying the assumptions results in:

$$\bar{\rho} \frac{\partial v'}{\partial t} + \bar{\rho} u \frac{\partial v'}{\partial x} = -\frac{\partial p'}{\partial y} + \nu f_2(u, v) \quad (2-8)$$

An equation that is second order in pressure can be derived from the governing equations. This equation represents the propagation of pressure waves in two-dimensions. Taking the derivative of equation 2-7 with respect to x results in

$$\bar{\rho} \frac{\partial^2 u'}{\partial t \partial x} + \bar{\rho} u \frac{\partial^2 u'}{\partial x^2} + \bar{\rho} \frac{\partial v'}{\partial x} \frac{\partial \bar{u}}{\partial y} = -\frac{\partial^2 p'}{\partial x^2} + \nu f_1'(u, v)$$

Solving for the second order cross derivative results in:

$$\bar{\rho} \frac{\partial^2 u'}{\partial t \partial x} = -\bar{\rho} u \frac{\partial^2 u'}{\partial x^2} - \bar{\rho} \frac{\partial v'}{\partial x} \frac{\partial \bar{u}}{\partial y} - \frac{\partial^2 p'}{\partial x^2} + \nu f_1'(u, v) \quad (2-9)$$

Taking the derivative of equation 2-8 with respect to y results in:

$$\bar{\rho} \frac{\partial^2 v'}{\partial t \partial y} + \bar{\rho} \frac{\partial \bar{u}}{\partial y} \frac{\partial v'}{\partial x} + \bar{\rho} u \frac{\partial^2 v'}{\partial x \partial y} = -\frac{\partial^2 p'}{\partial y^2} + \nu f_2'(u, v)$$

Solving for the second order cross derivative results in:

$$\bar{\rho} \frac{\partial^2 v'}{\partial t \partial y} = -\bar{\rho} \frac{\partial \bar{u}}{\partial y} \frac{\partial v'}{\partial x} - \bar{\rho} u \frac{\partial^2 v'}{\partial x \partial y} - \frac{\partial^2 p'}{\partial y^2} + \nu f_2'(u, v) \quad (2-10)$$

Taking the derivative of equation 2-6 with respect to time results in:

$$\frac{\partial^2 \rho'}{\partial t^2} + \bar{\rho} \frac{\partial^2 u'}{\partial x \partial t} + \bar{u} \frac{\partial^2 \rho'}{\partial x \partial t} + \bar{\rho} \frac{\partial^2 v'}{\partial y \partial t} = 0$$

Rearranging

$$\frac{\partial^2 \rho'}{\partial t^2} + \bar{u} \frac{\partial^2 \rho'}{\partial x \partial t} + \bar{\rho} \left[\frac{\partial^2 u'}{\partial x \partial t} + \frac{\partial^2 v'}{\partial y \partial t} \right] = 0 \quad (2-11)$$

Substituting Equations 2-9 and 2-10 into equation 2-11.

$$\begin{aligned} 0 = & \frac{\partial^2 \rho'}{\partial t^2} + \bar{u} \frac{\partial^2 \rho'}{\partial x \partial t} + \\ & \left(-\bar{\rho} u \frac{\partial^2 u'}{\partial x^2} - \bar{\rho} \frac{\partial v'}{\partial x} \frac{\partial \bar{u}}{\partial y} - \frac{\partial^2 p'}{\partial x^2} + v f_1'(u, v) \right) + \\ & \left(-\bar{\rho} \frac{\partial \bar{u}}{\partial y} \frac{\partial v'}{\partial x} - \bar{\rho} u \frac{\partial^2 v'}{\partial x \partial y} - \frac{\partial^2 p'}{\partial y^2} + v f_2'(u, v) \right) \end{aligned}$$

Rearranging

$$\begin{aligned} 0 = & \frac{\partial^2 \rho'}{\partial t^2} + \bar{u} \frac{\partial^2 \rho'}{\partial x \partial t} - 2\bar{\rho} \frac{\partial v'}{\partial x} \frac{\partial \bar{u}}{\partial y} - \left[\frac{\partial^2 p'}{\partial x^2} + \frac{\partial^2 p'}{\partial y^2} \right] - \\ & \bar{\rho} u \left(\frac{\partial^2 u'}{\partial x^2} + \frac{\partial^2 v'}{\partial x \partial y} \right) + v \left[f_1'(u, v) + f_2'(u, v) \right] \end{aligned}$$

Applying the chain rule to the 5th term:

$$\begin{aligned} 0 = & \frac{\partial^2 \rho'}{\partial t^2} + \bar{u} \frac{\partial^2 \rho'}{\partial x \partial t} - 2\bar{\rho} \frac{\partial v'}{\partial x} \frac{\partial \bar{u}}{\partial y} - \left[\frac{\partial^2 p'}{\partial x^2} + \frac{\partial^2 p'}{\partial y^2} \right] - \\ & \bar{\rho} u \frac{\partial \left(\frac{\partial u'}{\partial x} + \frac{\partial v'}{\partial y} \right)}{\partial x} + v \left[f_1'(u, v) + f_2'(u, v) \right] \end{aligned} \quad (2-12)$$

The fifth term in equation 2-12 is the derivative with respect to x of part of the flux term of the continuity equation. Rearranging Equation 2-6:

$$\bar{\rho} \left(\frac{\partial u'}{\partial x} + \frac{\partial v'}{\partial y} \right) = -\frac{\partial \rho'}{\partial t} - \bar{u} \frac{\partial \rho'}{\partial x} \quad (2-13)$$

Substituting Equation 2-13 into Equation 2-12 yields:

$$0 = \frac{\partial^2 \rho'}{\partial t^2} + \bar{u} \frac{\partial^2 \rho'}{\partial x \partial t} - 2\bar{\rho} \frac{\partial v'}{\partial x} \frac{\partial \bar{u}}{\partial y} - \left[\frac{\partial^2 p'}{\partial x^2} + \frac{\partial^2 p'}{\partial y^2} \right] + \bar{u} \frac{\partial \left(\frac{\partial \rho'}{\partial t} + \bar{u} \frac{\partial \rho'}{\partial x} \right)}{\partial x} + v \left[f_1'(u, v) + f_2'(u, v) \right]$$

Applying the chain rule to the fifth term:

$$0 = \frac{\partial^2 \rho'}{\partial t^2} + \bar{u} \frac{\partial^2 \rho'}{\partial x \partial t} - 2\bar{\rho} \frac{\partial v'}{\partial x} \frac{\partial \bar{u}}{\partial y} - \left[\frac{\partial^2 p'}{\partial x^2} + \frac{\partial^2 p'}{\partial y^2} \right] + \bar{u} \frac{\partial^2 \rho'}{\partial t \partial x} + \bar{u}^2 \frac{\partial^2 \rho'}{\partial x^2} + v \left[f_1'(u, v) + f_2'(u, v) \right]$$

Rearranging:

$$0 = \frac{\partial^2 \rho'}{\partial t^2} + 2\bar{u} \frac{\partial^2 \rho'}{\partial x \partial t} - \left[\frac{\partial^2 p'}{\partial x^2} + \bar{u}^2 \frac{\partial^2 \rho'}{\partial x^2} + \frac{\partial^2 p'}{\partial y^2} \right] - 2\bar{\rho} \frac{\partial v'}{\partial x} \frac{\partial \bar{u}}{\partial y} + v \left[f_1'(u, v) + f_2'(u, v) \right] \quad (2-14)$$

In Equation 2-14 there are terms for the fluctuating pressure, density, and velocity. There are also terms for the shear of the mean axial velocity in the y direction and for the viscous effects of the fluid. The density can be related to the

pressure through the energy equation. If the flow is assumed to be isentropic, thus in viscid, then the isentropic relationship for density and pressure can be used.

$$dp = a^2 d\rho \quad (2-15)$$

Applying Equation 2-15 to Equation 2-14 results in:

$$\begin{aligned} 0 = & \frac{\partial^2 p'}{\partial t^2} + 2\bar{u} \frac{\partial^2 p'}{\partial x \partial t} - a^2 \left[\frac{\partial^2 p'}{\partial x^2} + \frac{\bar{u}^2}{a^2} \frac{\partial^2 p'}{\partial x^2} + \frac{\partial^2 p'}{\partial y^2} \right] \\ & - 2\bar{\rho}a^2 \frac{\partial v'}{\partial x} \frac{\partial \bar{u}}{\partial y} \end{aligned} \quad (2-16)$$

Previously we defined the axial mean velocity as variable in the y direction. The mean axial velocity is further defined in terms of Mach number by:

$$\bar{u}(y) = aM(y) \quad (2-17)$$

Substituting Equation 2-17 into Equation 2-16 results in the final equation for wave propagation is two-dimensions. This matches the equations derived by Mungar and Plumlee (1969).

$$\begin{aligned} & \frac{\partial^2 p'}{\partial t^2} + 2M(y)a \frac{\partial^2 p'}{\partial x \partial t} - a^2 [1 - M(y)^2] \frac{\partial^2 p'}{\partial x^2} \\ & - a^2 \frac{\partial^2 p'}{\partial y^2} - 2\bar{\rho}a^3 \frac{\partial v'}{\partial x} \frac{\partial M(y)}{\partial y} = 0 \end{aligned} \quad (2-18)$$

Examining the two-dimensional wave propagation equation there are a variety of terms that represent the effect of the flow on wave propagation. In Equation 2-18 there are two terms with Mach number that represent the effect of convection on the wave propagation:

$$2M(y)a \frac{\partial^2 p'}{\partial x \partial t}$$

$$M(y)^2 \frac{\partial^2 p'}{\partial x^2}$$

The last term in Equation 2-18 has the derivative of the mean axial flow with respect to the y-axis. In flows with solid boundaries the no slip condition at the boundary causes a boundary layer to form. As the flow develops the boundary layer grows. In the case of flows in a cylinder the boundary layer will eventually merge in the center of the cylinder. At this point the flow is considered fully developed. At any axial location the mean axial flow will vary across the cylinder. The derivative of the axial velocity with respect to the adverse axis, the y axis, is defined as the shear. Thus the last term in Equation 2-18 is the contribution of shear on the wave propagation.

$$2\bar{\rho}a^3 \frac{\partial v'}{\partial x} \frac{\partial M(y)}{\partial y}$$

For the case of no axial flow Equation 2-18 reduces to the acoustic wave equation.

$$\frac{\partial^2 p'}{\partial t^2} - a^2 \frac{\partial^2 p'}{\partial x^2} = 0 \quad (2-19)$$

If one-dimensional constant axial flow is assumed, the convective wave equation results:

$$\frac{\partial^2 p'}{\partial t^2} + 2Ma \frac{\partial^2 p'}{\partial x \partial t} - a^2 [1 - M^2] \frac{\partial^2 p'}{\partial x^2} = 0 \quad (2-20)$$

If the axial Mach number is small, but there is appreciable shear then Equation 2-18 reduces to the wave equation with shear:

$$\frac{\partial^2 p'}{\partial t^2} - a^2 \frac{\partial^2 p'}{\partial x^2} - a^2 \frac{\partial^2 p'}{\partial y^2} - 2\bar{\rho}a^3 \frac{\partial v'}{\partial x} \frac{\partial M}{\partial y} = 0 \quad (2-21)$$

In this research the effect of both the convection and shear terms will be studied to varying degree to ascertain the effect of each of these components of flow on wave propagation.

In the Results and Discussion Chapter, analytical solutions of the various wave equations will be discussed. Comparisons of the time response of the damped and convective wave equations will be made to illustrate that convection acts like damping. The derivation of the damped wave equation is required for this comparison. Starting with the continuity and x-momentum equations previously expressed, Equation 2-6 and 2-7 repeated here:

$$\frac{\partial \rho'}{\partial t} + \bar{\rho} \frac{\partial u'}{\partial x} + \bar{u} \frac{\partial \rho'}{\partial x} + \bar{\rho} \frac{\partial v'}{\partial y} = 0 \quad (2-6)$$

$$\bar{\rho} \frac{\partial u'}{\partial t} + \bar{\rho} \bar{u} \frac{\partial u'}{\partial x} + \bar{\rho} v' \frac{\partial \bar{u}}{\partial y} = -\frac{\partial p'}{\partial x} + \nu f_1(u, v) \quad (2-7)$$

Equations 2-6 and 2-7 can be reduced to one dimension by assuming no mean velocity and only axial acoustic velocity and pressure. According to White (1986), viscous drag is a function of a fluids Reynolds number. For a fluid with constant property the viscous drag is related to the fluid velocity. The damping associated with fluid viscosity, the f_1 term in the momentum equation, is modeled

by an empirical constant, R , multiplied by the acoustic velocity. With these assumptions Equations 2-6 and 2-7 become:

$$\frac{\partial \rho'}{\partial t} + \bar{\rho} \frac{\partial u'}{\partial x} = 0 \quad (2-22)$$

$$\bar{\rho} \frac{\partial u'}{\partial t} = -\frac{\partial p'}{\partial x} - Ru' \quad (2-23)$$

Assuming the viscous effects are small, then the isentropic relationship between pressure and density, Equation 2-15, stands and Equation 2-22 becomes

$$\frac{\partial p'}{\partial t} + a^2 \bar{\rho} \frac{\partial u'}{\partial x} = 0 \quad (2-24)$$

To obtain a second order PDE in terms of pressure, the derivative of Equation 2-24 with respect to time and the derivative of Equation 2-23 with respect to x of are obtained.

$$\frac{\partial^2 p'}{\partial t^2} + \bar{\rho} a^2 \frac{\partial^2 u'}{\partial x \partial t} = 0 \quad (2-25)$$

$$\bar{\rho} \frac{\partial^2 u'}{\partial t \partial x} = -\frac{\partial^2 p'}{\partial x^2} - R \frac{\partial u'}{\partial x} \quad (2-26)$$

From equation 2-24, the spatial derivative of velocity can be related to the temporal derivative of pressure by

$$\frac{\partial u'}{\partial x} = -\frac{1}{a^2 \bar{\rho}} \frac{\partial p'}{\partial t} \quad (2-27)$$

Substituting Equation 2-27 into Equation 2-26 results in:

$$\bar{\rho} \frac{\partial^2 u'}{\partial t \partial x} = -\frac{\partial^2 p'}{\partial x^2} + \frac{R}{a^2 \bar{\rho}} \frac{\partial p'}{\partial t} \quad (2-28)$$

Substituting Equation 2-28 into Equation 2-25 yields the damped wave equation:

$$\frac{\partial^2 p'}{\partial t^2} - a^2 \frac{\partial^2 p'}{\partial x^2} + \frac{R}{\bar{\rho}} \frac{\partial p'}{\partial t} = 0 \quad (2-29)$$

III. ANALYTICAL SOLUTIONS TO THE ONE-DIMENSIONAL WAVE PROPAGATION EQUATIONS

In Chapter 2 many forms of the second order wave equation were derived. A variety of assumptions about the axial flow resulted in various forms of the wave equation, Equations 2-19 – 2-21. The damped wave equation (Equation 2-29) was also derived. In Appendices 3 through 5, the analytical solutions to the one-dimensional acoustic wave equation, the one-dimensional convective wave equation, and the one-dimensional damped wave equation were obtained using the separation of variables method. In this chapter, the analytical solutions are listed. The analytical solutions will be used in Chapter 7 to help understand the phenomenological effect of convection on the propagation of waves.

Three analytical solutions are presented in this chapter. The second order PDE in pressure derived from the governing equations in Chapter 2 (Equation 2-18) is repeated here:

$$\frac{\partial^2 p'}{\partial t^2} + 2Ma \frac{\partial^2 p'}{\partial x \partial t} - a^2 [1 - M^2] \frac{\partial^2 p'}{\partial x^2} - a^2 \frac{\partial^2 p'}{\partial y^2} - 2\bar{\rho}a^3 \frac{\partial v'}{\partial x} \frac{\partial M}{\partial y} = 0 \quad (2-18)$$

As in Chapter 2, if no flow is assumed, the Mach number can be set to zero.

With this assumption, equation 2-18 reduces to:

$$\frac{\partial^2 p}{\partial t^2} - a^2 \frac{\partial^2 p}{\partial x^2} = 0 \quad (2-19)$$

Analytical solutions to Equation 2-19 were derived in Appendix 3. The analytical solution to Equation 2-19 is given as:

$$p_n(x, t) = \sin(\pm k_n x) [A_n \cos(\pm \omega_n t) + B_n \sin(\pm \omega_n t)] \quad (\text{A3-12})$$

As in Chapter 2, the damped wave equation was derived assuming damping was a function of the acoustic velocity. Equation 2-29 is repeated here:

$$\frac{\partial^2 p'}{\partial t^2} - a^2 \frac{\partial^2 p'}{\partial x^2} + \frac{R}{\rho} \frac{\partial p'}{\partial t} = 0 \quad (\text{2-29})$$

Analytical solution to the damped wave equation (Appendix 4) is:

$$p(x, t) = e^{-R_2 t} \sin(\pm k_n x) \left[A_n \cos\left(\pm \omega_n \left(1 - \frac{R_2^2}{\omega_n^2}\right) t\right) + B_n \sin\left(\pm \omega_n \left(1 - \frac{R_2^2}{\omega_n^2}\right) t\right) \right] \quad (\text{A5-16})$$

Finally, as in Chapter 2 if only the convective terms are considered, Equation 2-20 results:

$$\frac{\partial^2 p'}{\partial t^2} + 2Ma \frac{\partial^2 p'}{\partial x \partial t} - a^2 [1 - M^2] \frac{\partial^2 p'}{\partial x^2} = 0 \quad (\text{2-20})$$

The solution for Equation 2-20 (Appendix 5) is:

$$p(x, t) = A_1 e^{\omega_n (1-M^2)t + k_n (1+M)x} + A_2 e^{\omega_n (1-M^2)t - k_n (1-M)x} \quad (\text{A5-10})$$

IV. NUMERICAL MODELS

In Chapter 2 the PDEs for pressure and velocity were combined resulting in a single PDE that is a functions of pressure only. In Chapter 3 the analytical solutions for various forms the wave equations were given. In this chapter, several numerical models for the study of the wave propagation will be developed in three sections. In the first section the application of the finite element analysis (FEA) tool COMSOL Multiphysics will be developed. The second section contains models for the electrical, mechanical, and enclosure portions of the speakers. These models will be utilized in Chapter 7 to separate the effects of convection and shear on wave propagation by modeling each effect individually.

COMSOL MULTIPHYSICS

COMSOL Multiphysics is a commercially available three-dimensional Finite Element (FEA) package that was used to numerically model the various experimental sections. COMSOL is a very flexible package. COMSOL has many application modes; Acoustics, Diffusion, Electromagnetics, Heat Transfer, Fluid Dynamics, Structural Mechanics, Deformed Mesh, PDE Mode, and Classical PDEs. In each of these modes, the PDEs for the physical model and

select boundary conditions are already derived and ready for use. COMSOL also contains a mesh generation package in the main Graphical User Interface. With this tool geometries can be created, or imported from various computer aided design packages and meshed with hexagonal or tetrahedral meshes. Within the Acoustics Mode of COMSOL Multiphysics the acoustic wave equation and boundary conditions are available for immediate use. The governing equations for wave propagation with flow are much more complicated than the acoustic wave equation, and are not readily available in COMSOL. COMSOL has the ability to solve user defined PDEs using the PDE solvers within COMSOL. User provided PDEs can take three forms: Coefficient Form, General Form, and Weak Form. In the Coefficient Form, the PDEs have constant coefficients. In the weak form, the PDEs can contain models with mixed time and spatial derivatives. This is ideal for wave propagation with shear and convection, which has derivatives of space and time. In the weak form, the three first order governing equations can be used.

$$\frac{\partial p'}{\partial t} + aM(y)\frac{\partial p'}{\partial x} + \bar{\rho}a^2\left(\frac{\partial v'}{\partial y} + \frac{\partial u'}{\partial x}\right) = 0 \quad (4-1)$$

$$\bar{\rho}\frac{\partial u'}{\partial t} + \bar{\rho}aM(y)\frac{\partial u'}{\partial x} + a\bar{\rho}v'\frac{\partial M(y)}{\partial y} = -\frac{\partial p'}{\partial x} \quad (4-2)$$

$$\bar{\rho}\frac{\partial v'}{\partial t} + \bar{\rho}aM(y)\frac{\partial v'}{\partial x} = -\frac{\partial p'}{\partial y} \quad (4-3)$$

In the weak form, the second order PDE for pressure and the y momentum equation can also be used.

$$\frac{\partial^2 p'}{\partial t^2} + 2M(y)a \frac{\partial^2 p'}{\partial x \partial t} - a^2 [1 - M(y)^2] \frac{\partial^2 p'}{\partial x^2} - a^2 \frac{\partial^2 p'}{\partial y^2} - 2\bar{\rho}a^3 \frac{\partial v'}{\partial x} \frac{\partial M(y)}{\partial y} = 0 \quad (4-4)$$

$$\bar{\rho} \frac{\partial v'}{\partial t} + \bar{\rho}aM(y) \frac{\partial v'}{\partial x} = -\frac{\partial p'}{\partial y} \quad (4-3)$$

COMSOL has many analysis tools built into the Graphical User Interface.

In this research, the transient analysis, modal analysis, and frequency response analysis types were used. The transient analysis type tool allows for full transient analysis of the model in time domain. The modal analysis type tool solves for the modes of the model. The frequency response analysis type tool performs Frequency Response Function analysis of user defined inputs and outputs. The frequency response analysis type tool obtains and plots the Frequency Response Function magnitude and phase.

Speaker/Driver Model

Speakers are used in the experimental portion of this research to obtain the response of the one-dimensional system. A driver was constructed combining four speakers with a rear and front enclosure. The driver for the experiment has a rear enclosure common to all 4 speakers (Figure 4-4). All four speakers play into a common front enclosure. On one end, the common enclosure is attached to the experimental section with a flange. The opposite end of the volume is open to the atmosphere.

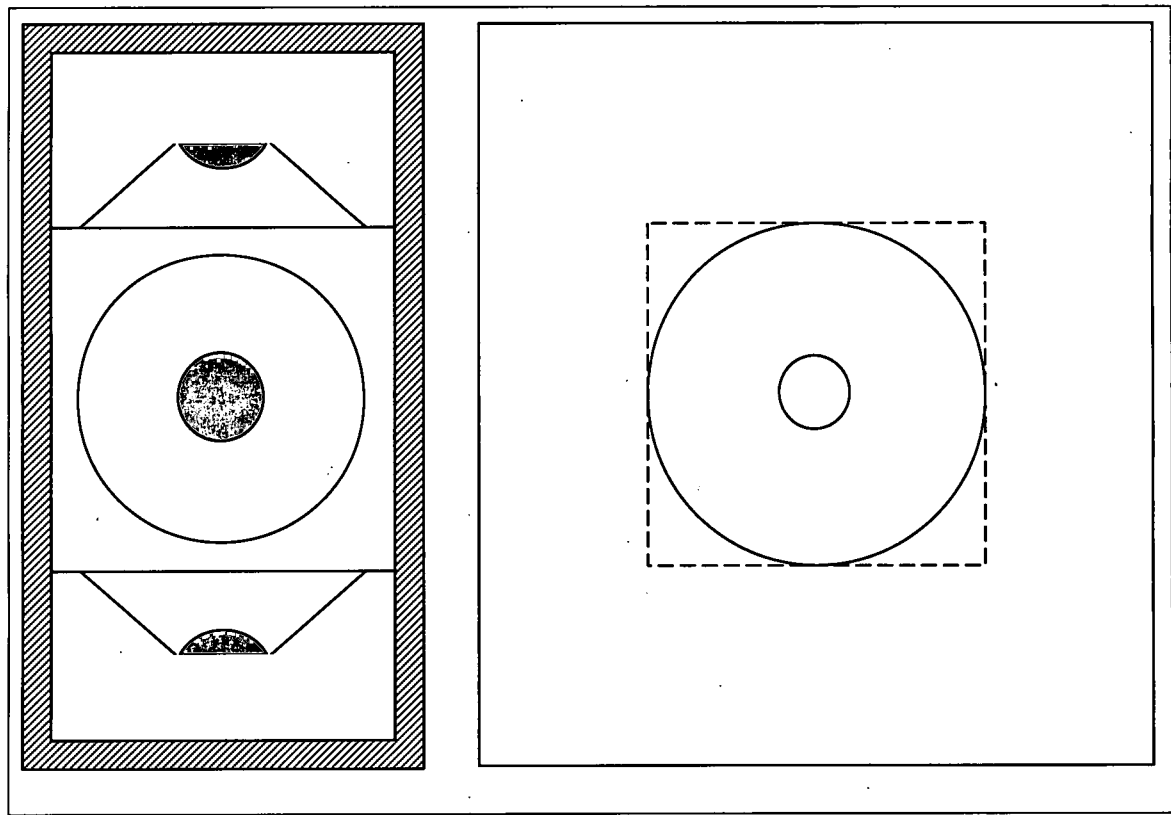


Figure 4-4 Experimental Driver System

In the experiments Frequency Response Functions were obtained by the data acquisition system. The response was of the speaker voltage as the input and the pressure measured by the Kulite as the output. To ensure a one to one comparison of the experimental data and model results a numerical model of the speaker physics was constructed. The model was used in COMSOL.

The input of the speaker model is the voltage supplied to the speaker coil. The output of the model is the pressure in the center of the common volume shared by all of the speakers in the speaker driver. The electrical and mechanical portions of the speaker are modeled with two governing equations. Equation 4-40 is the equation for the electrical portion of the speaker. Equation

4-40 relates the voltage applied to the speaker to the current in the coil and displacement of the speaker cone:

$$v = R_e i + L_e \frac{di}{dt} + K_e \frac{dx}{dt} \quad (4-40)$$

In equation 4-40, R_e is the resistance of the voice coil, L_e is the inductance of the voice coil and K_e is the back emf gain. The mechanical portion of the speaker can be modeled with a spring, mass, and damper system, Equation 4-41.

$$F - P_c A_s^* = m_s \frac{d^2 x}{dt^2} + b_s \frac{dx}{dt} + K_s x \quad (4-41)$$

In equation 4-41 P_c is the pressure in the common volume of the front enclosure. A_s^* is the effective area of the speaker piston. m_s are the mass of the speaker cone. b_s is the damping coefficient of the speaker cone. K_s are the stiffness of the speaker cone and the added stiffness of the finite enclosure behind the speaker. The force generated by the speaker is related to the current of the coil by the force gain constant K_f . Substituting, Equation 4-41 becomes:

$$K_f i - P_c A_s^* = m_s \frac{d^2 x}{dt^2} + b_s \frac{dx}{dt} + K_s x \quad (4-42)$$

Both Equations 4-40 and 4-42 can be represented as a transfer function. Taking the Laplace Transform of each equation results in:

$$V(s) = R_e I(s) + L_e s I(s) + K_e s X(s) \quad (4-43)$$

$$K_f I(s) - P_c(s) A_s^* = m_s s^2 X(s) + b_s s X(s) + K_s X(s) \quad (4-44)$$

The front enclosure of the speaker can be modeled using a lumped parameter model. Two equations can be written for the front enclosure. The first is an equation for the change in pressure in the front enclosure:

$$\frac{dP_c}{dt} = \frac{1}{C_c}(q_s - q_n) \quad (4-45)$$

Where C_c is the compliance of the front enclosure. The second is an equation relates the pressure drop across the neck to the flow through the neck:

$$(P_c - P_\infty) = I_n \frac{dq_n}{dt} + R_n q_n \quad (4-46)$$

Where I_n is the inertance of the neck and R_n is the resistance in the neck. In Equations 4-45 and 4-46 the compliance, inertance and resistance can be related to the geometry of the enclosure and neck by:

$$I_n = \frac{\rho L_{neck}}{A_{neck}}$$

$$C_n = \frac{V_{enclosure}}{\rho a^2}$$

$$R_n \approx 5000$$

Both Equations 4-45 and 4-46 can be represented as a transfer function. Taking the Laplace Transform of each results in:

$$P_c(s)s = \frac{1}{C_c}(Q_s(s) - Q_n(s)) \quad (4-36)$$

$$(P_c(s) - P_\infty(s)) = I_n s Q_n(s) + R_n Q_n(s) \quad (4-37)$$

Figure 4-5 is the SIMULINK transfer function model of the entire speaker driver.

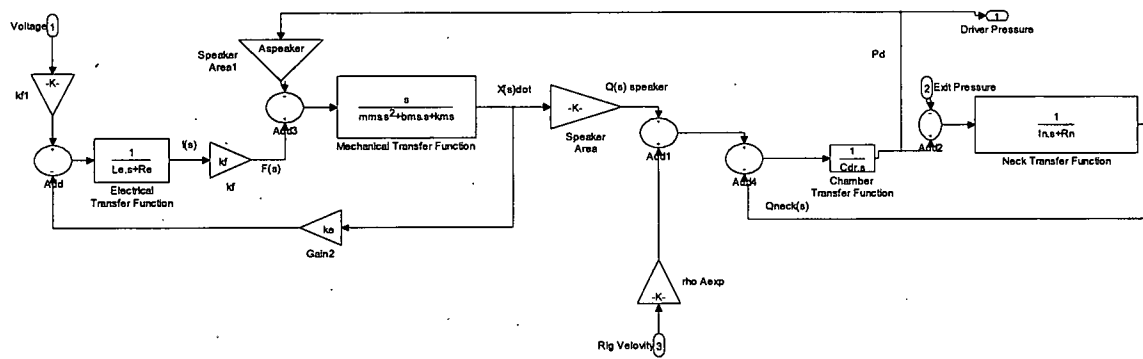


Figure 4-5 Transfer Function of the Driver Assembly

V. EXPERIMENTAL SETUP

The experimental apparatus (Figure 5-1) consists of four components, the blower and controller, the experimental rig, the speaker driver, and the data acquisition (DAQ) system. Two types of experimental rigs were used in the research, longitudinal and circumferential. The longitudinal rig was used to study the effect of axial flow on the longitudinal modes. The circumferential rig was used to study the effect of swirling flow on circumferential modes. A speaker/driver portion was mounted to the end the experimental rigs to excite the modes of the experimental rigs. Last the data acquisition system was assembled capable of performing simultaneous analog input and output.

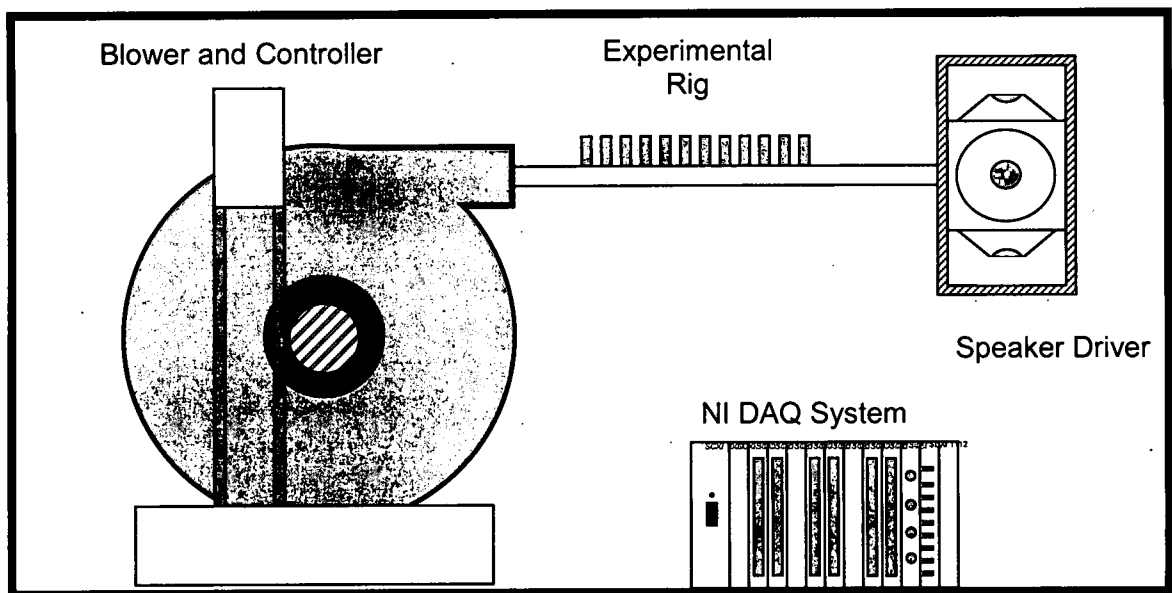


Figure 5-1 Experimental Apparatus

Blower, Experimental Rigs, and Speaker/Driver

Figure 5-2 is a picture of the blower. This part of the apparatus includes the blower and motor controller. The blower consists of a centrifugal fan in a composite housing. The fan is connected to a 7.5 horsepower 3 phase motor. Together, the fan and motor were capable of producing mass flow in excess of 0.25 Kg/m^3 at pressures up to 1250 Pa gauge. An Allen Bradley Powerline 70 motor control was attached to the blower power supply (Figure 5-3). The controller allows for control of the blower's fan motor. The speed of the motor was varied in order to change the velocity in the experimental rig.

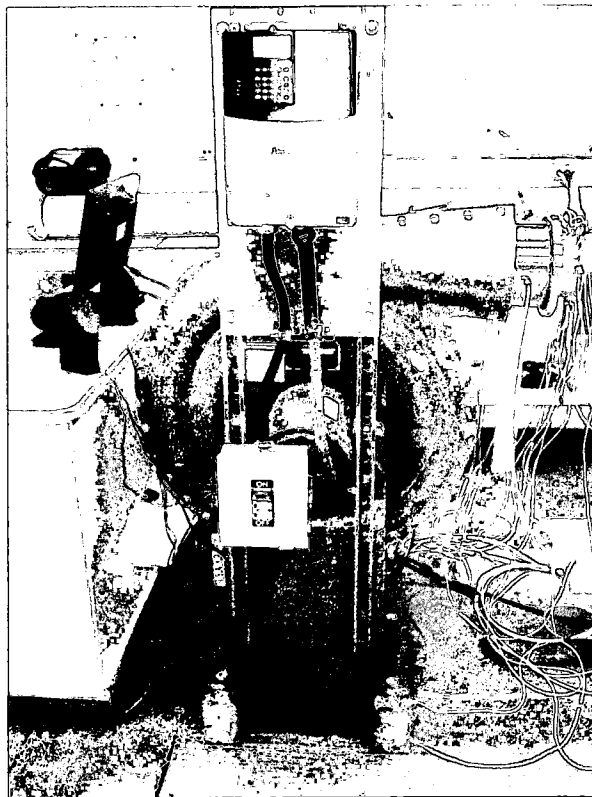


Figure 5-2 Blower and Controller

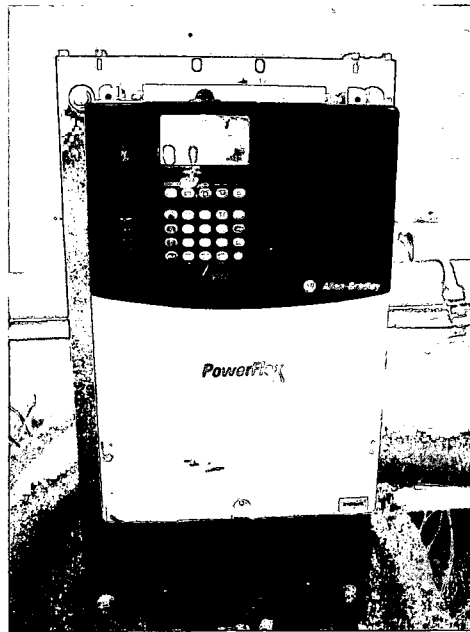


Figure 5-3 Allen Bradley Controller

Two different types of experimental rigs were used in the research. Separate rigs were constructed to study the longitudinal modes and the circumferential modes. The longitudinal rigs were constructed from one meter long schedule 40 PVC pipe. Three nominal diameters were used: $\frac{1}{2}$, 1, and 2 inches. The actual diameters in meters were: 0.0158 (1/2 inch nominal), 0.0254 (1 inch nominal), and 0.0508 (2 inches nominal). Attached to the pipes were 15 Kulite pressure transducers. The transducers were all mounted at the same axial location on all three of the experimental rigs. The transducers were placed 2.5, 5, 10, 15, 20, 22, 24, 26, 28, 30, 32, 34, 36, 38, and 39 inches from the inlet of the rigs. Figure 5-4 depicts the three longitudinal experimental rigs.

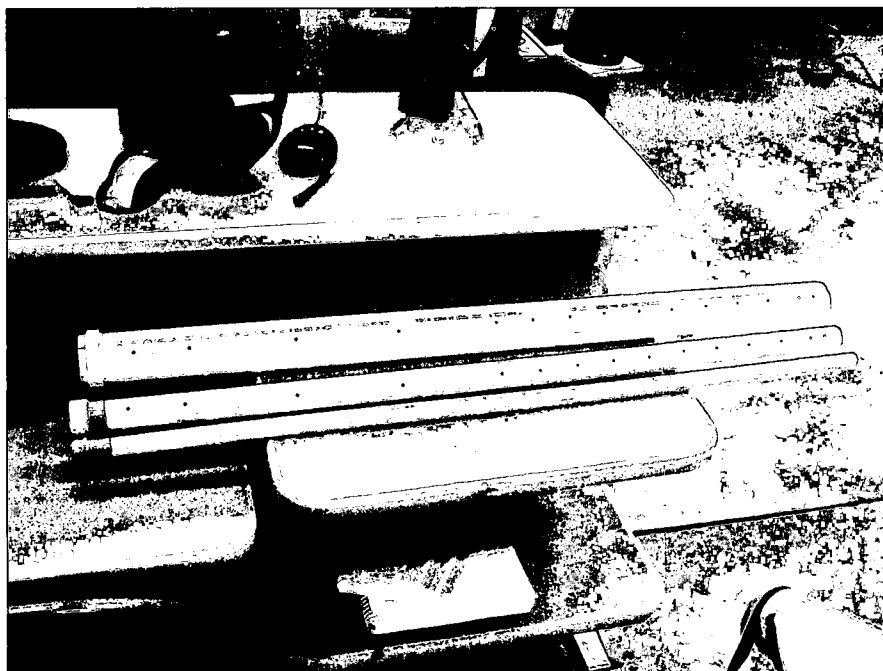


Figure 5-4 Longitudinal Mode Experimental Rigs

The circumferential rig was fabricated from 4 parts: blower plenum, inlet flange, outer tube, and swirler. Figures 5-5 through 5-7 depict the circumferential experimental rig. The blower plenum was fabricated to fit into the opening of the exit of the blower. The outer tube was fabricated to be 0.140 meters (5.5 inches) in diameter, and 0.254 meters (10 inches) long. The outer tube is connected to the blower plenum by the inlet flange. All of these features are clearly visible and marked in Figure 5-5.

Figure 5-6 is a close-up of the interior of the outer tube. Note that the swirler is mounted to the inlet flange that separates the circumferential rig from the blower. Figure 5-7 is a close-up of the swirler with the outer tube removed. The slots in the swirler are cut at a 30 degree angle relative to a tangent line at the surface of the swirler. The slots causing the flow to swirl as it exits the

swirler. The swirling air then turns axially and flows down the inside of the outer tube of the experimental rig. 15 Kulite pressure transducers were affixed around the perimeter of the rig. They were placed 0.0508 meters (2 inches) from the inlet flange. The transducers were placed at 0, 30, 60, 90, 120, 150, 180, 210, 225, 240, 270, 300, 315, and 330 degrees around the circumference. The location of the thermocouple and Kulite transducers can be seen in Figures 5-5, and 5-6.

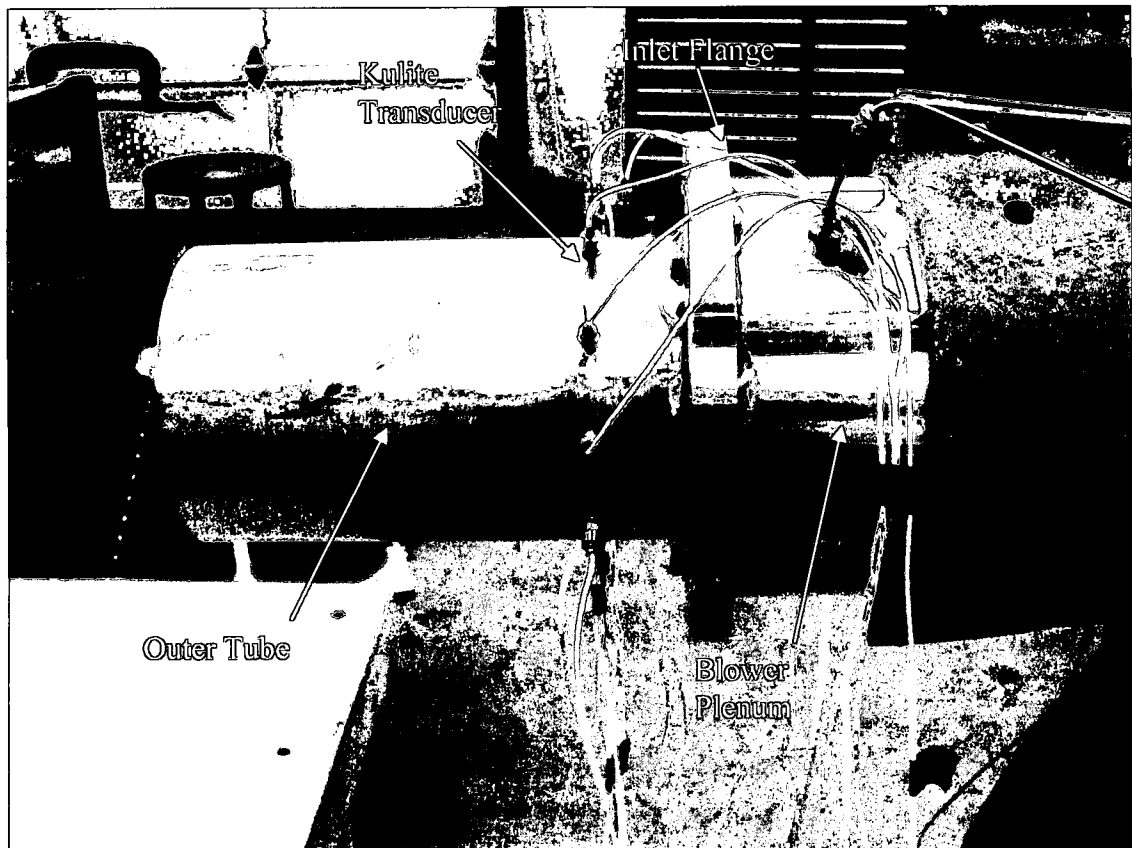


Figure 5-5 Side View of Circumferential Rig



Figure 5-6 Circumferential Rig with Thermocouple and Kulite Pressured Transducers

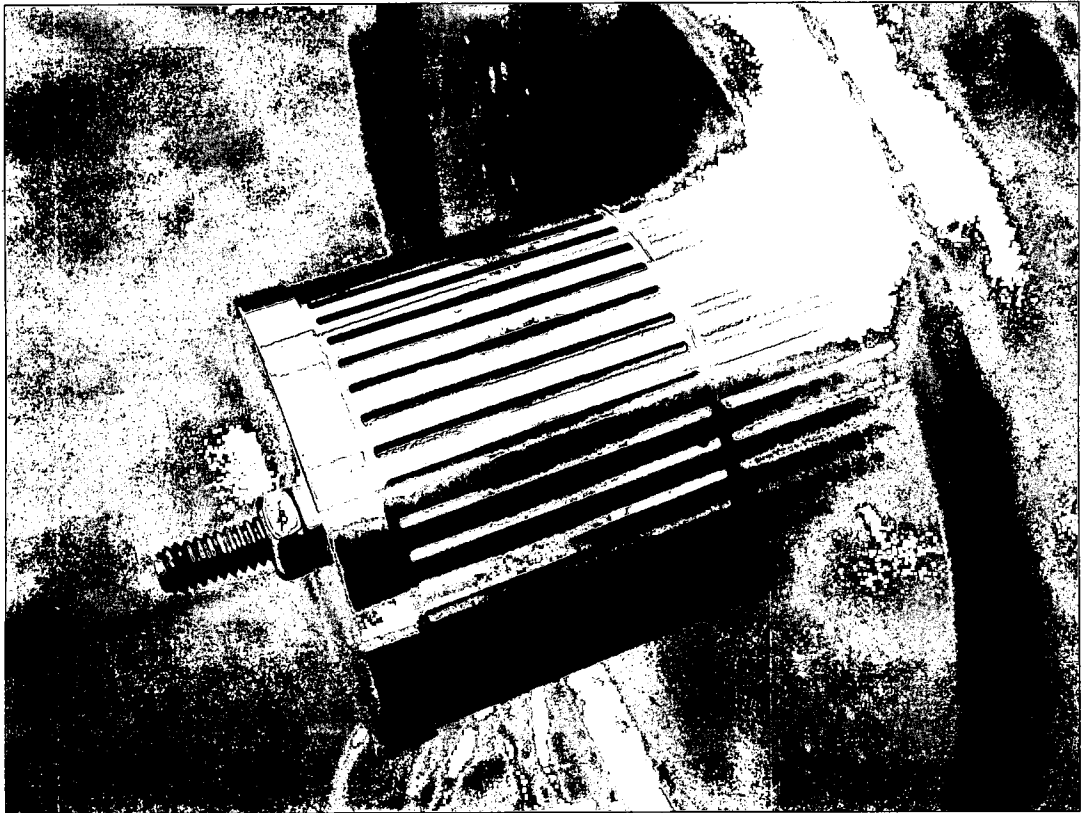


Figure 5-7 Close-up of the Swirler mounted to the Inlet Flange

In Chapter 4 the speaker/driver model was described. The speaker driver was constructed of four speakers and plywood (Figures 4-4 and 5-8). A cube with a dimension of 0.203 meters was constructed. 0.125 meter diameter holes were cut into all six sides of the cube. Speakers were mounted facing each other on 4 faces of the cube. The remaining two holes act as the inlet and exit of the speaker driver. Wooden flanges were constructed to accept the exit ends of the various experimental rigs into the inlet portion of the driver housing.

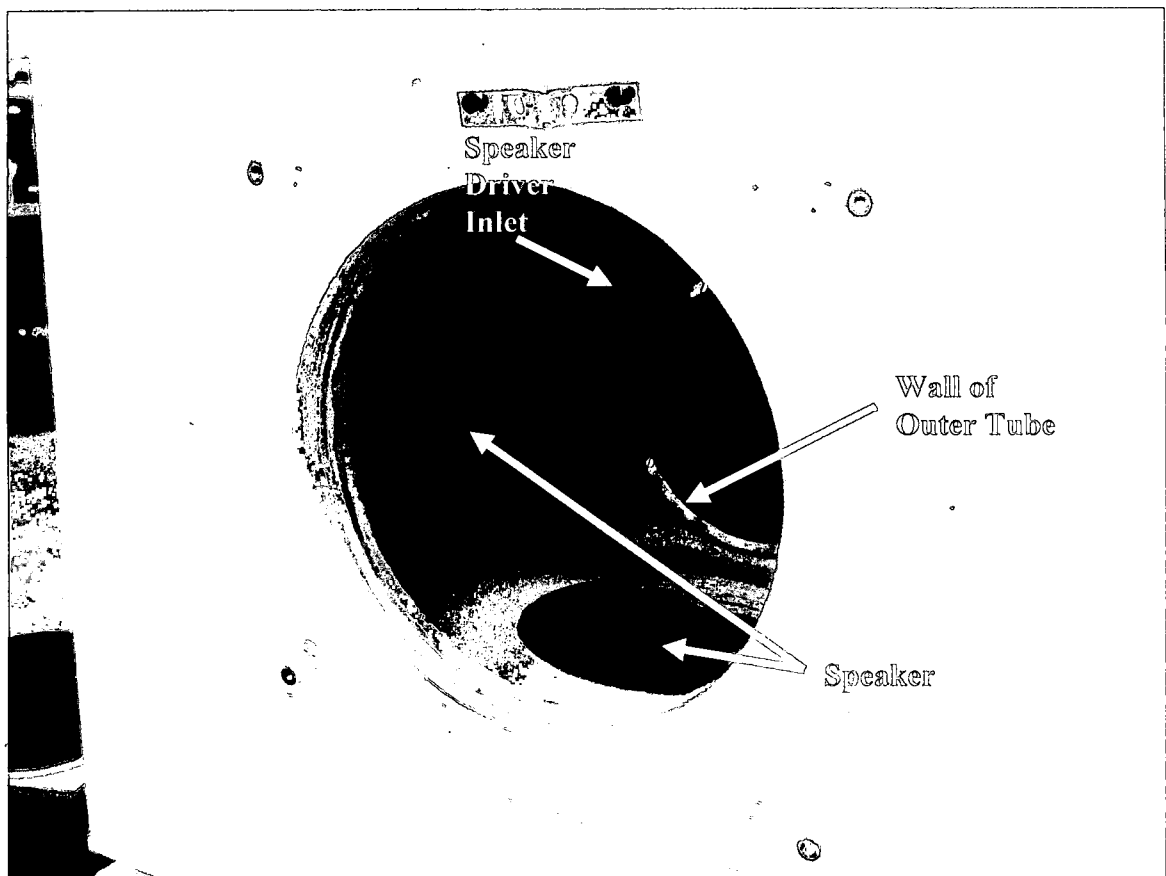


Figure 5- 8 Close-up view of Speaker/Driver Rig

High Speed Pressure, Pitot Probe, and Hot Wire Measurements

Several variables were measured during the experiments. The temperature in the blower plenum was measured for calculation of wave speed. The pressure drop across the experimental rig was measured as an estimate of the viscous losses. The static pressure and total head were measured for Pitot probe velocity measurement. Fluctuating pressure in the experimental rig was measured to calculate the FRF and mode shapes.

To measure the fluctuating pressure along the experimental rigs, high speed pressure Kulite XTE and XTC pressure transducers were used. Figure 5-9 is a sketch of a Kulite XTE high speed pressure transducer. The pressure transducers used in the experiment were 5 psi differential transducers with 0.01% full scale accuracy. The transducers are capable of 40 kHz operation. 10 volt excitation was provided by a National Instruments SCXI 1121 Isolated Universal Input Module.

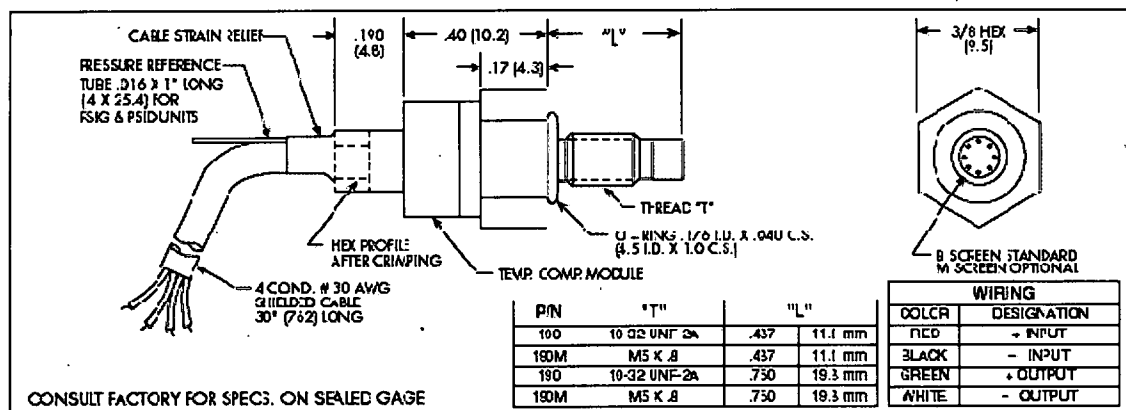


Figure 5-9 Sketch of Kulite XTE High Speed Pressure Transducer

The dark holes along the longitudinal experimental rigs in Figure 5-4 are the location of each of the transducers. For the longitudinal rigs, a total of 15 transducers were used. Some of the transducers were specifically placed where the maxima/antinode of the first five longitudinal modes was expected. All of the acoustic modes are symmetric about the center of the experimental rig. Because of a limited number of transducers the symmetry was used. More transducers were placed evenly on the right half of the experimental rigs. Figure 5-7 depicts the location of the transducers on the circumferential experimental rig. A transducer was placed at the top of the experimental rig, 2 inches from the wall separating the blower plenum from the experimental rig. Subsequent transducers were placed in the same axial plane every 30 degrees. Transducers were also placed at the 225, and 315 degree. A total of 14 transducers were used.

In the experiment, the velocity in the experimental rig was varied to ascertain the effect of flow on the wave propagation in the experimental rig. The velocity was measured using a Pitot probe (Figure 5-10). Total pressure was measured with a Serta 5 psi differential pressure transducer. The static pressure was measured with an Omega 15 psi absolute pressure transducer. The temperature of the air was measured with a K type thermocouple that was inserted in the flow at the exit of the experimental rig.

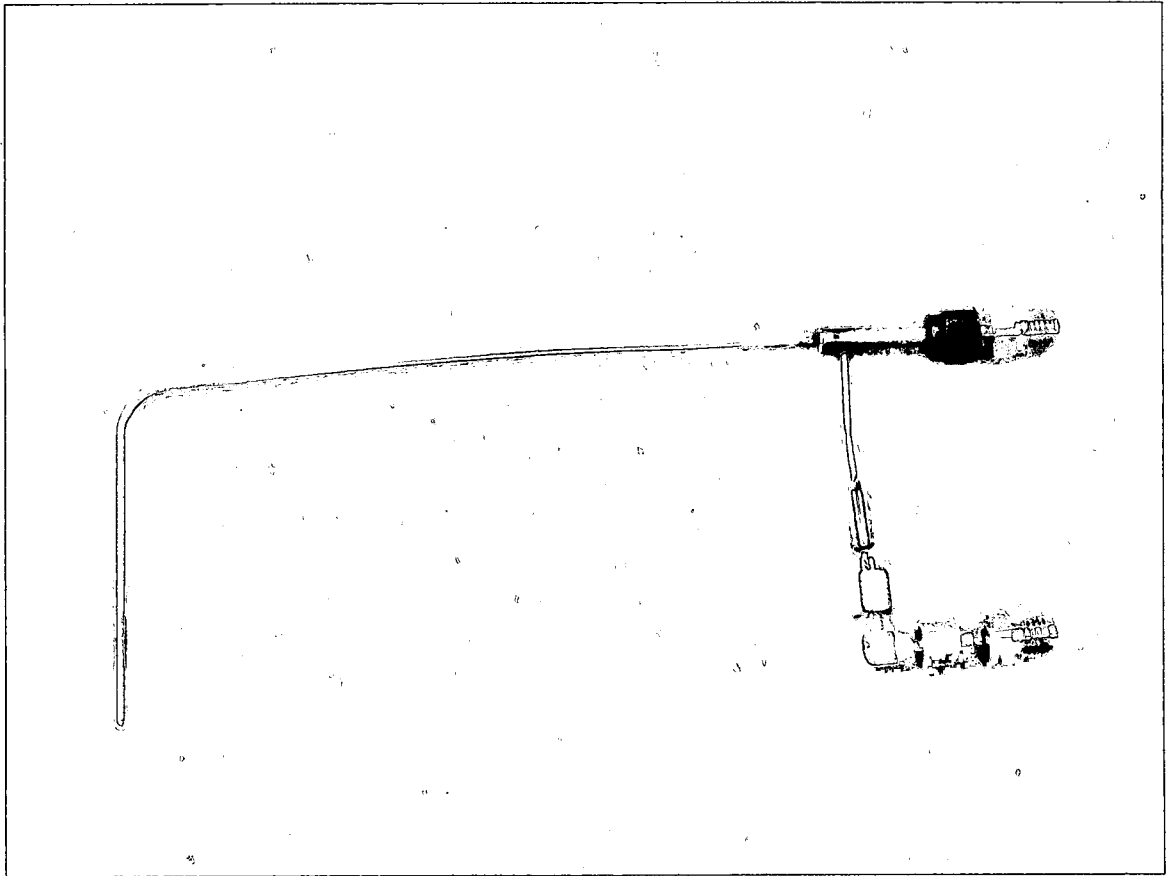


Figure 5-10 Pitot Probe

The velocity of the flow was calculated from the differential pressure and the static pressure using the compressible relations for the Pitot Probe (Equation 5-1).

$$M = \sqrt{2 \frac{\left(\frac{p_{static} + \Delta p}{p_{static}} \right)^{\frac{\gamma-1}{\gamma}} - 1}{\gamma - 1}} \quad (5-1)$$

In equation 5-1, P_{static} is the static pressure, and Δp is the differential pressure.

The total temperature and total wave speed are given as:

$$T_0 = T \left(1 + \frac{\gamma - 1}{2} M^2 \right) \quad (5-2)$$

$$a_0 = (\gamma R T_0) \quad (5-3)$$

The wave speed is defined as:

$$a = a_0 \left(\frac{1}{1 + \left(\frac{\gamma - 1}{2} \right) M^2} \right)^{0.5} \quad (5-4)$$

The velocity measured by the Pitot probe is simply the product of Equations 5-1 and 5-4.

To measure the magnitude of the fluctuating velocity a TSI Model 1210 hot wire sensor was used at the end of the experimental rig. The hot wire was used in conjunction with an IFA 100 anemometer. The TSI 1210 has a single cylindrical platinum fiber that is maintained at a constant temperature by the IFA 100 anemometer. For a heated cylinder in cross-flow, the heat transfer from the cylinder is a function of the Reynolds number of the flow over the cylinder. The Nusselt number (Equation 5-5) is a dimensionless number representing the average temperature gradient at the surface of the heated cylinder. In Equation 5-5, h is the convection coefficient, k is the thermal conductivity of the air, and L is the cylinder diameter.

$$Nu = \frac{hL}{k} \quad (5-5)$$

Hilpert's derived an empirical correlation (Incorporera and DeWitt, 1985) for constant temperature cylinders in cross-flow, Equation 5-6. The correlation relates the Nusselt Number to the Reynolds and Prandlt Numbers. For a

$$Nu_D = C Re_D^m Pr^{1/3} \quad (5-6)$$

For a constant temperature wire, the heat transfer is a function of the current applied to the film by the anemometer.

$$I_w^2 R_w = h A_w (T_w - T_\infty) \quad (5-7)$$

Where the voltage of the wire is:

$$V_w = I_w R_w \quad (5-8)$$

Solving for h:

$$h = \frac{V_w^2}{R_w \pi D_w L_w (T_w - T_\infty)} \quad (5-9)$$

From Equation 5-5, Nusselt number is:

$$Nu_w = \frac{V_w^2}{R_w \pi D_w L_w k_w (T_w - T_\infty)} \quad (5-10)$$

The anemometer controls the probe voltage through a bridge circuit. For a bridge circuit, the voltage is related to current by

$$V_b = I_w (R_w + R_c) \quad (5-11)$$

$$V_b = \left(\frac{V_w}{R_w} \right) (R_w + R_c) \quad (5-12)$$

$$V_w = \frac{V_b R_w}{R_w + R_c} \quad (5-13)$$

Substituting, the Nusselt Number becomes

$$Nu_D = \frac{V_b^2 R_f^2}{(R_f + R_c)^2 \pi L_f k_f (T_f - T_\infty)} \quad (5-14)$$

In Equation (5-14) the Nusselt number is a function of the square of the bridge voltage of the anemometer.

Combining Equations (5-6) and (5-14), the Reynolds Number of the wire is a function of the square of the bridge voltage of the anemometer, Equation 5-15. Each hot wire was calibrated using the Pitot probe. Mean velocity magnitude was measured with the Pitot Probe for all three experimental rigs over a range of blower settings. At the same time, the hot wire probe was placed in the flow and the bridge voltage was recorded. The hot wire Reynolds number and the square of the bridge voltage were calculated for each condition. These data were then plotted for each hot wire over the range of velocities tested. Figure 5-11 depicts the Reynolds number calibration for the hot wire probes available for the experiment.

$$Re^m = f(V_b^2) \quad (5-15)$$

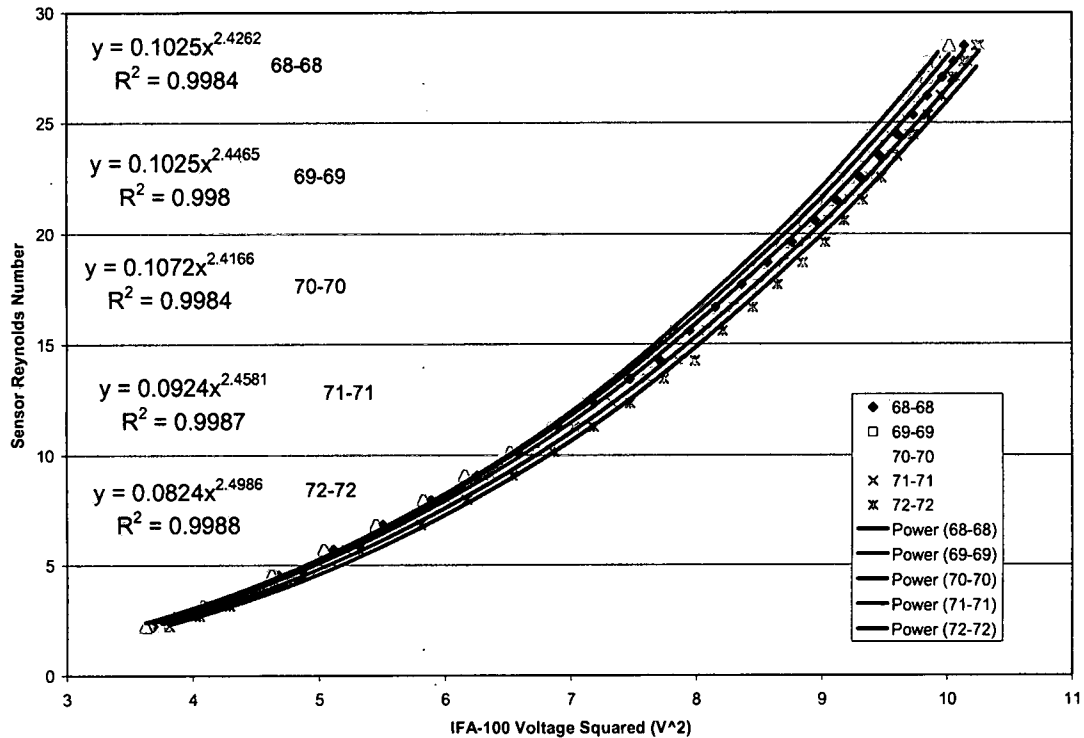


Figure 5-11 Calibration Data for TSI 1210 Hot Wire Probes

Data Acquisition System, FRF, and Mode Shape Measurement

The objective of the experimental portion of the research was to discern the effect of fluid motion on the wave propagation of a one-dimensional duct. In the experiment the FRF of the pressure signal at each transducer was obtained for a known voltage signal applied to the speaker driver. The FRF were gathered as the Mach numbers in the experimental rig was increased. To obtain the FRF, a data acquisition system was required that could both create a known signal and measure the effect of that signal on the pressure fluctuations in the experimental rig. The data acquisition system requires both an analog output and input

capabilities. The system also required precise timing between the output signal and the pressure response. A data acquisition system was constructed using National Instruments hardware and LabVIEW software. The hardware system consists of three components, a data acquisition (DAQ) board, an analog output board, and an SCXI chassis containing several analog input boards. Special cabling was used to daisy chain the various boards together to enable simultaneous analog output and input.

The DAQ board is the heart of the data acquisition system. An M-series NI 6280 multi-function DAQ board was installed in a personal computer. The board is capable of 18 bit resolution. The board also has a maximum sampling rate of 625 kHz. 16 channel analog input channels were also located on the board. The analog input channels were not utilized on the board. Instead, the board was linked to an SCXI 1000 chassis with several analog input boards. This was done to enable multi channel simultaneous sampling.

The NI 6280 Multifunction DAQ board does not have internal analog output channels. A separate NI 6733 analog output board was utilized for this purpose. The board has 8 analog output channels. Each channel has a maximum ± 10 volt output and 1 MHz output rate. The board also has 16 bit resolution. The NI 6733 board was then connected through a cable to a BNC-2110 accessory. The output from the BNC-2110 was routed to the speaker/driver through an external 200 watt rms amplifier with a BNC cable. The NI 6733 board was also connected directly to the NI 6280 DAQ board with a Real Time System Integration (RTSI) cable across the common RTSI bus.

Analog input was not accomplished on the DAQ board. Instead, a SCXI Chassis was configured with several analog input boards. The SCXI 1000 housed three SCXI 1140 eight Channel Simultaneous-Sampling Analog Input Modules. The chassis also housed six; four channel SCXI 1121 Isolated Universal Input Modules. Figure 5-12 is a photo of the SCXI chassis with boards installed. A combination of the 1140 and 1121 hardware and software enabled up to 24 channel simultaneous sampling. The chassis also housed a SCXI 1112 Thermocouple Input Module board.

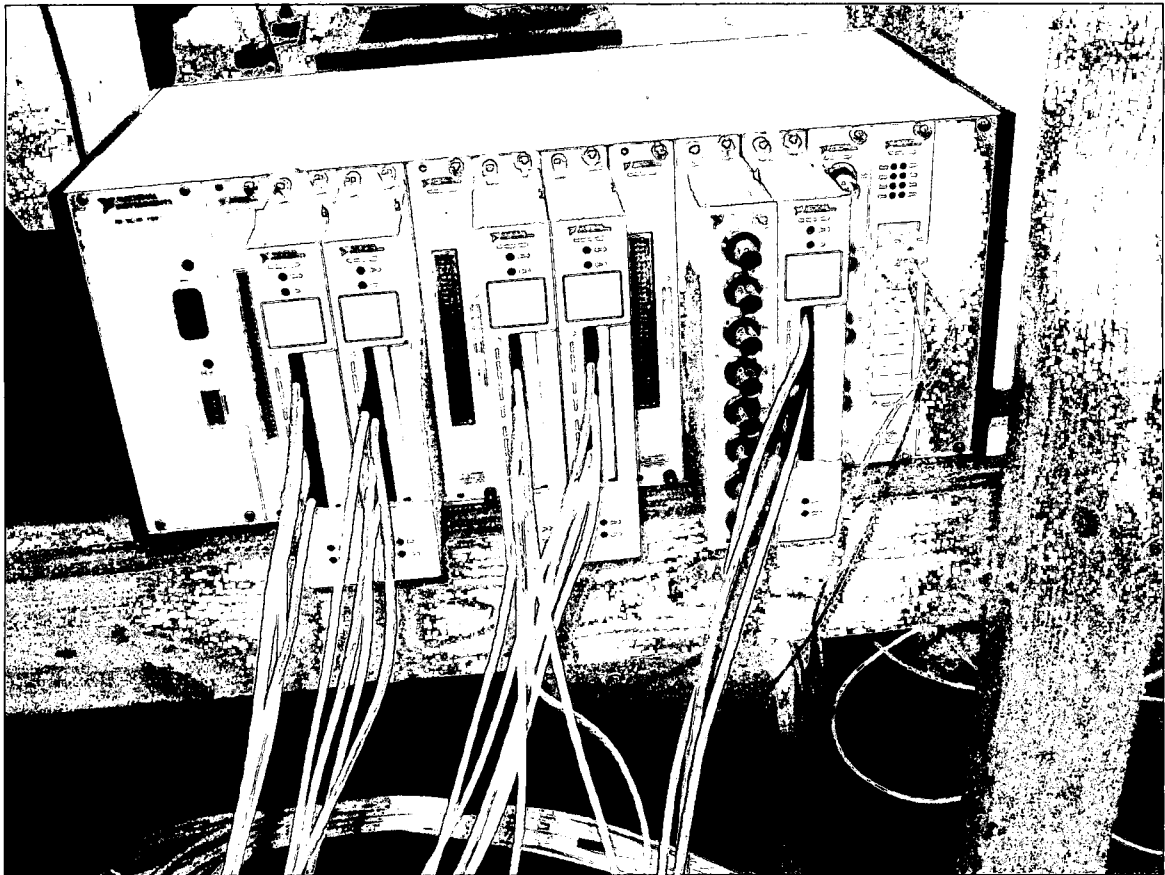


Figure 5-12 SCXI Chassis and SCXI Data Acquisition Cards.

The purpose of the SCXI 1121 boards was to perform analog input of each of the pressure transducers. Each board contains 4 isolated input channels with isolated excitation voltage. The boards' excitation voltage was set to 10 volts to match the required excitation of the Kulite pressure transducers. The calibration of the pressure transducers was approximately 20 mv/psid, resulting in a full scale reading from the transducer of approximately 0.100 volts. In the experiment fluctuations of less than 1 psid were expected, thus the maximum voltage expected from the Kulite was approximately 0.05 volts. Each of the input channels also has an independently configurable gain. On each of the Kulite channels a gain of 100 was used to gain the signal to a level of ~ 5 volts. Each channel also has an independently configurable low pass filter. The filters on all channels were set to 10,000 Hz. A SCXI 1320 4 Channel Terminal Block was used to connect the excitation and signal lines from each of the transducers to the front of the SCXI 1121.

A SCXI 1140 eight channel Simultaneous Sampling Analog Input board was connected to two, four channel SCXI 1121 boards with a ribbon cable. The full scale reading of the SCXI 1140 is 5 volts, with ± 30 volt over voltage protection. On the SCXI 1120 a channel gain of 100 was chosen. For pressure measurements of 1 psid, a gain of 100 on a SCXI 1121 channel results in a signal on the SCXI 1140 board of ~5 volts, or a full scale reading. Each channel on the SCXI 1140 board has a high input impedance amplifier followed by a track-and-hold amplifier. The track-and-hold amplifiers allows for simultaneous sampling of 8 channels with approximately 4 nanosecond skew between the first

and last channel. In the SCSI 1000 three sets of SCXI 1140/1121 bundles are installed. This allows for three sets of eight channels simultaneous analog input.

Simultaneous sampling of the analog inputs from the pressure transducers was accomplished in both hardware and software. The hardware was configured to sample 3 sets of eight channels of data simultaneously. To sample up to 24 of the channels simultaneously, National Instruments Measurements and Automation (MAX) Software and LabVIEW's DAQMX data acquisition driver were used. In MAX, a single task with as many as 24 channels was constructed. In the task the channels were configured for finite rate sampling. The configured task was then read with a single read call in the LabVIEW program. Having the channels configured in a task and called with a single read allows for as many as 24 channels to be read simultaneously.

Some "low speed", non-simultaneous data acquisitions were also required. The last SCXI 1121 on the SCXI 1000 chassis was used to measure the voltage output from the absolute and differential pressure transducers. Excitation of 10 volts DC was set on each channel to drive the transducers. The configurable low pass filter was also set to 10,000 Hz on each channel. The gains for each of the instruments were set as a function of their output. The full scale voltage of the Serta transducer is 5 volts. For a full scale signal to the SCXI 1140 board a gain of 1 was used. For the Sensotec absolute transducer, the full scale voltage is 0.030 volts, for atmospheric pressure the voltage is ~0.01. A gain of 200 is sufficient for the SCXI 1140 board to read up to 42 psia as full scale.

A SCXI 1112 was added to the SCXI 1000 chassis in slot 10. This is a Thermocouple Input Module. The board has 8 positions to sense signals from k-type thermocouples. Each thermocouple channel has a 2 Hz low pass filter. This filter ensures accurate temperature measurement while reducing line noise.

In the research the effect of flow on the wave propagation over a wide range of frequencies is desired. In general the FRF is the gain and phase response of the output of a system to an input of varying frequency. More specifically the FRF is defined as the inverse Fourier Transform of the impulse response of a system, Equation 5-16:

$$H(f) = \int_{-\infty}^{\infty} h(\tau) e^{-j2\pi f\tau} d\tau \quad (5-16)$$

The FRF is an excellent way to measure the effect of the flow on wave propagation. In this research, the input is the voltage applied to the speaker the outputs are the pressure signals from the various pressure transducers located along the experimental rig. The input signal was varied over a range of frequencies using a linear chirp (Equations 5-17 and 5-18). For a linear chirp the signal is a sinusoid. The frequency of the sinusoid that is swept from f_0 to f_{\max} over the period τ .

$$y(t) = \sin(2\pi(f_0 + kt)t) \quad (5-17)$$

$$k = \frac{f_{\max} - f_0}{\tau} \quad (5-18)$$

To accurately measure the FRF, the input and output signal must be measured simultaneously. Simultaneous analog input and output are achieved

by configuring both the hardware and software. As stated in rig the previous section, the analog input was configured in hardware and software so that up to 24 analog input channels could be read simultaneously. To output the Chirp signal and read the analog input signals simultaneously, a trigger signal must be used to synchronize the output and input. The trigger is sent over the built in Real-Time System Integration (RTSI) bus over a RTSI Cable. The RTSI bus is a signal bus that is reserved for signal timing between multiple boards. The RTSI cable connects the DAQ board directly to the analog output board over the RTSI bus. In software the analog input and output are specifically timed. The read of each pressure transducer (analog input) is timed such that it will not occur until the linear chirp (analog output) starts. The timing is accomplished through a trigger command. The read of the pressure transducer signals (analog input) is told to trigger not on its own start command, but on the start command of the linear chirp signal (analog output). This allows for the linear chirp to be output to the speaker and for the response of the pressure transducers to the chirp to be read simultaneously with less than 9 nanosecond skew between input and output.

The FRF of the chirp function input will have its own unique magnitude and phase response at every location along the experimental rig. The FRF will depend on both the location of the measured output and the boundary conditions of the experimental rig. Figure 5-13 depicts the FRF of a 1 meter open-open rig. Plotted is the FRF magnitude of all 15 pressure transducer outputs resulting from the chirp input voltage. Each line on the plot represents the FRF magnitude of a

different transducer at the locations outlined in Figure 5-4. The FRF magnitude of each transducer can be plotted against the location of the transducer at any frequency. If the FRF magnitude is plotted for a resonant frequency, the result is a measure of the mode shape of that resonant frequency. Figure 5-14 is an example of the mode shape derived from the FRF magnitude data. The FRF magnitude at the second resonant frequency was plotted versus the location of each of the 15 pressure transducers. The plot depicts the shape of the second longitudinal mode of the open-open rig.

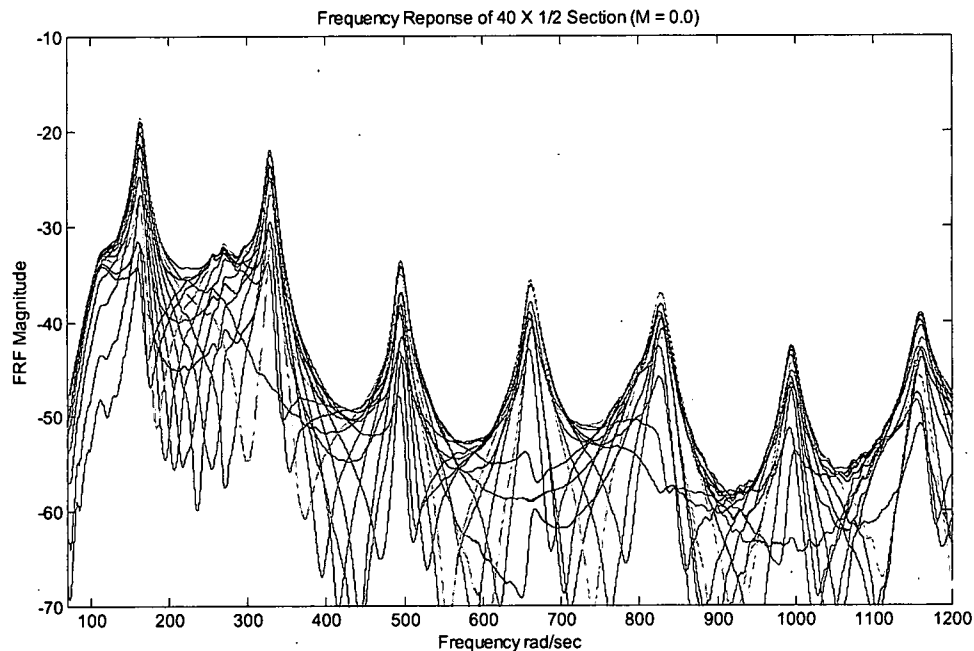
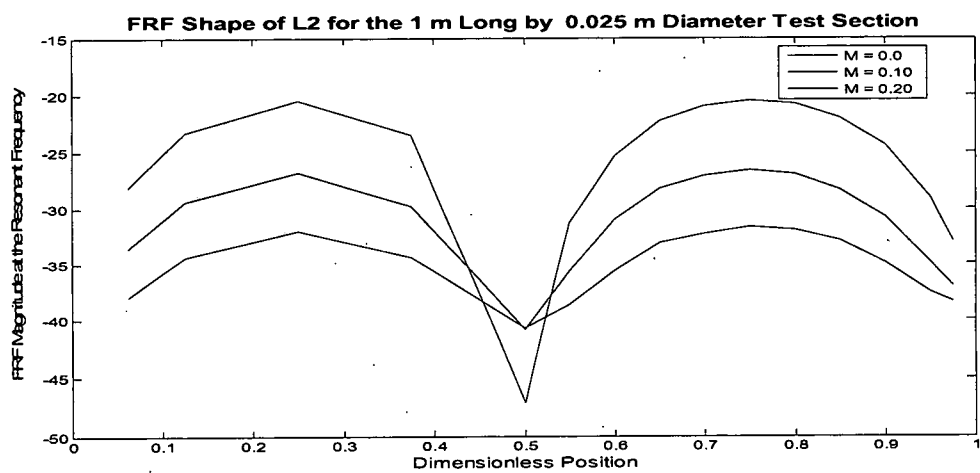


Figure 5-13 Example FRF Curve



**Figure 5-14 Example Mode Shape of the 2nd Longitudinal Mode Derived
from the FRF Magnitude Data**

VI. TURBULENCE AND SHEAR

For flows in cylindrical tubes, the velocity at the wall must be zero while the velocity away from the wall is finite. The gradient of velocity at the wall multiplied by the viscosity is defined as the shear stress in the fluid at the wall. Along the radius, the velocity is increasing to a maximum at the center of the cylinder. As a result of the velocity gradient from the wall to the center of the cylinder, vortices are formed with a range of sizes. These vortices help transition the velocity from the maximum at the center to zero velocity at the wall. The largest vortex is usually on the scale of diameter of the tube. The vortices convert flow kinetic energy into turbulent kinetic energy, making that energy unavailable to the mean flow. Vortices form with a very wide range of sizes, with varying turbulent kinetic energy. This size range of vortices is referred to as the turbulent spectrum or turbulent cascade.

Figure 6-1 illustrates the Turbulent Kinetic Energy (TKE) spectrum for a typical turbulent flow (Hinze 1987) and represents all of the varied scales of turbulence. Figure 6-1 can be obtained from the instantaneous velocity measured by a hot wire. The velocity measured by a hot wire, without acoustic excitation, can be divided into two components, the mean and fluctuating velocity (Equation 6-1). The instantaneous fluctuating TKE results from the square of the

$$U = \bar{u} + u' \quad (6-1)$$

instantaneous fluctuating velocity. Figure 6-1 is representative of the Power Spectral Density (PSD) of the time series of the instantaneous TKE.

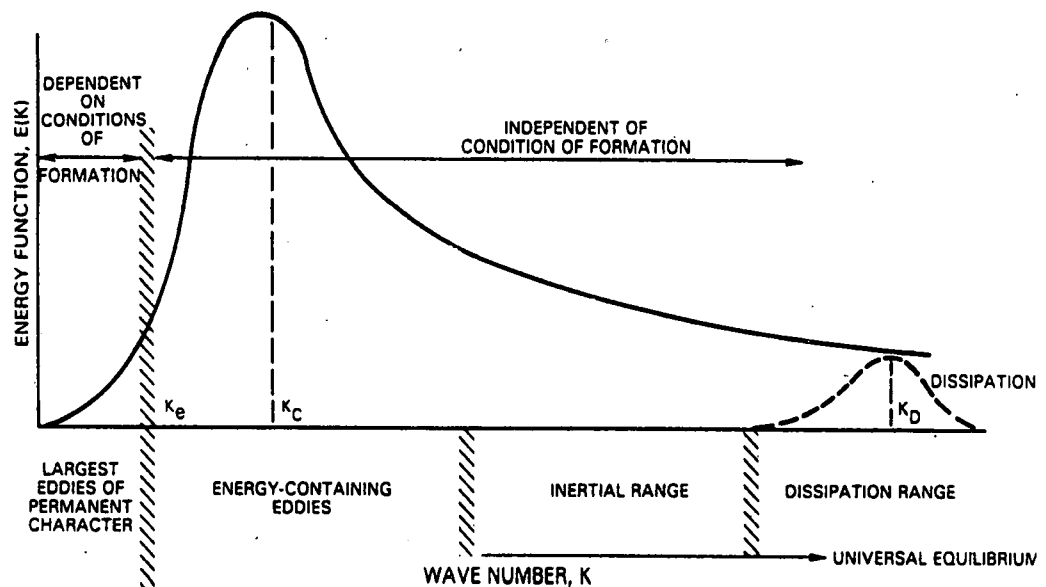


Figure 6-1 Turbulent Energy Spectra (Hinze, 1987)

Examining Figure 6-1, some observations can be made about turbulence. First, there are four ranges of turbulent flow, the large eddy range, the energy containing eddies range, the inertial range and the dissipation range. Vortices can grow or shrink as they interact with the gradients of velocity in the flow. As a result, the TKE can transition up or down the cascade. For flow in cylindrical tubes, the energy cascades to smaller and smaller vortices of higher and higher frequencies. For flows on the scale of the earth, the TKE from smaller vortices can cascade up the spectrum to larger and larger scales. This process is the reason for the formation of hurricanes.

According to Kolmogorov (1941) vortices cascade to smaller and smaller scales and physically become smaller and smaller. At some point in the spectrum, the scale of the vortex is so small that molecular diffusion becomes important. At this scale, the TKE contained in the smallest vortex is non-isentropically converted to heat energy through viscous dissipation. This scale is known as the Kolmogorov length scale and can be calculated for any flow. Viscous dissipation of energy occurs in the boundary layer at the wall due to no-slip where the scale of vortices is small. Away from the wall, the cascade dictates that there are vortices on the order of the Kolmogorov scale that exist in every flow. For flows with non-zero viscosity, these vortices also dissipate energy as heat to the flow.

According to Encyclopedia Britannica, damping is defined as the resistance to vibratory motion (oscillatory, noise, alternating current, etc.) by dissipating energy. Turbulence dissipates flow energy in two ways. The most obvious form of dissipation is the non-isentropic conversion of TKE to heat at the smallest scales of the flow. The other form of dissipation is more abstract. By its nature, turbulence converts kinetic energy from the mean flow to turbulent kinetic energy, making the energy unavailable to the mean flow. The turbulent cascade can also interact with the acoustic field (Howe 2003). Turbulence can be an excitation and source of energy to the acoustics. This is illustrated by the whistling that occurs when one blows over the opening of a bottle, or by the audible noise created by air jets. Turbulence can also be a sink to acoustic

energy in the same fashion that it is a sink of kinetic energy in the mean flow, converting acoustic energy to turbulence.

VII. RESULTS AND DISCUSSION

In Chapter 2, equations for the propagation of waves in 2 dimensions with flow were derived. Examining these equations, there are three main effects from the flow on the wave propagation in ducts: convection, shear, and viscosity. The equations for wave propagation were further refined assuming isentropic flow. This assumption had two results. First, pressure and density were related algebraically. Second, since viscous dissipation is a source of entropy, viscous dissipation is ignored. Equation 2-18 was the final governing equation for wave propagation with convection and shear. These remaining two effects, shear and convection will be examined in detail in this chapter. This chapter is divided into two sections to systematically examine the relationships between flow, damping, and wave propagation.

The first section of this chapter will examine the FRF and Turbulent Kinetic Energy data. Both data will be used to better understand the effects of flow on wave propagation. The FRF data will be used to construct mode shapes for several flow conditions. The FRF data measured at the center pressure transducer will be used to derive the amount of damping in each of the modes at that location for several flow conditions. Both data will be used to establish a link between flow and damping. This link is further explored by comparing the damping data and turbulent spectrum data collected with a hot wire. A clear correlation between increased TKE and increased damping is evident in the data.

The second section in this chapter will explore the time domain results from models and experiments. Traditionally in acoustics the right and left moving waves combine to form a standing wave. A one-dimensional standing wave manifests itself as a single spatial sinusoid whose amplitude changes as a function of time. The analytical solutions and time domain data from the models and experiments will illustrate that convection imparts motion onto the standing wave. This motion will be demonstrated in both longitudinal and circumferential waves.

Frequency Response Function (FRF) Data

FRF data were obtained from a variety of sources, both numerical and experimental. First computational models of the longitudinal and circumferential experimental rig, detailed in Chapter 5, were constructed and meshed using COMSOL. The weak form mode of COMSOL was used to model Equations 4-1, 4-2 and 4-3. The effect of convection and shear on wave propagation was isolated by varying the Mach number over the entire experimental rig. The FRF was obtained using the Frequency Response Analysis tool in the Acoustics Module of COMSOL.

The longitudinal experimental rig was modeled using FEA with COMSOL. The wave equation with shear and convection was modified with numerical constants so the effects of convection and shear could be studied separately. Equations 7-1 and 7-2 were implemented in COMSOL and the Frequency Response Function was obtained using the weak form solver.

$$\begin{aligned} \frac{\partial^2 p'}{\partial t^2} + 2 * SCALE1 * M(y) * a \frac{\partial^2 p'}{\partial x \partial t} - a^2 * [1 - (SCALE1 * M(y)^2)] \frac{\partial^2 p'}{\partial x^2} \\ - a^2 * \frac{\partial^2 p'}{\partial y^2} - 2 * SCALE2 * \bar{\rho} * a^3 * \frac{\partial v'}{\partial x} * \frac{\partial M(y)}{\partial y} = 0 \end{aligned} \quad (7-1)$$

$$\bar{\rho} * \frac{\partial v'}{\partial t} + SCALE1 * \bar{\rho} * M(y) * a \frac{\partial v'}{\partial x} = - \frac{\partial p'}{\partial y} \quad (7-2)$$

The scale factors allow for the study of the effect of shear and convection individually and combined. The response is that of the voltage applied to the speaker model as the input to the system and pressure at center computational point of the longitudinal experimental rig as the output of the system. Shear was modeled assuming the Mach number had a parabolic profile in the y direction with zero Mach number at the walls.

Figure 7-1 depicts the FRF magnitude of the FEA model. The blue dashed is the FRF Magnitude of the rig with no flow, $SCALE1 = SCALE2 = M(y) = 0.0$. The solid red line is the FRF magnitude for shear only, $SCALE1 = 0.0$. The green line with large dashes is for the convection case only, $SCALE2 = 0.0$. Finally the thin black line represents the case for both shear and convection, thus both scale factors are equal to one. For the convection only case the response of the system appears damped and the resonant frequency differs from the resonant frequency without flow by:

$$\omega_{convective} = \omega_{M=0} (1 - M^2) \quad (7-3)$$

In the case of shear only the resonant frequency does not change, but magnitude decreases. Combined, shear and convection, the resonant frequency is between

the two extremes of convection only and no flow. Combined, the magnitude is less than that of both cases individually.

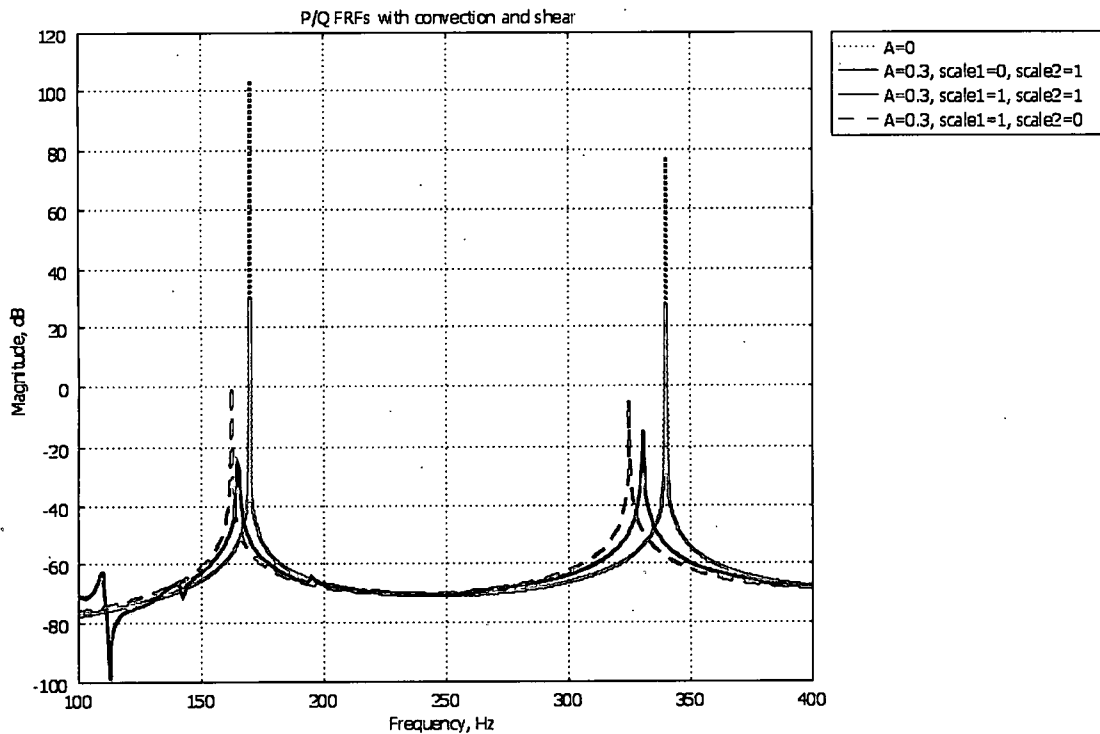


Figure 7-1 Frequency Response Function Magnitude Plot of the First and Second Modes of the Longitudinal Rig Modeled Using COMSOL

Equation 7-4 is the transfer function for a simple second order damped system. ω_n is the natural frequency of the system. G is a gain. ζ is the damping ratio of the system.

$$\frac{G\omega_n^2}{s^2 + 2\zeta\omega_n s + \omega_n^2} \quad (7-4)$$

Figure 7-2 is a plot of a Frequency Response Function magnitude of equation 7-4 for several damping ratios. Note that increases in damping ratio decrease the magnitude of the FRF. For small amounts of damping ratio, < 0.10 the resonant frequency changes very little. This same effect is seen in Figure 7-1. For the shear only case the magnitude changes, but frequency does not. Thus the FRF of shear has the same trend as the FRF of a simple second order system with damping. Shear acts like a damped system with only small amounts of damping.

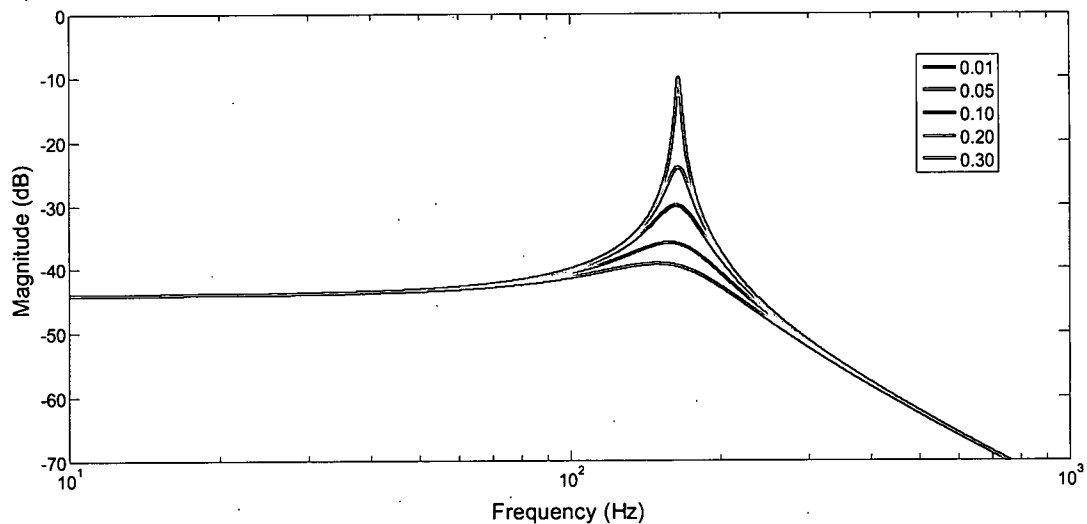


Figure 7-2 FRF of a Second Order Damped System

Figure 7-3 depicts the FRF magnitude of the longitudinal experimental rig modeled with COMSOL. The response is that of the pressure at center of the rig with convection only. This was achieved by assuming constant Mach number over the spatial domain and setting SCALE2 = 0.0. The Mach number was varied from 0.0 to 0.4. For acoustic modes, the center location of the rig is an anti-node for the first, third, fifth, and seventh modes and the response will be at a maximum at this location for these modes. The center location for the second,

fourth, and sixth modes is a node and the response will be a minimum at this location for these modes. The blue center line curve in Figure 7-3 is the response for no flow. The green solid line is for Mach number = 0.20. The red solid line is for Mach number = 0.40. Note the peaks represent the first 5 odd

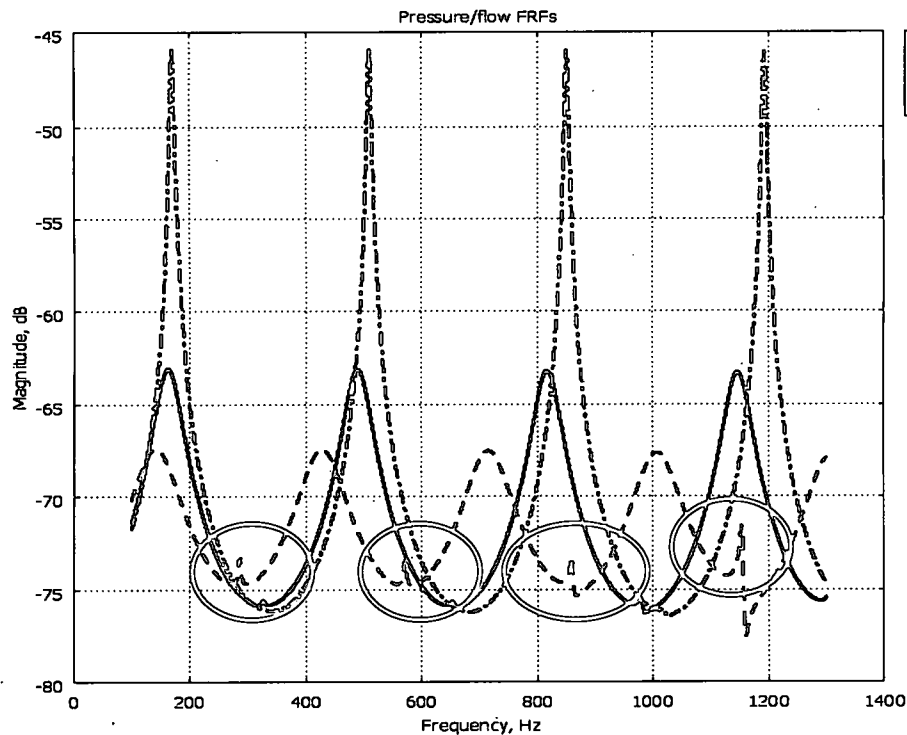


Figure 7-1 FEA FRF at the Center Pressure Node for Increasing Mach Number

modes of the system. As the Mach number is increased something interesting happens to the response of the even modes. For Mach number of 0.20 the magnitude of the FRF increases at the frequency of the even modes, but decreases for the odd modes. As Mach number is increased further to 0.40 the magnitude of the even modes again increases while the magnitude of the even modes decreases further. For a simple second order damped system, Figure 7-

2, damping uniformly decreases the FRF magnitude around resonance. This increase in FRF magnitude at the even modes is not typical of simple damped systems.

Experiments were conducted on the longitudinal and circumferential experimental rigs over a range of flow conditions to obtain Frequency Response function data to compare to the modeling data. Figures 7-4 through 7-8 are plots of the magnitude of the FRF for the 1 m long by 0.0508 meter (2 inch) diameter longitudinal experimental rig over a range of Mach numbers. The FRF magnitude for the 0.0254 meter (1 inch) and 0.0016 meter (1/2 inch) experimental rigs had similar trends to Figures 7-4 through 7-8, but is not provided. Figures 7-9 through 7-12 are plots of the magnitude of the FRF for the circumferential rig over a range of blower mass flow rates. For both the longitudinal and circumferential rigs the FRF for all of pressure transducer locations is plotted on all of the plots.

Studying Figures 7-4 through 7-7 several observations are noted. For the longitudinal rig, the seven peaks in Figure 7-4 are typical of the first seven modes of the longitudinal rig. In all cases as the flow velocity increases, the FRF magnitude of the modes of the rigs decreases at the resonant frequency of the modes. Also, as the flow increases the value of the magnitude at the resonant frequencies decreases. This was observed by Ingard and Singhal (1975). This follows the trend from the finite element model in Figure 7-1. Like the finite

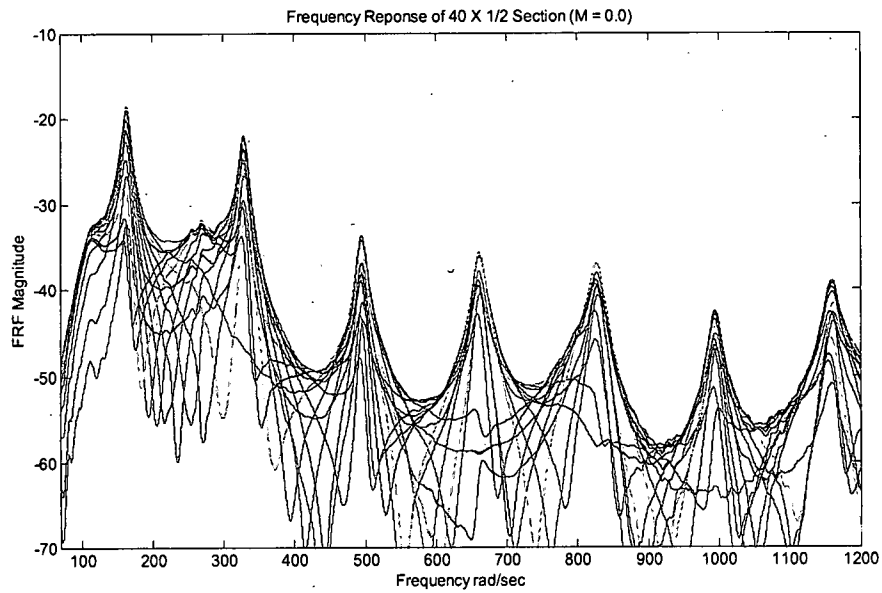


**Figure 7-4 FRF Magnitude of the 1m by 0.0158m (1/2 inch) Diameter
Longitudinal Rig, Mach Number = 0.0**

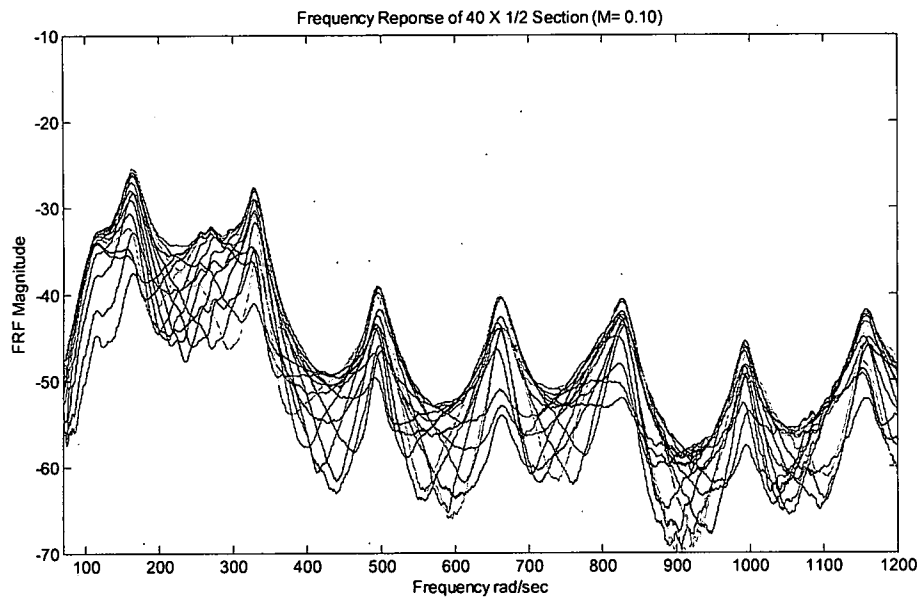


**Figure 7-5 FRF Magnitude of the 1m by 0.0158m (1/2 inch) Diameter
Longitudinal Rig, Mach Number = 0.10**

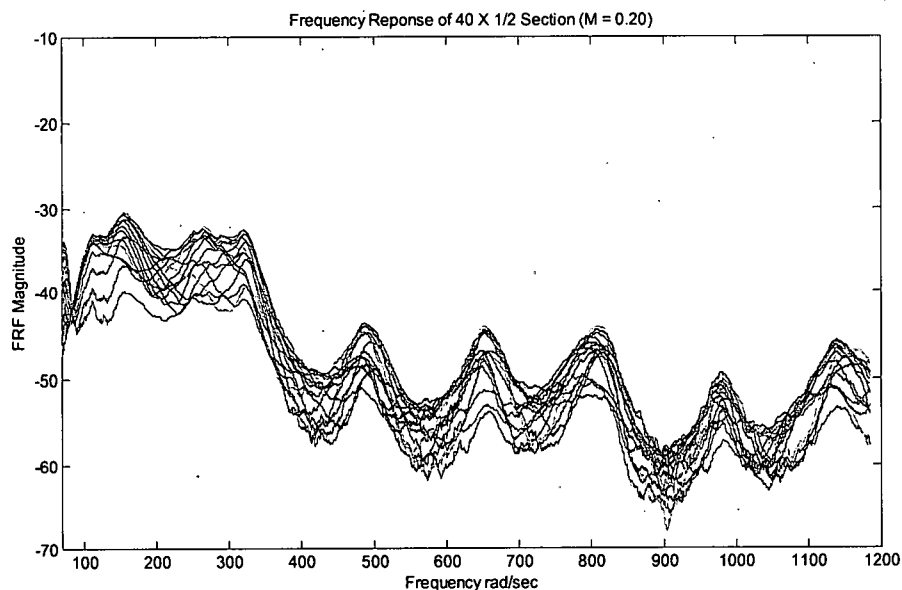


**FIGURE 7-6 FRF MAGNITUDE OF THE 1M BY 0.0158M (1/2 INCH) DIAMETER
LONGITUDINAL RIG, MACH NUMBER = 0.20**

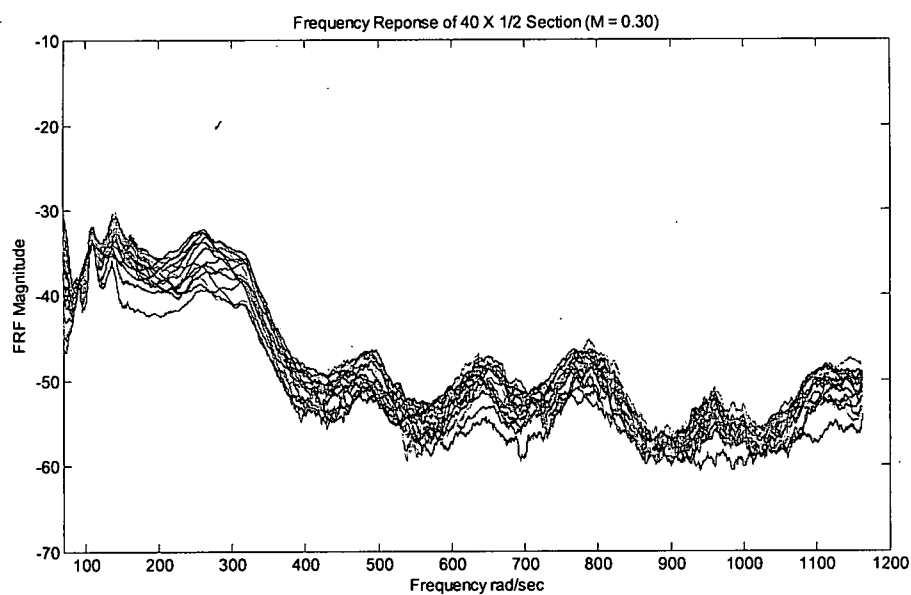


**Figure 7-7 FRF Magnitude of the 1m by 0.0158m (1/2 inch) Diameter
Longitudinal Rig, Mach Number = 0.30**

element model, the FRF magnitude and resonant frequencies decrease. The frequency and magnitude of the peaks decreases in a similar way as the response of a simple system with increased damping (Figure 7-2).

The FRF data presented thus far is for all of the transducers plotted on a single plot. Figure 7-8 depicts the FRF for the center transducer only, of the 1 meter long by 0.0254 meter (2 inch) diameter experimental rig. In Figure 7-8 the first, third, fifth, and seventh longitudinal modes are clearly seen by peaks distributed across the plot. The second and fourth longitudinal modes have greatly reduced magnitudes but are also visible. In Figure 7-8 it is clear that increasing the Mach number of the flow decreases the magnitude and the frequency of the odd modes. The decrease is attributed to the combined convective and viscous damping associated with the increasing flow.

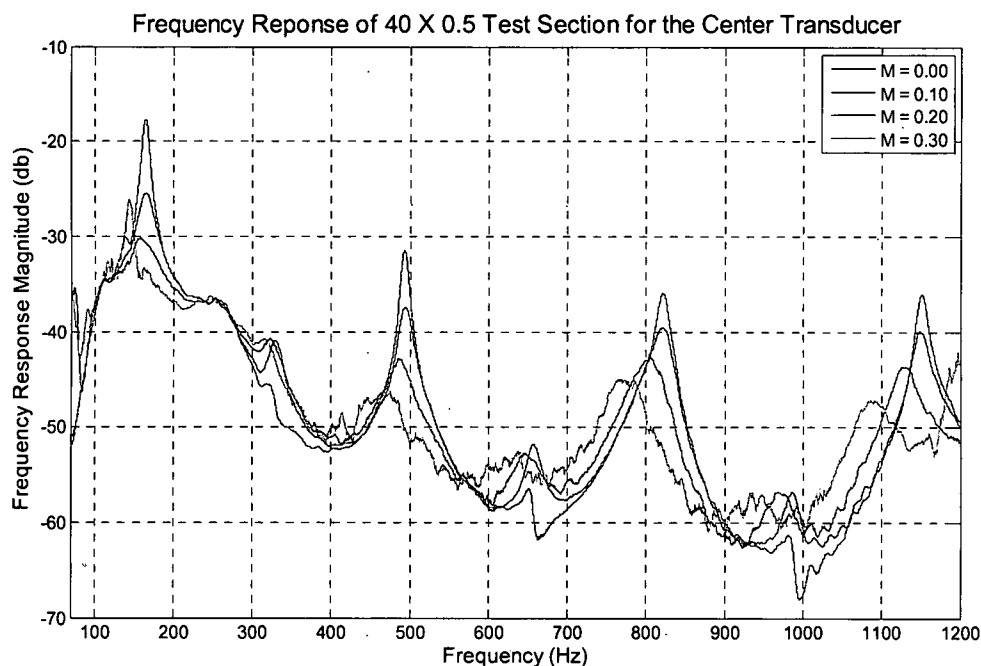


Figure 7-8 FRF Magnitude for the Center Transducer of the 0.0504 Meter (2 Inch) Diameter Longitudinal Rig for a Range of Mach Numbers

In Figure 7-8 the response of the second, fourth and sixth modes is also visible. As in an earlier portion of this section, the center transducer corresponds to the location of the node for the second, fourth, and sixth modes when there is no flow. It is also clear from Figure 7-8 that as the Mach number increases from 0.0 the magnitude of the FRF of the second, fourth and sixth modes increases by 5 dB at the center transducer. This is in direct agreement with the finite difference model results depicted in Figure 7-3.

Observations can also be made studying the FRF magnitude data from the circumferential rig. Figure 7-9 is the FRF magnitude for frequencies from 70-2800 Hz. Depicted in Figure 7-9, for frequencies up to 1250 Hz the magnitude of the FRF is nearly constant. All of the pressure transducers are mounted circumferentially at the same axial location. Since the transducers are at the same axial location and the magnitude does not change, the peaks between 70 and 1250 Hz must be associated with the drive, an axial mode, or radial mode.

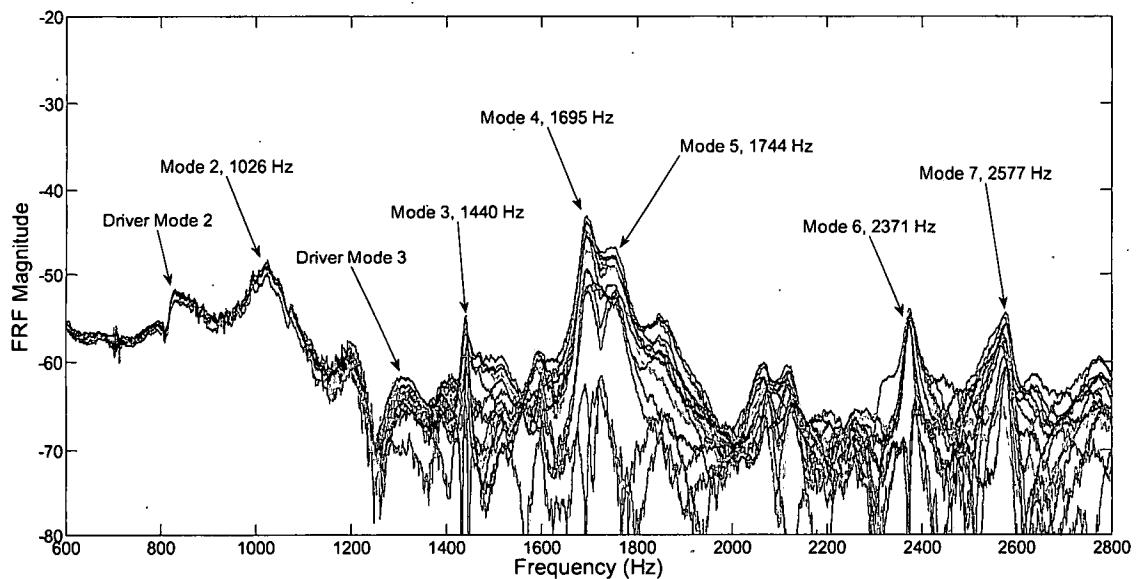


Figure 7-9 FRF Magnitude of the Circumferential Rig With no Flow

Figures 7-10 to 7-13 depict the FRF magnitude of the circumferential rig from 1250 Hz to 200 Hz for increasing blower mass flow. Figure 7-10 depicts the FRF magnitude for no flow. Three peaks are easily seen in the figure at 1440, 1700, and 1760 Hz. As the mass flow increases the peak at 1440 is quickly indiscernible with the noise. As the blower flow increases the peak near 1700 Hz decreases in magnitude and frequency. The peak at 1700 is most likely the first circumferential mode. As the flow rate increases the peak at 1740, though, maintains a constant magnitude and frequency. This is most likely a longitudinal or radial mode. In the mode shapes will be obtained from the FRF magnitude data and conclusive identity of the modes will be obtained.

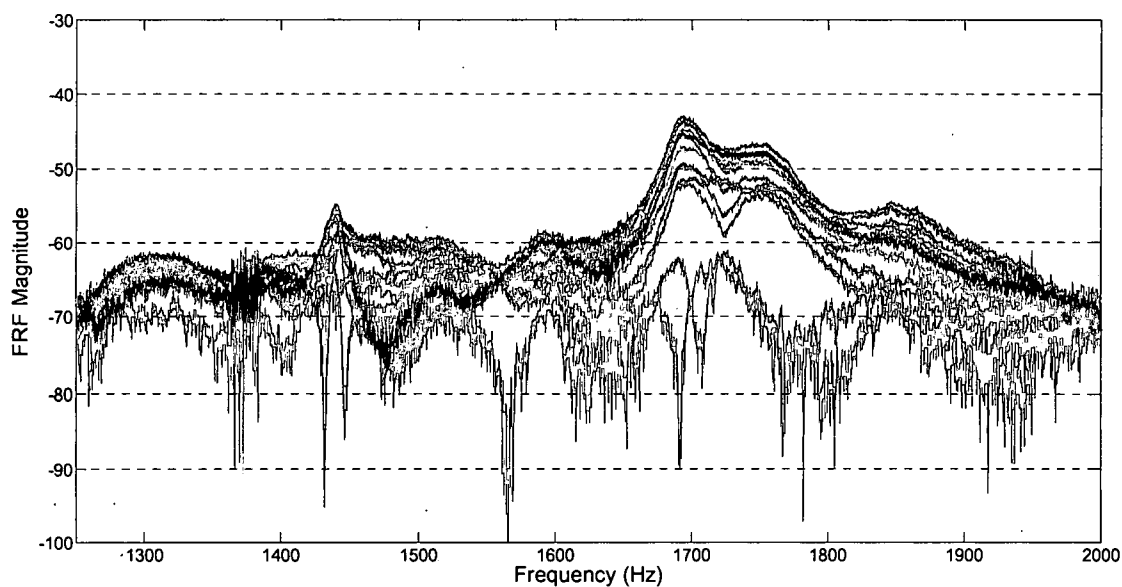


FIGURE 7-10 FRF MAGNITUDE OF THE CIRCUMFERENTIAL RIG, WITH NO FLOW

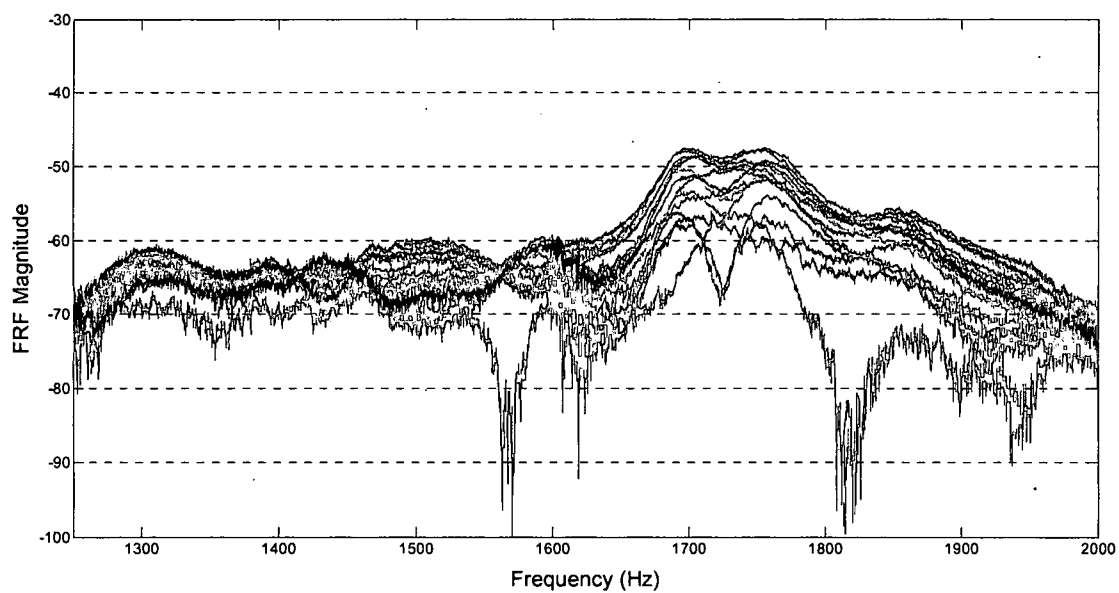


Figure 7-11 FRF Magnitude of the Circumferential Rig, Flow = 0.05 kg/s

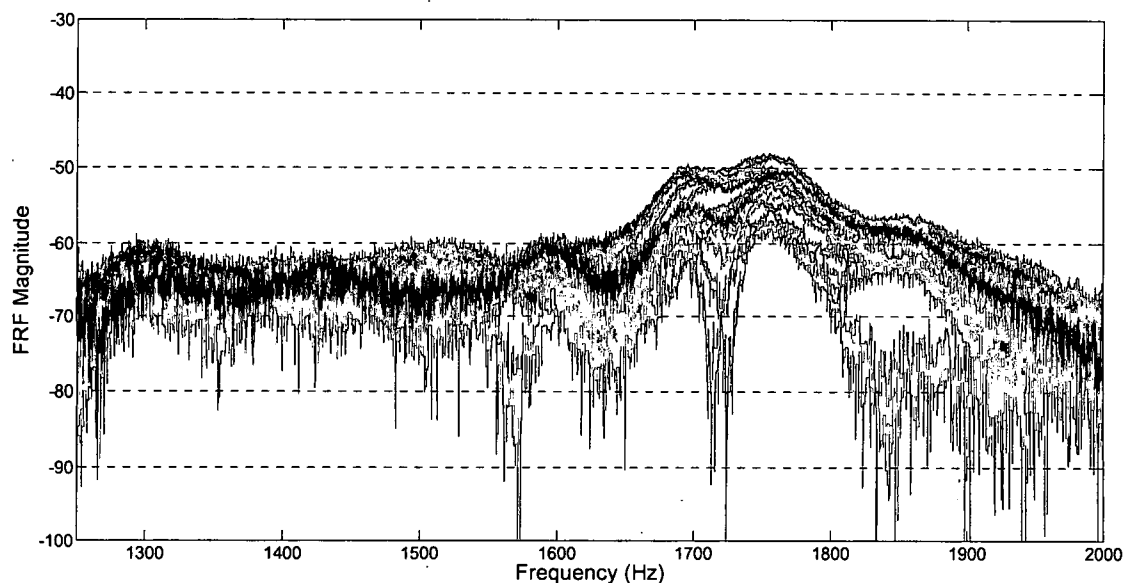


Figure 7-12 FRF Magnitude of the Circumferential Rig, Flow = 0.09 kg/s

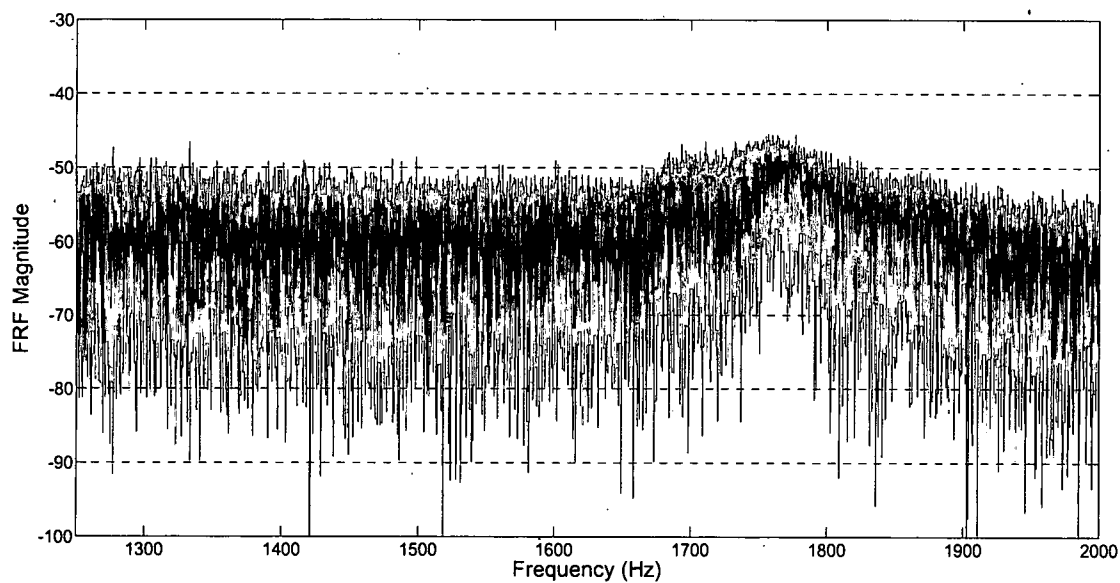


Figure 7-13 FRF Magnitude of the Circumferential Rig, Flow = 0.13 kg/s

Another observation is seen when comparing the FRF magnitude in the 200 to 400 Hz range for all Mach numbers for the longitudinal rig. Comparing

Figures 7-4 through 7-8, small peak are seen at approximately 275 Hz at a magnitude of -35 db. For this peak, as the flow is increased the magnitude does not change nor does the frequency. This is unlike the resonant peaks associated with the modes of the experimental rig. Because the peak is unaffected by the changing flow conditions, the modes must occur in a portion of the rig that is not affected by the Mach Number variation. The cross sectional area of the speaker driver is approximately 100 inches squared. The cross sectional areas of the experimental rigs are approximately 0.30, 0.78, 3.14, 23 square inches. The maximum Mach number in the speaker driver was always less than 0.05, thus the magnitude and resonant frequencies of the blower are unaffected by increasing the flow in the experimental rigs.

A finite element analysis of the speaker driver alone was performed. Since the flow in the speaker driver is negligible, the wave equation in the Acoustics Mode of COMSOL was used. The speaker driver is a closed-open acoustic system. Figure 7-14 depicts the predicted first mode shape of the speaker driver. The predicted frequency is approximately 277 Hz. This is the same as the peak noted in Figures 7-4 through 7-7 that does not change with increasing Mach number. Figure 7-15 depicts the second mode shape of the speaker driver predicted using FEA. The frequency predicted by FEA is approximately 830 Hz. This corresponds with the peak marked Driver Mode 2 in Figure 7-9. From this analysis the frequency of the 3rd mode of the driver is approximately 1380. This corresponds to the peak marked Driver Mode 3 in Figure 7-9.

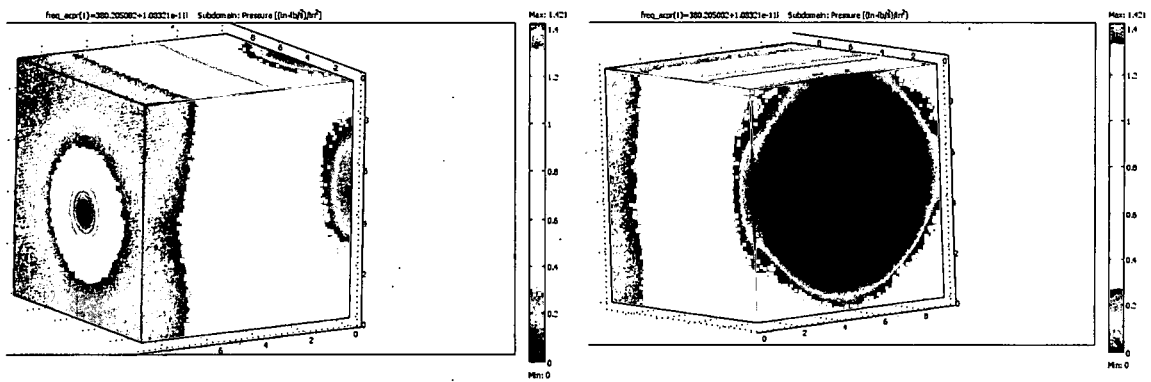


Figure 7-14 FEA Mode Shape of the First Mod of the Speaker Driver

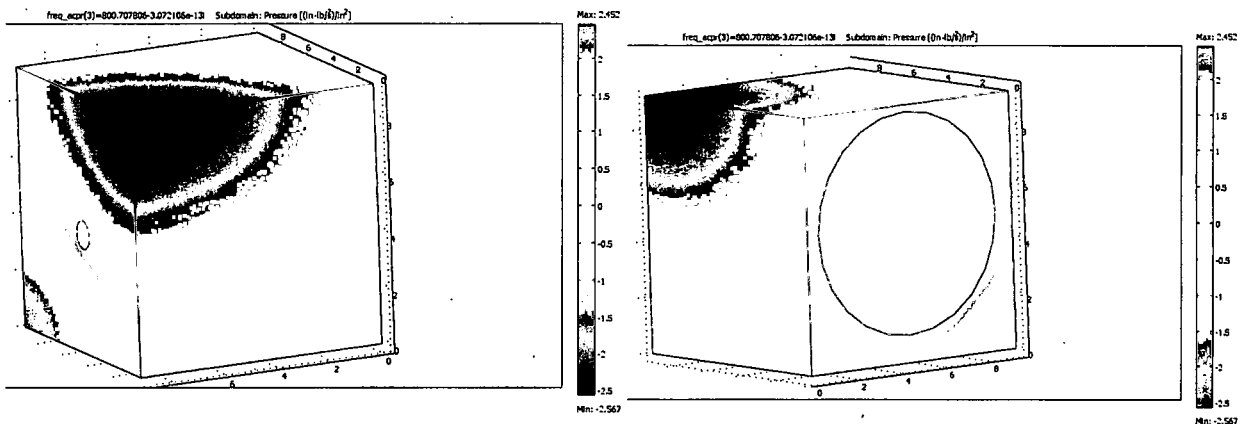


Figure 7-15 FEA Mode Shape of the Second Mode of the Speaker Driver

Mode Shapes

The mode shapes were determined from the measured FRF data obtained at various locations along the experimental rig (Refer to Chapter 5 for the location of the pressure transducers for each of the four experimental rigs). The shapes were constructed as outlined in Chapter 5, section 5.3.2. Figures 7-16

through 7-20 depict the first five modes for the 1 meter long, 0.0508 meter (2 inch) diameter longitudinal rig. Examining the mode shape data for the longitudinal rigs, several general comments can be made. First, in all cases the mode shapes are symmetric about the center of the experimental rig. The second observation noted from the data is, as Mach number is increased, the magnitude of the mode shape generally decreases. This occurs while the shape of the mode is maintained. This trend is true everywhere except for the center location for the second, and fourth mode. At the center location for the second mode, the magnitude increases. The magnitude also increases for the fourth mode at the center location. This is in agreement with the modeling data in Figure 7-3 where the amplitude of the even modes increases at the center as Mach number is increased above zero. The final trend noted in the figures is the location of the maximum. In all cases, the location of the maximum can easily be found on the figure. Later the maximum location will be used to estimate the damping ratio from the FRF data. This maximum will also be used when selecting the frequency for the time domain experiments in the next section.

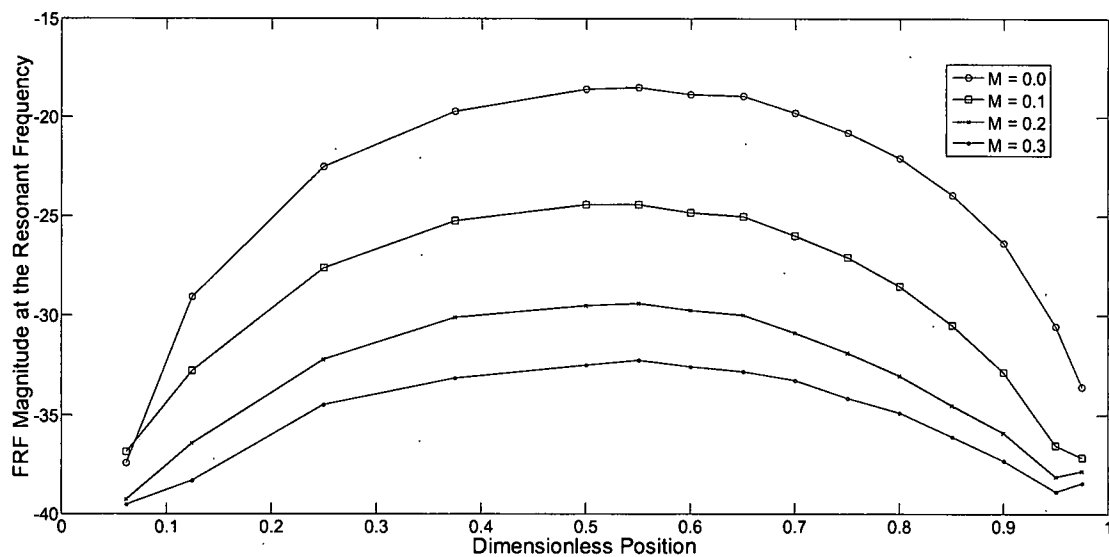


Figure 7-16 Mode Shape for the Longitudinal Rig, First Mode

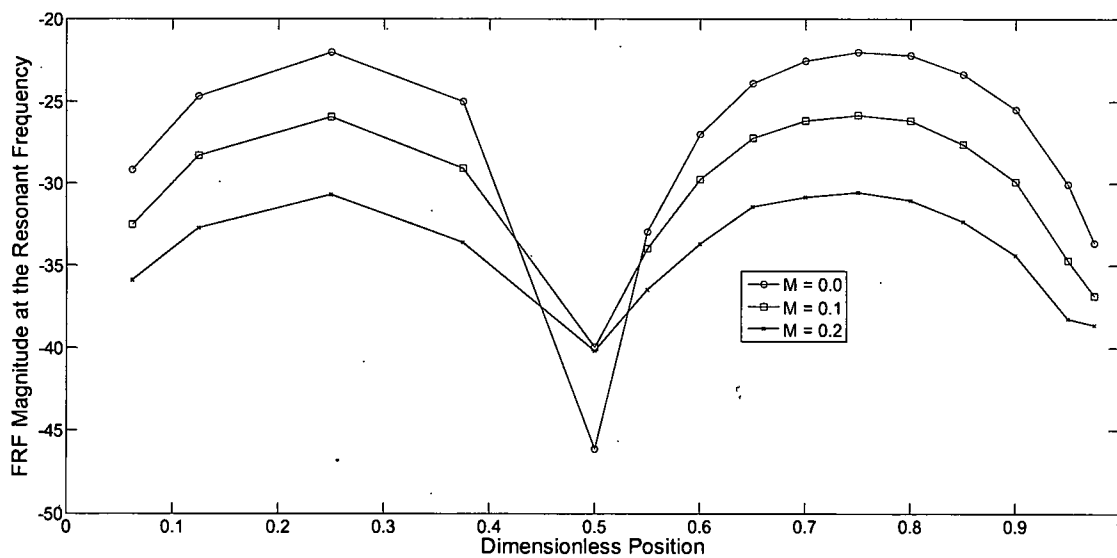


Figure 7-17 Mode Shape for the Longitudinal Rig, Second Mode

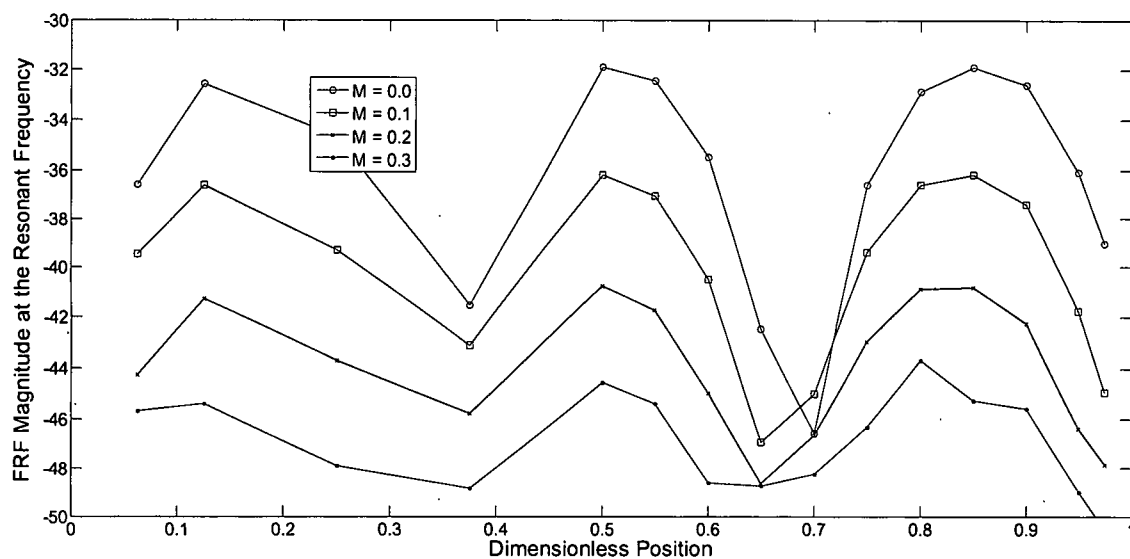


Figure 7-18 Mode Shape for the Longitudinal Rig, Third Mode

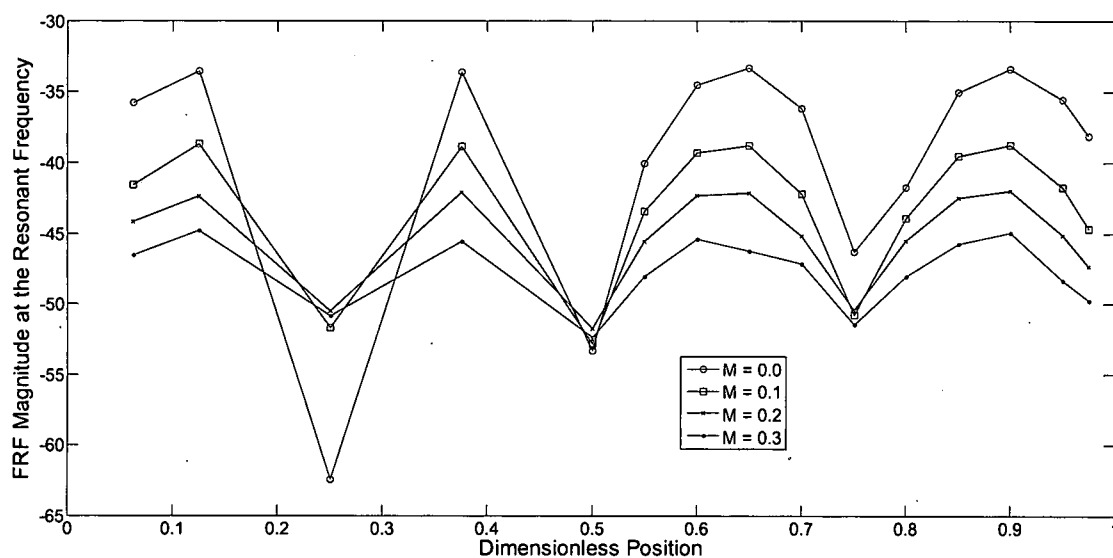


Figure 7-19 Mode Shape for the Longitudinal Rig, Fourth Mode

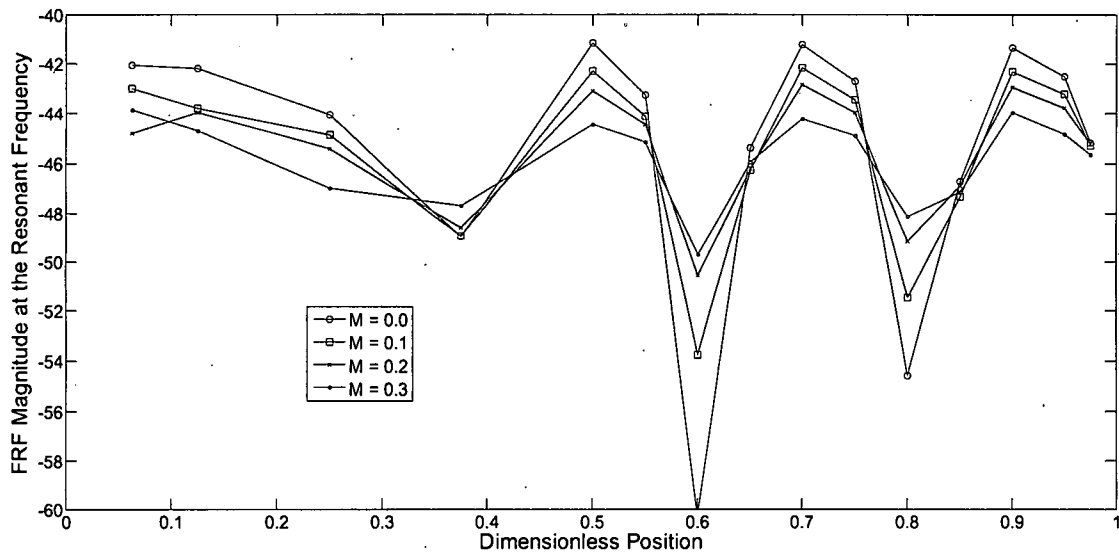


Figure 7-20 Mode Shape for the Longitudinal Rig, Fifth Mode

Mode shapes for the circumferential rig were obtained FRF magnitude data in Figure 7-9. Figure 7-21 depicts the second through seventh mode shapes for the circumferential rig with no flow. The x axis of Figure 7-21 is the circumferential position of the pressure transducer in degrees. Note, the shape of the 4th and 6th modes change with circumferential position. The rest of the modes do not change with circumferential location. Because the shape of the 4th and 6th modes changes with circumferential position, it can be concluded that the 4th and 6th modes have a circumferential component. The remaining nodes do not change with circumferential position, thus they are either longitudinal or radial modes of the circumferential rig, or they are modes of the speaker driver.

Figure 7-22 depicts the mode shape data for the circumferential rig for three flow conditions, no flow, 0.054, and 0.090 kg/s. These results are similar to those of the longitudinal rig. As swirling flow increases the shape remains the

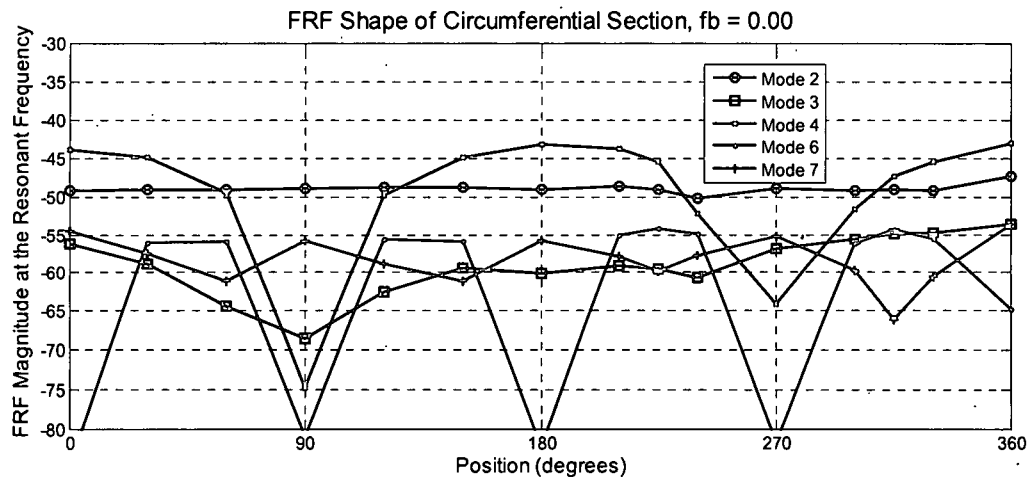


Figure 7-21 Mode Shape for the Second Through Seventh Modes of the Circumferential Rig Without Flow

same and the magnitude decreases except at the node locations. At the node locations, as the swirling flow increases the magnitude increases. This increase was also exhibited in the even modes for the longitudinal rig.

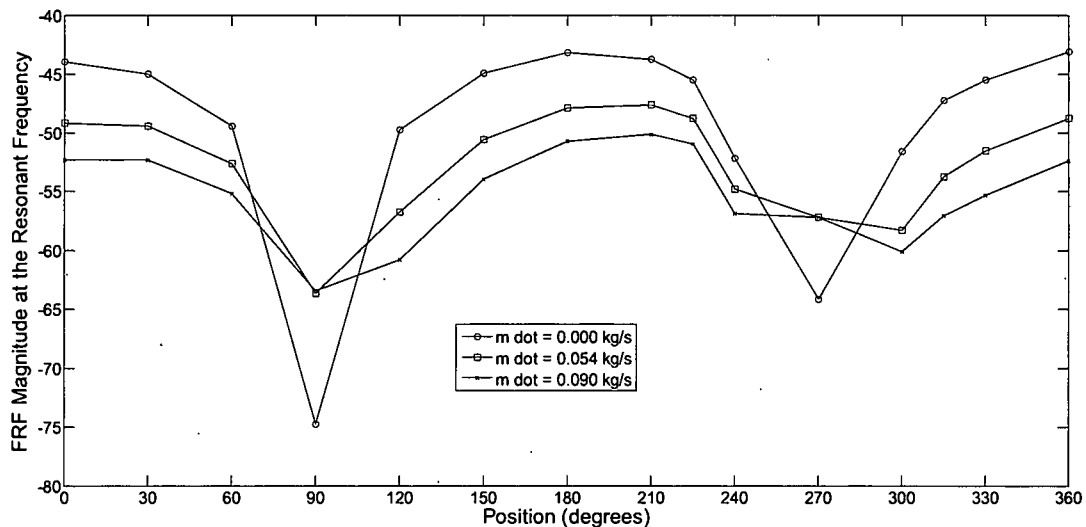


Figure 7-22 Mode Shape for the Circumferential Rig, Third Mode

Damping From FRF Data

In the extreme, each of the peaks can be analyzed to estimate the overall damping from the flow. The frequency associated with center of the peak is the resonant frequency. From the shape of the peak the amount of damping at that frequency can be estimated. To estimate the damping, each mode is represented as a second order damped system, equation 7-4. The natural frequency is not a value that can be obtained directly from the FRF figure and must be estimated. Equation 7-5 relates the resonant frequency, damping ratio and natural frequency.

$$\omega_n = \frac{\omega_d}{(1 - \zeta^2)^{1/2}} \quad (7-5)$$

To obtain the damping for each peak, the gain and the damping coefficient can be iterated until the second order system approximately fits the experimental data. Figure 7-23 is an example of such a curve fit. The red dashed curve is the experimental FRF data for the 1 meter long by 0.0508 meter diameter experimental rig. The blue solid curve is the plot of the second order system from Equation 7-4. An acceptable fit was obtained by iterating the resonant frequency, gain and damping ratio. Upon obtaining such a fit, the resonant frequency and the damping ratio were recorded in a spread sheet.

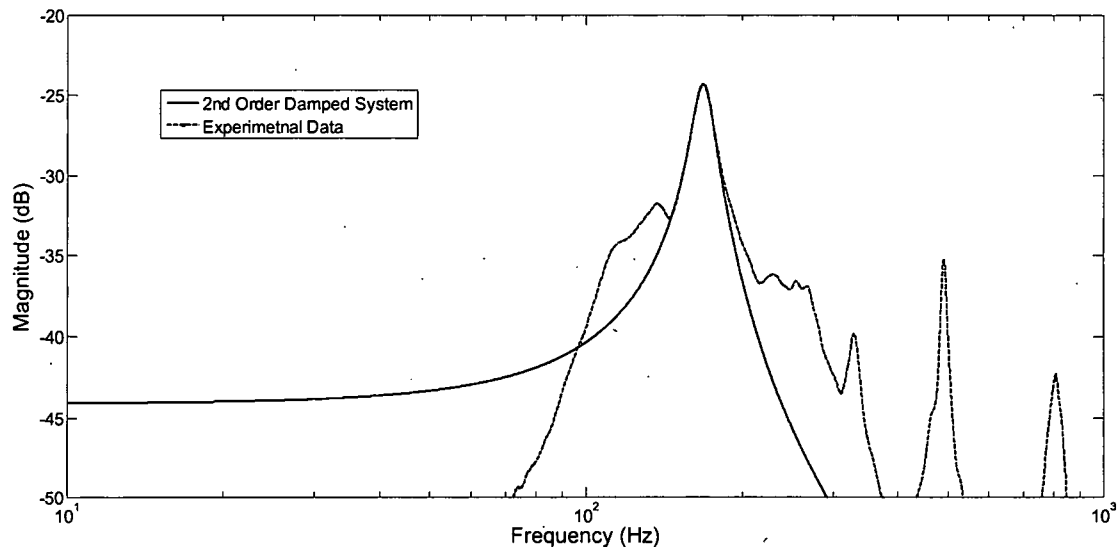


Figure 7-23 Example Curve Fit for 1 m Long by 0.0508 m Diameter
Experimental Rig, Mach Number = 0.10

Tables 7-1, 7-2, and 7-3 are tables of the resonant frequency and damping coefficient obtained from the curve fitting. The tables were constructed for the 1 meter long by 0.0508, 0.0254, and 0.0158 meter diameter experimental rigs respectively. Comparing the data from each of the rigs, several trends are apparent. First, the damping generally increases as the diameter of the experimental rig decreases for all modes and Mach numbers. Figure 7-24 is a plot of the total rig pressure drop for each experimental rig. For a given Mach number, the pressure drop of the rig increases as the diameter of the experimental rig decreases. The pressure drop is an indirect measure of the damping. The trend of increasing pressure drop correlates well with the increase in damping coefficient as the diameter of the rig decreases.

M	L1	ζ	L2	Z	L3	ζ	L4	ζ	L5	ζ
0.00	167.45	0.0256	327.55	0.0185	490.52	0.0089	649.35	0.0076	808.00	0.0050
0.10	168.60	0.0525	328.22	0.0260	490.12	0.0133	648.35	0.0119	808.20	0.0140
0.20	165.32	0.0975	323.32	0.0395	482.35	0.0245	637.35	0.0217	790.15	0.0205
0.30	160.70				466.80	0.0445	613.15	0.0397	765.15	0.0225

Table 7-1 Damping of 1.0 m Long, 0.0508m Diameter Experimental Rig

M	L1	Z	L2	ζ	L3	ζ	L4	ζ	L5	ζ
0.0	164.55	0.0254	328.11	0.0141	492.92	0.0094	655.88	0.0081	821.25	0.0095
0.1	165.90	0.0689	328.80	0.0269	494.47	0.0187	657.42	0.0151	821.25	0.0155
0.2	162.05	0.1090	322.76	0.0405	486.62	0.0339	648.42	0.0311	802.60	0.0242
0.3					477.00	0.0542	624.25	0.0521	772.60	0.0283

Table 7-2 Damping of 1.0 m Long, 0.0254 m Diameter Experimental Rig

M	L1	Z	L2	ζ	L3	ζ	L4	ζ	L5	ζ
0.0	164.4	0.0347	329.1	0.0187	496.0	0.0132	661.8	0.0117	827.4	0.0114
0.1	165.3	0.0815	329.9	0.0288	496.4	0.0251	662.5	0.0201	826.8	0.0174
0.2	159.9	0.125	322.0	0.052	489.4	0.0456	654.1	0.0327	808.5	0.0304
0.3					483.3	0.0659	642.7	0.0589	789.5	0.0381

Table 7-3 Damping of 1.0 m Long, 0.0158 m Diameter Experimental Rig

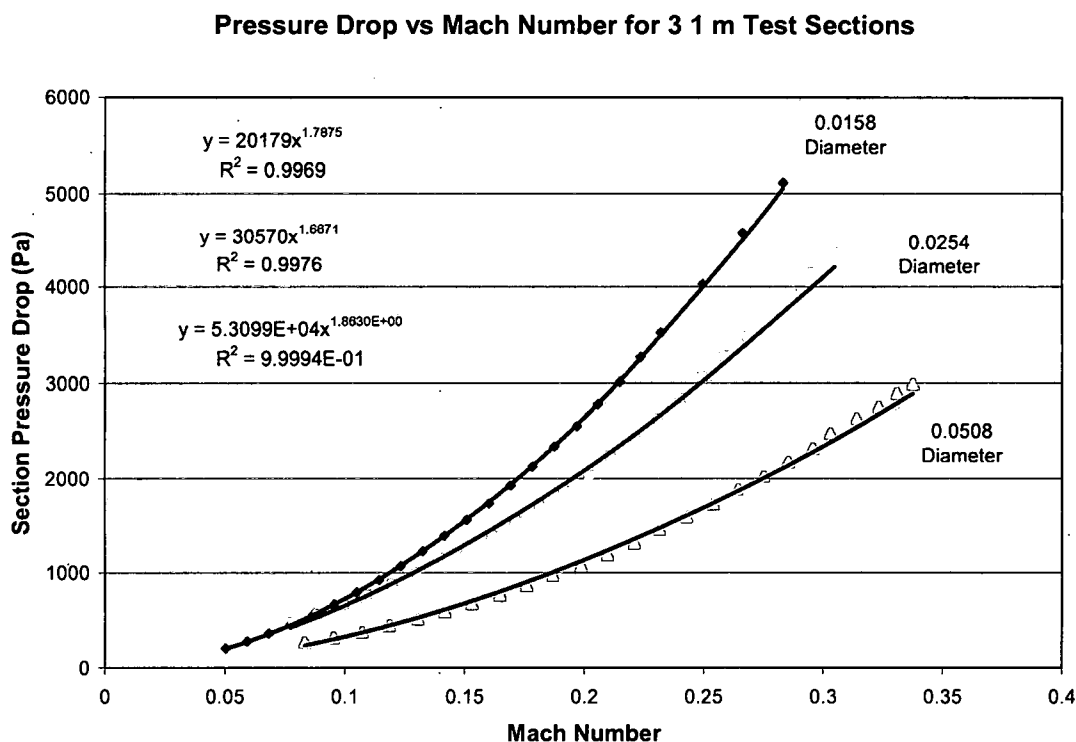


Figure 7-24 Rig Pressure Drop Versus Mach Number for the Three 1 Meter Long Experimental Rigs

The second trend seen in the tabulated damping data concerns the resonant frequency and its relationship to the Mach number. Figures 7-25 to 7-29 are plots of the resonant frequency of a given mode versus the damping ratio. In each plot, there are clusters of data for each of the Mach numbers studied. Comparing the plots, the damping is always highest in the first mode. As the mode number increases, the damping decreases, below 6% for the third and higher modes. This is in agreement with Ingard and Sinhal (1975). For the first two modes there is no other discernible trend in the data.

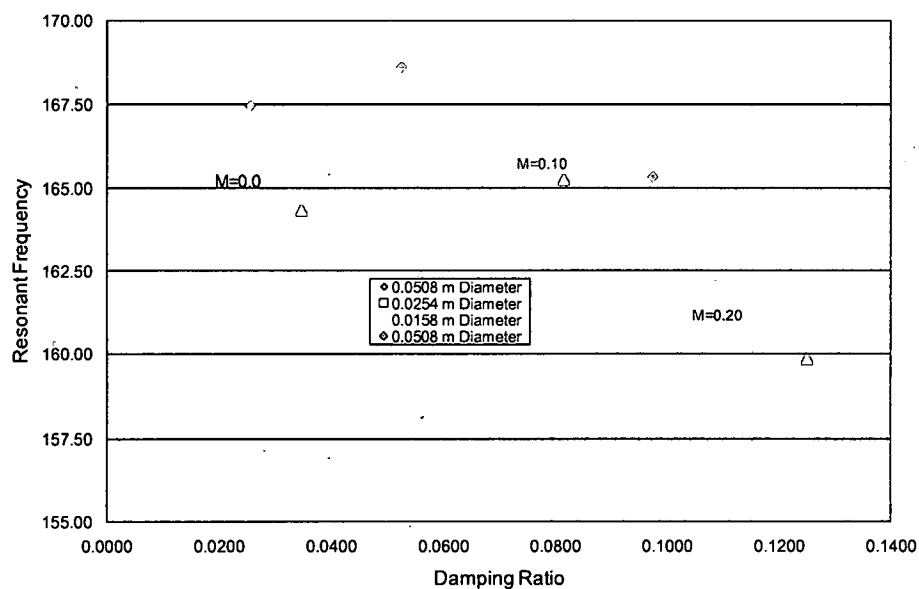


Figure 7-25 Resonant Frequency vs. Damping Ratio for the First Mode Over a Range of Mach Numbers and Experimental Rigs

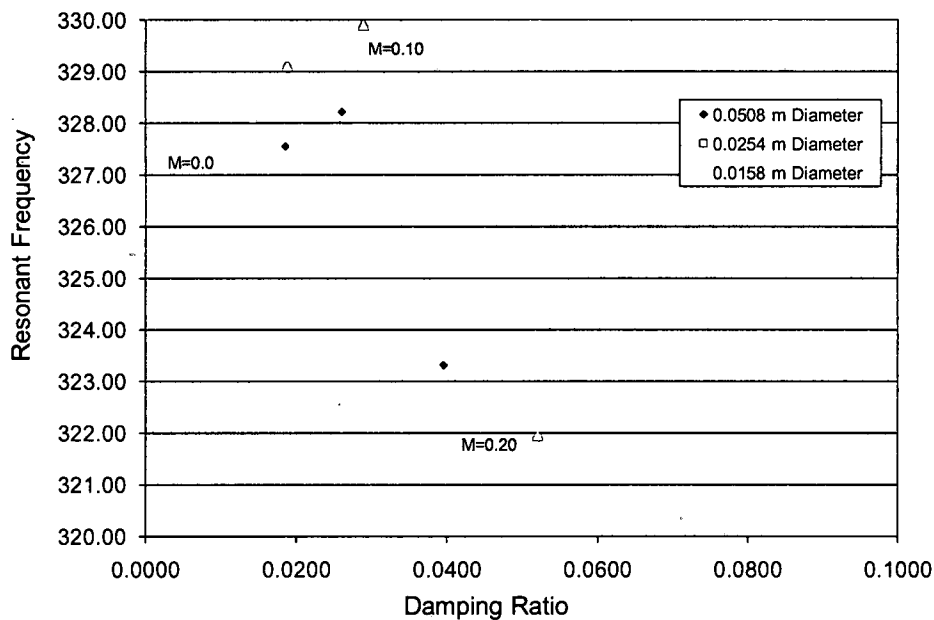


Figure 7-26 Resonant Frequency vs. Damping Ratio for the Second Mode Over a Range of Mach Numbers and Experimental Rigs

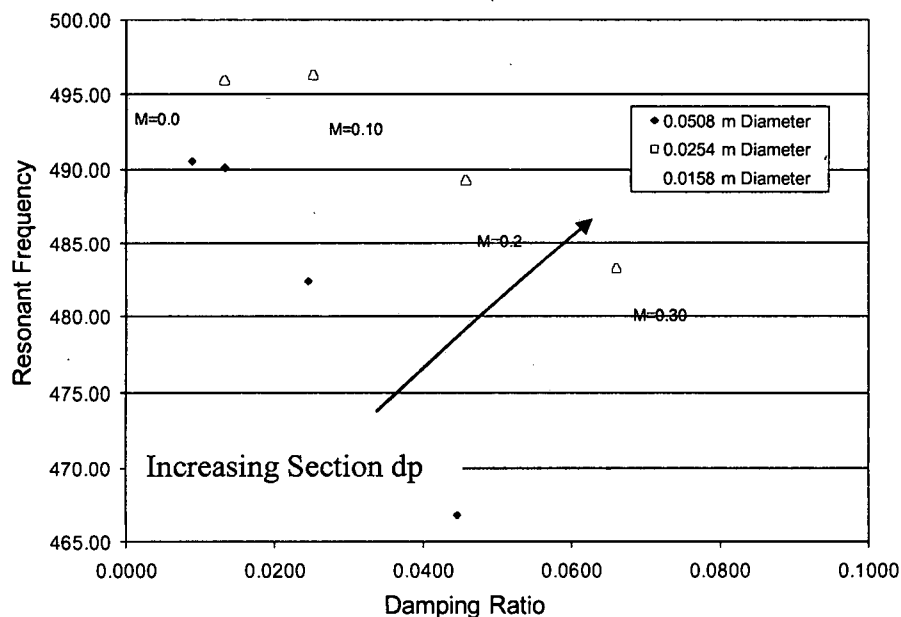


Figure 7-27 Resonant Frequency Versus Damping Coefficient for the Third Mode Over a Range of Mach Numbers and Experimental Rigs

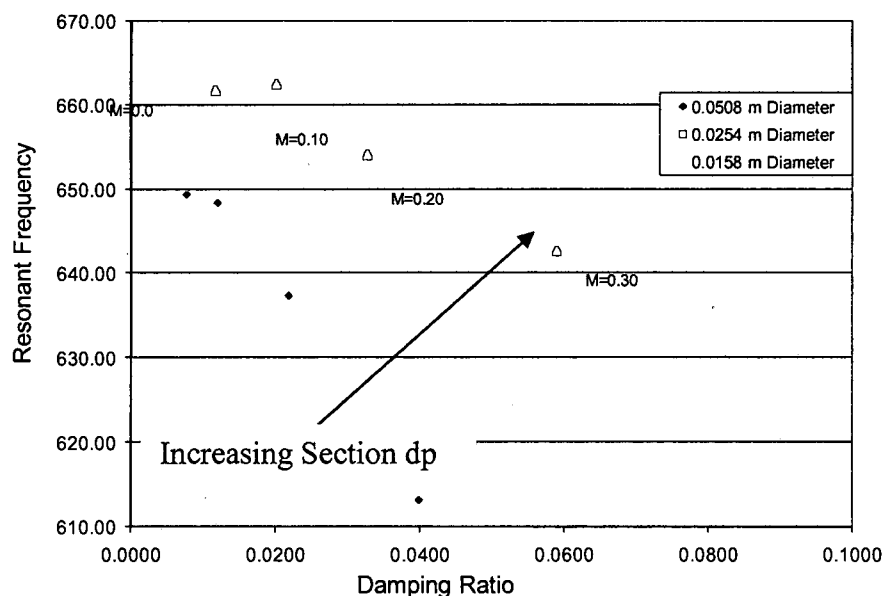
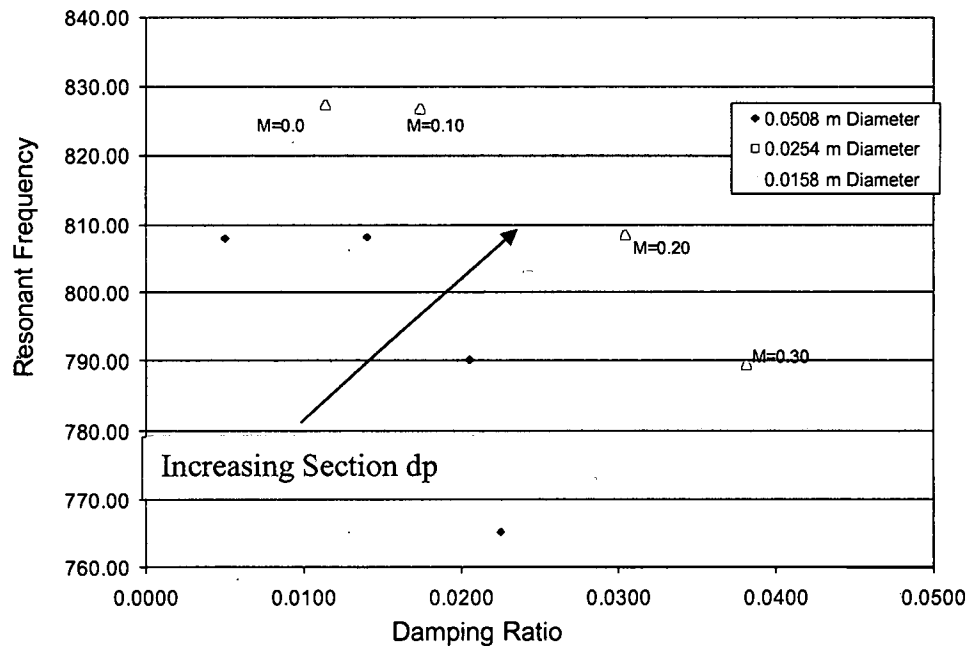


Figure 7-28 Resonant Frequency vs. Damping Coefficient for the Fourth Mode Over a Range of Mach Numbers and Experimental Rigs



**Figure 7-29 Resonant Frequency vs. Damping Coefficient for the Fifth Mode
Over a Range of Mach Numbers and Experimental Rigs**

For the third, fourth and fifth modes, the resonant frequency decreases as the damping increases. This trend is opposite to what is expected for a system with increasing damping. Recall Figure 7-2. Note that as the damping ratio increases, the resonant frequency decreases for the simple second order system. It is further observed that large damping values, greater than 10%, are required to appreciably change the resonant frequency. The results plotted in Figures 7-27, 7-28, and 7-29 are differ from that of the simple second order damped system in Figure 7-2. For the third, fourth, and fifth modes, as the damping increases the resonant frequency increases, not decreases. This is counter to the trend for the simple damped second order system.

Correlation of Turbulence Data to Damping

The final observation when comparing Tables 7-1 through 7-3 is, for a given mode number, the damping associated with the mode at the resonant frequency increases as the Mach number increases. This trend can be explained by comparing the effect of turbulence at the resonant frequency as the Mach number is increased. Figures 7-30, 7-31, and 7-32 depict the Turbulent Kinetic Energy (TKE) spectra for the 1 meter long by 0.0508 meter (2 inch), 0.0254 meter (1 inch), and 0.0158 meter ($\frac{1}{2}$ inch) diameter experimental rigs respectively. These data were obtained using the hot wire probe as described in Section 5. The x axis in the figure is non-dimensionalized by the natural frequency of the first mode without flow. Thus, a value of 1 on the x-axis corresponds to the frequency of the first mode, 2 on the x-axis corresponds to the frequency of the second natural frequency, etc. Examining these plots, the energy extracted from the mean flow increases as the Mach number increases for a given frequency. Thus the turbulence extracts more energy from the flow as the Mach number increases. This increase in turbulent kinetic energy correlates directly to an increase in damping for a given mode as Mach number increases. As stated before in Section 6, the transfer of flow energy to turbulence is seen as the source of damping.

The frequency dependence of damping is the third trend seen in the data tabulated in Tables 7-1, 7-2, and 7-3. For a given Mach number the damping decreases as the order of the mode increases. Insight into the reason for the

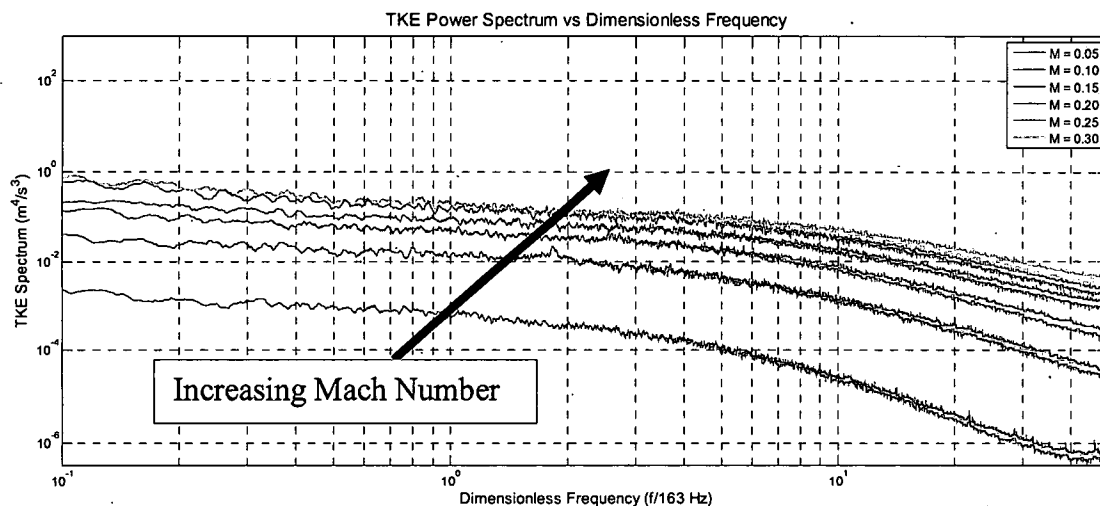


**Figure 7-30 Turbulent Kinetic Energy (TKE) Spectrum for 1m Long, 0.0508m
(2 Inch) Diameter Experimental Rig**

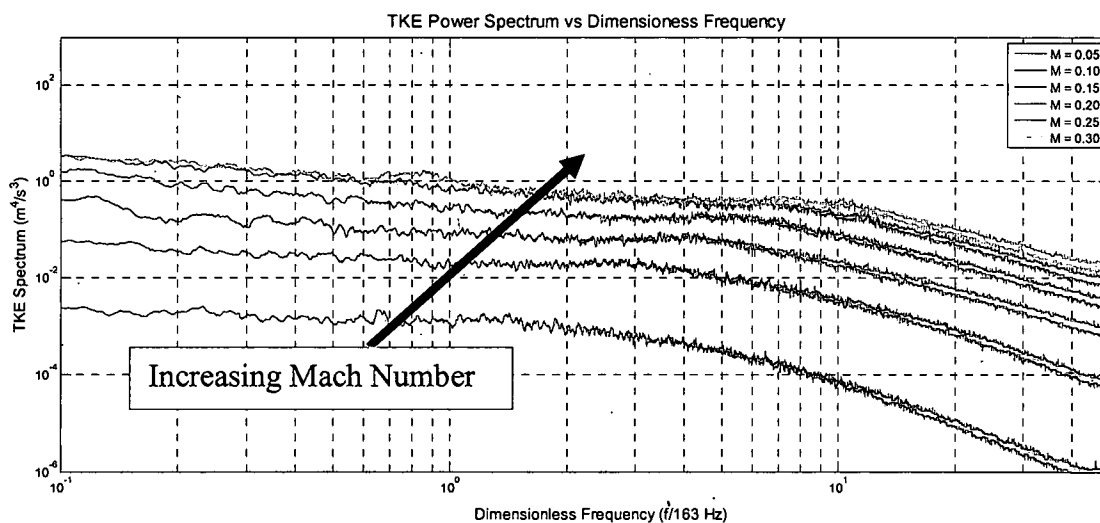


**Figure 7-31 Turbulent Kinetic Energy (TKE) Spectrum for 1m Long, 0.0254m
(1 Inch) Diameter Experimental Rig**

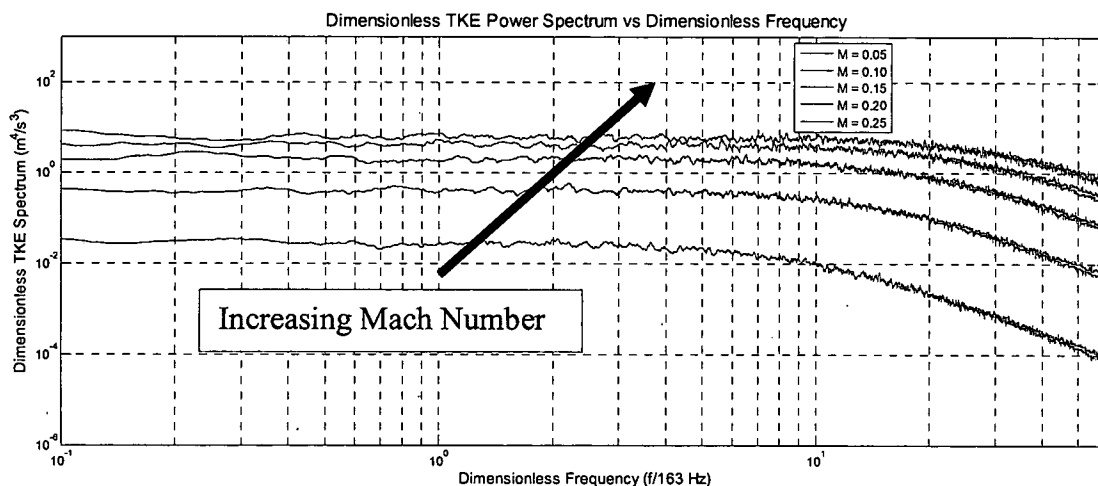


Figure 7-32 Turbulent Kinetic Energy (TKE) Spectrum for 1m Long, 0.0158m (1/2 Inch) Diameter Experimental Rig

decrease in damping as the mode number increases can also be gained by again referring to Figures 7-30 to 7-32. Shear creates turbulence by extracting energy from the flow over the range of turbulent scales. According to Townsend (1993) more energy is extracted at the larger scales than the smaller scales. As frequency increases, past the energy containing eddies region, the energy removal decreases as the frequency of the vortices increases. Examining Figures 7-30 to 7-32, in each case, the turbulent kinetic energy decreases along lines of constant Mach number as frequency increases. When comparing the results in Tables 7-1 to 7-3 to Figures 7-30 to 7-32, the decrease in turbulent energy correlated directly with the decrease in damping as the mode number increases. Turbulence extracts less energy from the higher frequency modes and consequently these modes are damped less.

Analytical Solutions in the Limit and Damping

The effect of convection can also be discerned by studying the analytical solution in the limit as time approaches infinity. Analytical solutions were derived for the homogenous acoustic, homogenous damped acoustic and homogenous convective wave equations. Equations A3-12, A4-16 and A5-10 are repeated here for convenience.

Acoustic Wave Equation Solution:

$$p_n(x,t) = \sin(\pm k_n x) [A_n \cos(\pm \omega_n t) + B_n \sin(\pm \omega_n t)] \quad (\text{A3-12})$$

Damped Acoustic Wave Equation Solution:

$$p(x,t) = e^{-R_2 t} \sin(\pm k_n x) \left[\begin{aligned} &A_n \cos\left(\pm \omega_n \left(1 - \frac{R_2^2}{\omega_n^2}\right) t\right) \\ &+ B_n \sin\left(\pm \omega_n \left(1 - \frac{R_2^2}{\omega_n^2}\right) t\right) \end{aligned} \right] \quad (\text{A4-16})$$

Convective Wave Equation Solution:

$$p(x,t) = A_1 e^{(\omega_n(1-M^2)t + k_n(1+M)x)} + A_2 e^{(\omega_n(1-M^2)t - k_n(1-M)x)} \quad (\text{A5-10})$$

Examining the analytical solutions, the nature of the time response can be studied. To determine the effect of acoustic damping and convection, the time response of the analytical solution is studied in the limit as time becomes infinite. For the Acoustic Wave Equation:

$$\begin{aligned}
p_n(x, \infty) &= \lim_{t \rightarrow \infty} (\sin(\pm k_n x) [A_n \cos(\pm \omega_n t) + B_n \sin(\pm \omega_n t)]) \\
&= \lim_{t \rightarrow \infty} (A_n, B_n)
\end{aligned}$$

The limit is bounded by the greater of $\pm A_n$, and $\pm B_n$. In either case each is constant, neither growing nor decaying as time approaches infinity.

For the wave equation with acoustic damping, taking the limit of Equation as time approaches infinity:

$$\begin{aligned}
p(x, \infty) &= \lim_{t \rightarrow \infty} \left(e^{-R_2 t} \sin\left(\frac{n\pi x}{L}\right) \left[A_n \cos\left(\sqrt{(\omega_n^2 - R_2^2)}t\right) + B_n \sin\left(\sqrt{(\omega_n^2 - R_2^2)}t\right) \right] \right) \\
&= \lim_{t \rightarrow \infty} (e^{-R_2 t}) = 0
\end{aligned}$$

As before $\pm A_n$, and $\pm B_n$ bound the amplitude maxima and minima. The first exponential with time, governs the rate of growth or decay of the pressure. As time approaches infinity the amplitude of this term will tend to zero. Thus damping has the effect of decaying the time response as time increases.

Convection can be studied in the same manner as acoustic damping. Modifying Equation A5-10 to isolate the Mach number effect on the time response results in Equation A5-11. The first exponential in the equation is of the same form as the

$$p(x, t) = e^{-M^2 \omega_n t} \left[A_1 e^{\omega_n t + k_n (1+M)x} + A_2 e^{\omega_n t - k_n (1-M)x} \right] \quad (\text{A5-11})$$

first exponential of the damped acoustic wave solution. In the limit as time approaches infinity the amplitude has a maximum and minimum bounded by $\pm A_1$, and $\pm A_2$. As with the acoustic damping, the first exponential with time governs the rate of growth or decay of the pressure. As time approaches infinity, the

amplitude of this term also will tend to zero. Thus convection also has the effect of decaying the time response as time increases.

Numerical and Experimental Transient Analysis

In the previous section the results of models and experiments were studied in frequency domain. The main result from the section is that the flow damps the modes, but the shape of the modes are preserved. In this section the effect of flow will be studied in the time domain. The analytical solutions will be studied first to gain insight into the behavior of standing waves that occur without flow and propagating waves that occur with convection. "Data" were also taken by exciting the experimental/model rigs with a sine wave at discrete resonant frequencies. The simultaneously fluctuating response of the pressure at each measurement location at each instant in time was recorded. The resonant frequencies were obtained from the FRF data in the previous section. The "data" was taken with the finite element models and the experimental longitudinal and circumferential rigs. Snapshots of the data for each pressure location are plotted at an instant in time. Several snapshots will be presented together to show the time evolution of the response of the experimental/model rigs. The time evolutions will be presented without and with flow and compared/contrasted.

Studying the analytical solutions to the varying wave equations can provide insight into the behavior of the waves. The effect of damping and convection on the resonant frequencies (ω_n) and wave number (k_n) can be

discerned by comparing the solutions directly. Three analytical solutions were derived for the acoustic, damped acoustic and convective wave equations.

Comparing the time and spatial portions of the solutions can lend insight into the effect that damping and convection have on the resonant frequencies and wave numbers of the waves. For the acoustic equation the waves add to form a single standing wave whose shape is constant, but whose magnitude changes in time. Comparing the time portion of the solutions (Equations A3-12, A4-16, and A5-10), damping and convection cause a similar shift in the resonant frequency of the wave. In the solution for damped acoustics (Equation 7-6), as the damping is increased the resonant frequency decreases. This is also true for convective wave propagation (Equation 7-7). As the Mach number of convection is increased the resonant frequency decreases.

$$\omega_{\text{resonant, AcousticDamping}}^2 = \omega_n^2 \left(1 - \frac{R_2^2}{\omega_n^2} \right) \quad (7-6)$$

$$\omega_{\text{resonant, Convection}}^2 = \omega_n^2 (1 - M^2) \quad (7-7)$$

Comparing the spatial portion of equations A3-12, A4-16, and A5-10, has a markedly different result. For the wave equation and the damped wave equation the wave numbers of the left and right running waves are the same, resulting in a single standing wave. Convection, though, has an effect on the spatial portion of the solution. Convection changes the effective wave number of the propagating waves (Equations 7-8 and 7-9). For waves traveling with the flow (Equation 7-8) the effective wave number increases, decreasing the wave length. For the waves traveling against the flow (Equation 7-9) the effective

wave number is reduced, increasing the wave length of the waves. The analytical result for convection hints that the sum of the left running and right running waves does not form a standing wave.

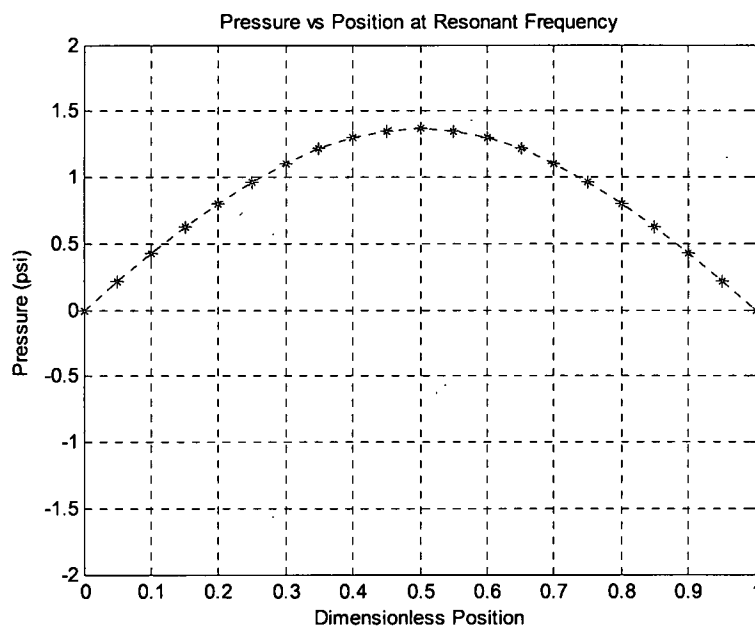
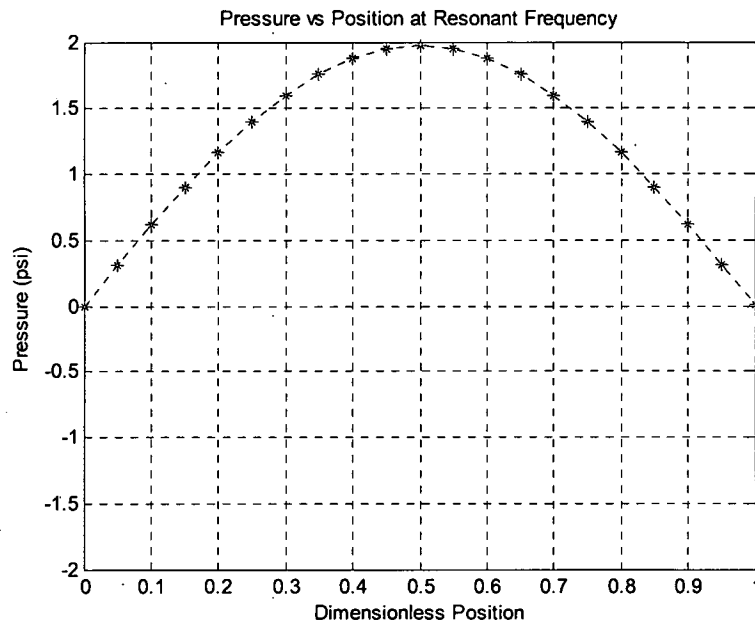
$$k_x^+ = k_n(1 + M) \quad (7-8)$$

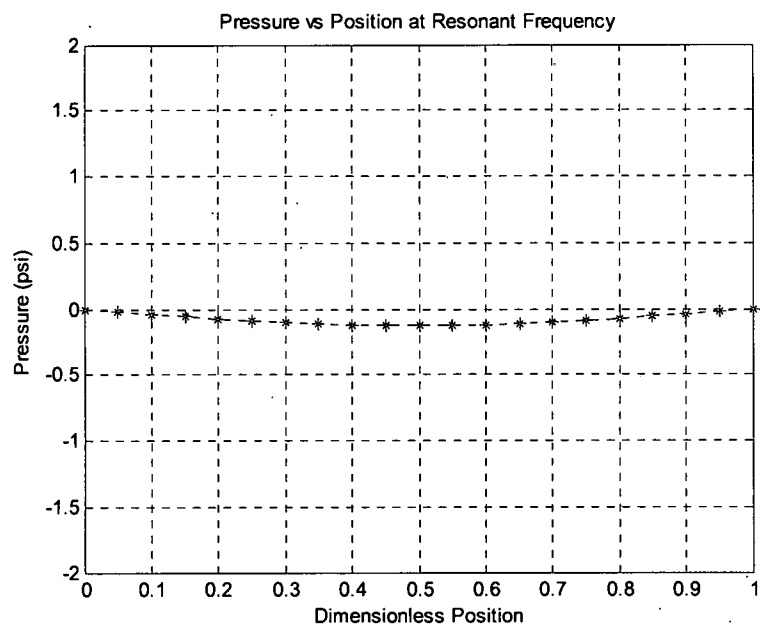
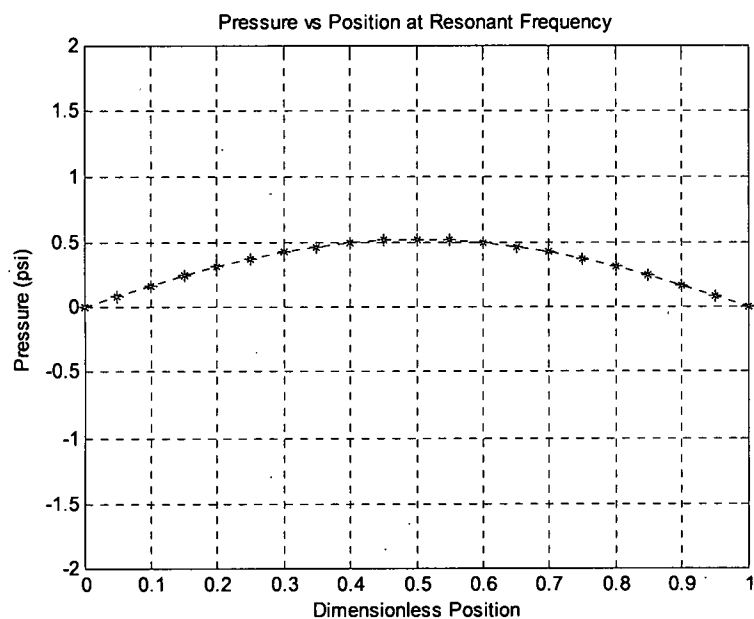
$$k_x^- = -k_n(1 - M) \quad (7-9)$$

To verify the assertion that convection changes the nature of the propagation of the standing waves, time domain data were taken to shed further light on the effect of convection. Second order accurate central difference models for the Navier Stokes Equations are mathematically unstable and require complicated differencing schemes to get transient solutions. Because of this, models of the experimental rigs were constructed and tested with finite element analysis. The weak form mode of COMSOL was used to model Equations 4-1, 4-2 and 4-3. The Mach number was varied to achieve convective only, sheared only, and combined convective and sheared equations for wave propagation. The transient solutions were obtained by using the transient analysis mode in COMSOL. The response of the pressure to the excitation at each computational point, at each instant in time was recorded.

The plots in Figure 7-33 are results of the rig excited at the resonant frequency of the first mode. The plots in Figures 7-34 are results of the rig excited at the resonant frequency of the second mode. The figures are a succession of snapshots of the pressure at each computational point in time for the acoustic wave equation model of the longitudinal rig. Each successive

snapshot depicts the response of the pressure at a later instant in time. For the first mode, Figure 7-33, there are two nodes, one at either end of the rig. As time increases the center pressure is always maximum and corresponds to the location of the anti-node. With increasing time, the magnitude changes, but





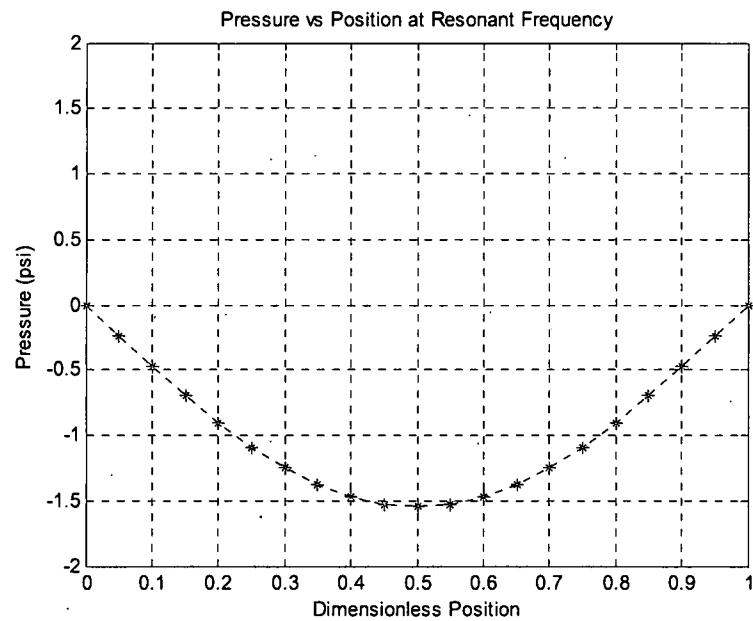
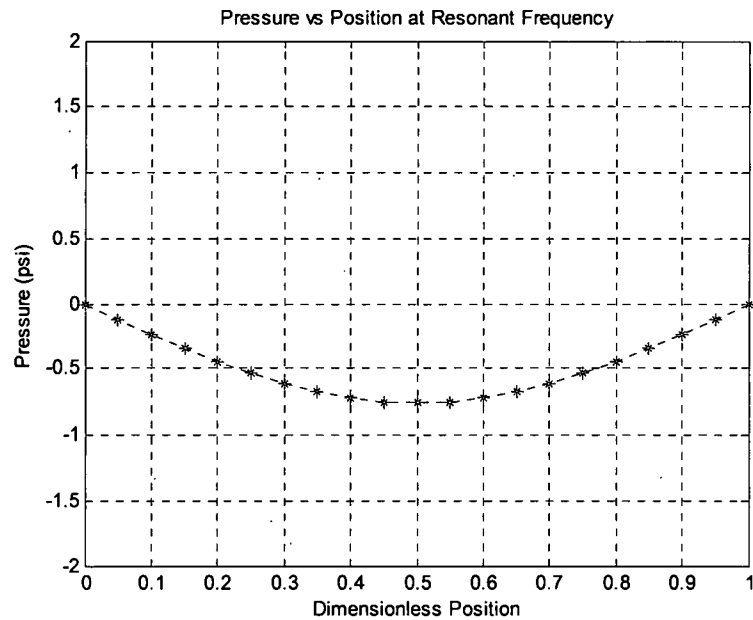
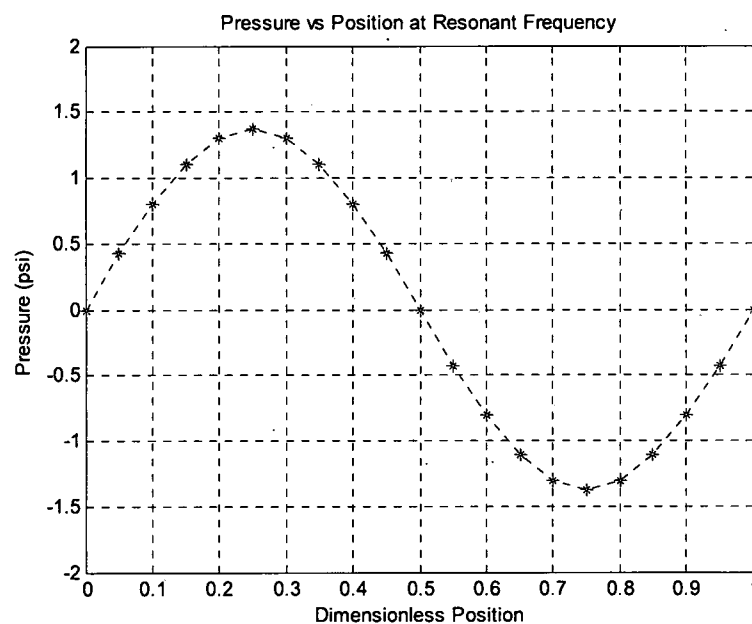
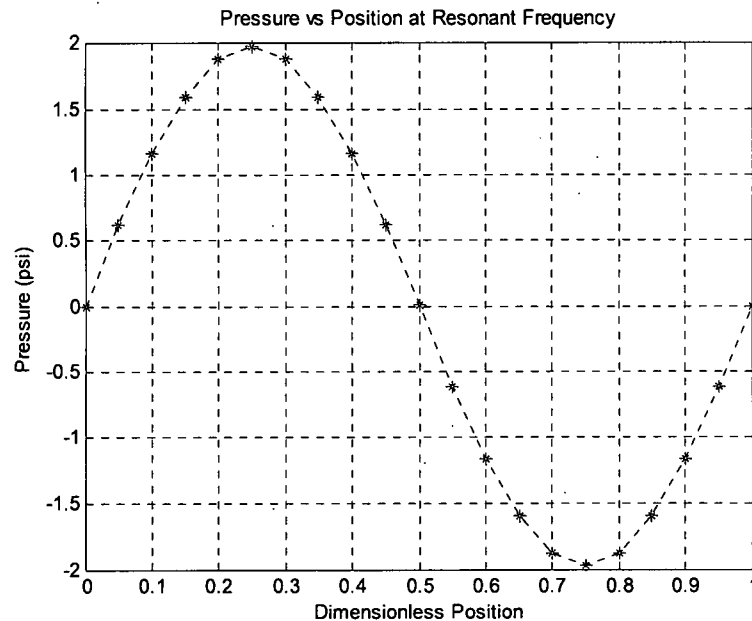
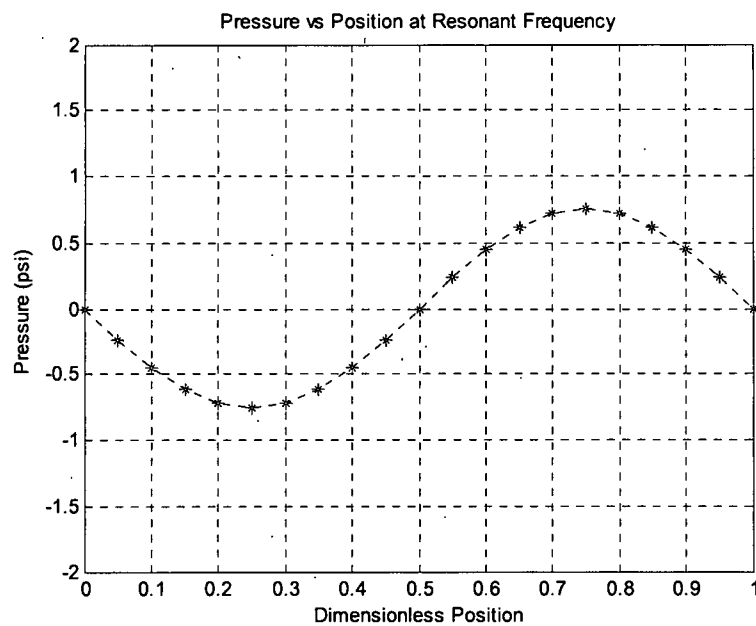
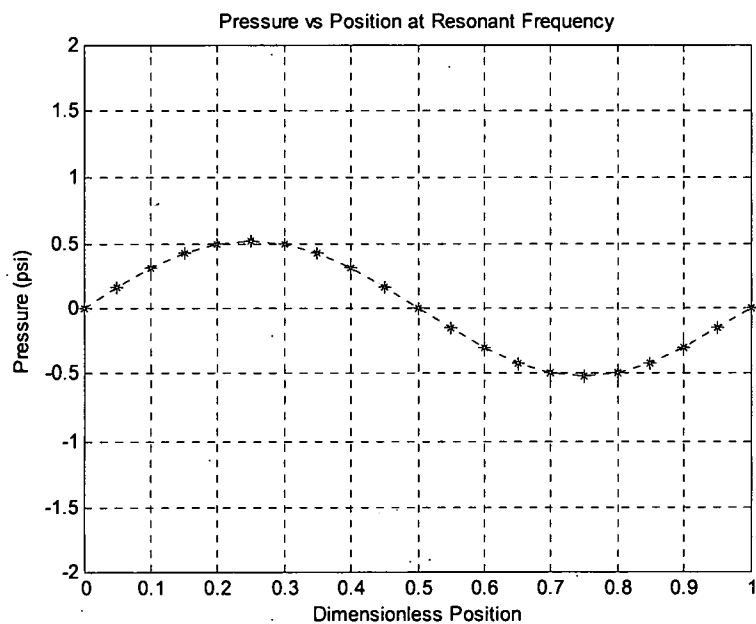


Figure 7-33 Response of the 1-D Acoustic Wave Equation, First Longitudinal Mode

remains symmetric about the center of the experimental rig. The anti-node is always in the center of the rig, and the nodes are always anchored at the ends of the rig. For the second mode (Figures 7-34) there are three nodes, two at the

ends and one at the center. There are also two anti-nodes at $x/L = 0.25$ and 0.75 locations. With increasing time, the magnitude of the wave increases and decreases, but the location of the nodes and anti-nodes is stationary. There is also a symmetry plane at the center of the rig.





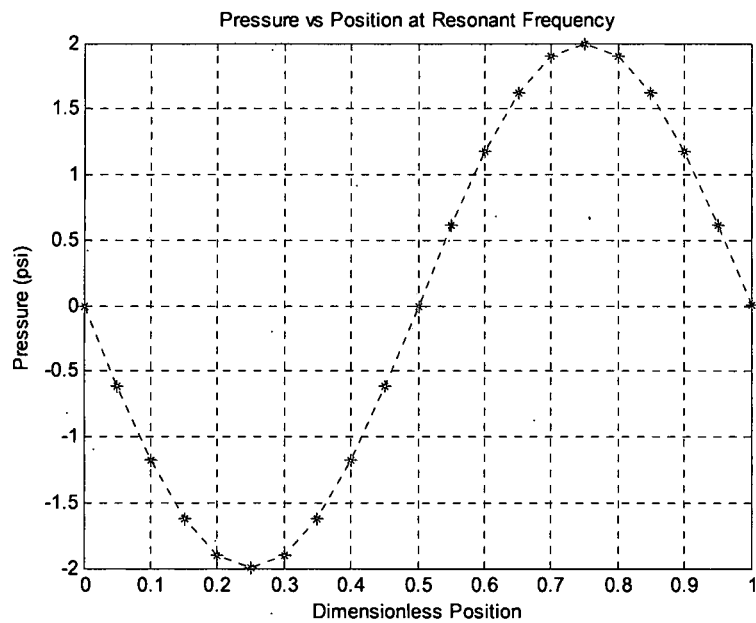
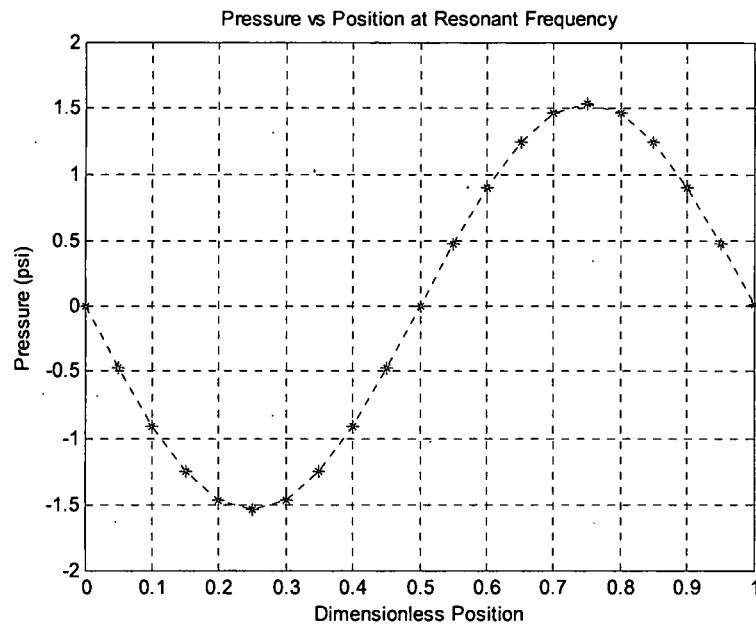
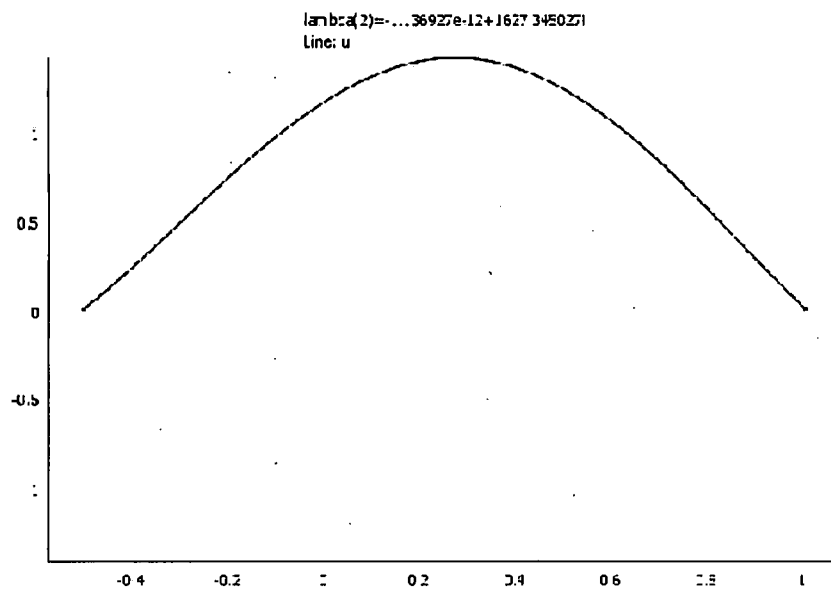
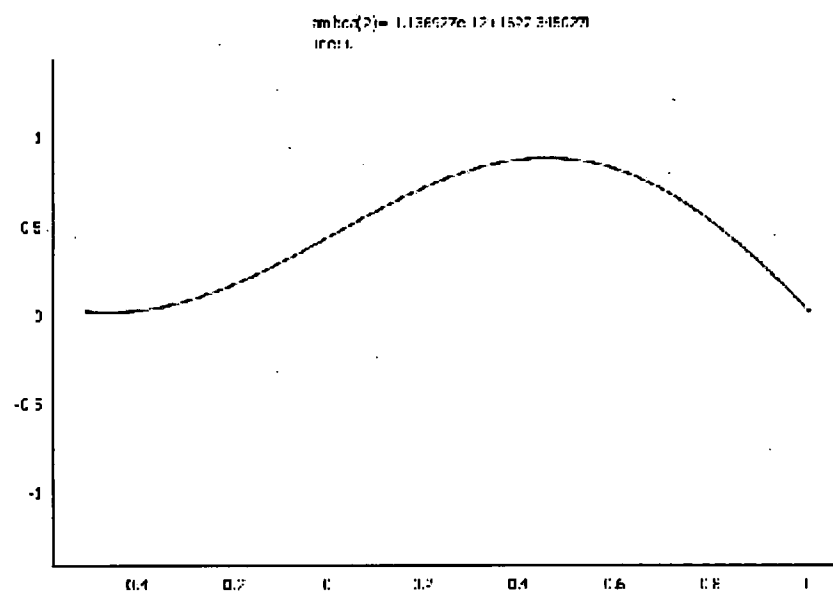
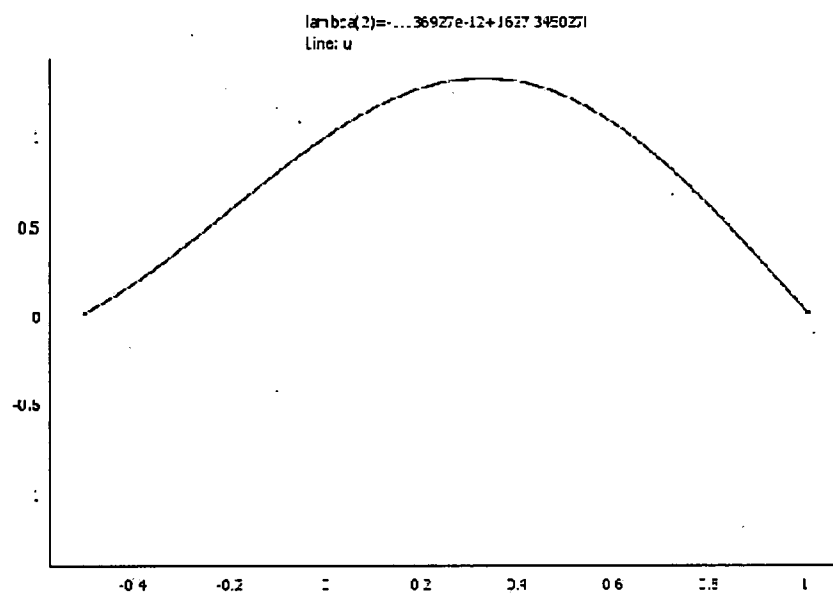


Figure 7-34 Time Response 1-D Acoustic Wave Equation, Second Longitudinal Mode

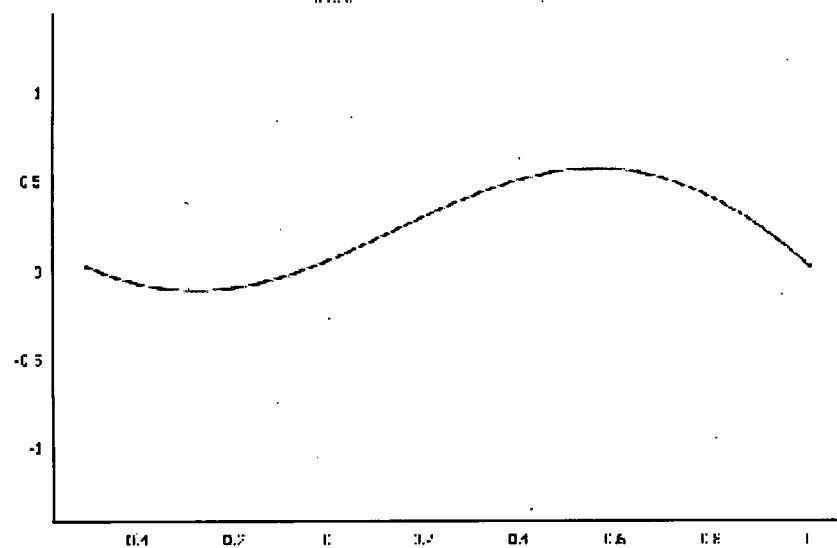
The plots in Figures 7-35 depict the time series of the finite element model for the first mode for convection only. The Mach number used in the simulation

was equal to 0.10. The shape of the time response is very dissimilar to that Figure 7-33. As time increases there is no clear symmetry in the figures. In the various plots in Figure 7-35 the location of the minimum, maximum, and zero pressure are no longer stationary and moves through the rig as time increases.

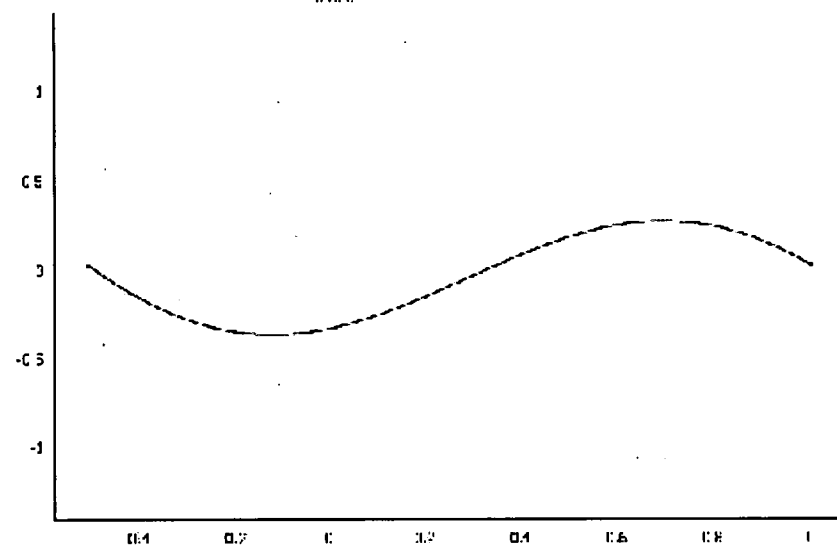


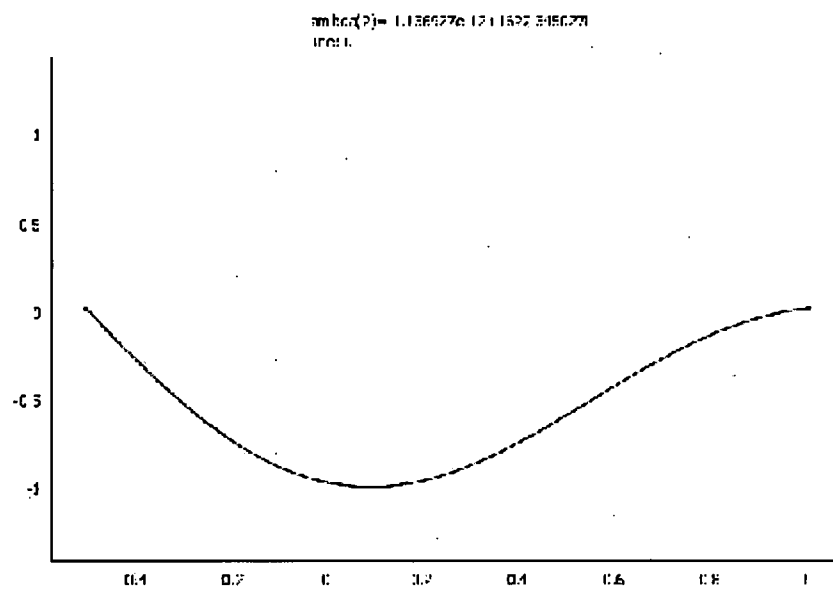
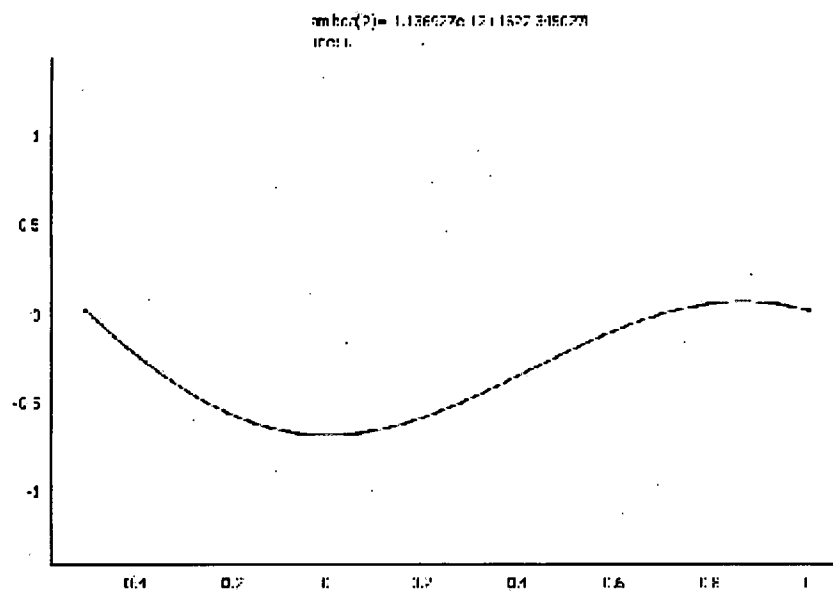


amhc(2)= 1.136627e 12 1.1327 3.186627
 ipol:1



amhc(2)= 1.136627e 12 1.1327 3.186627
 ipol:1





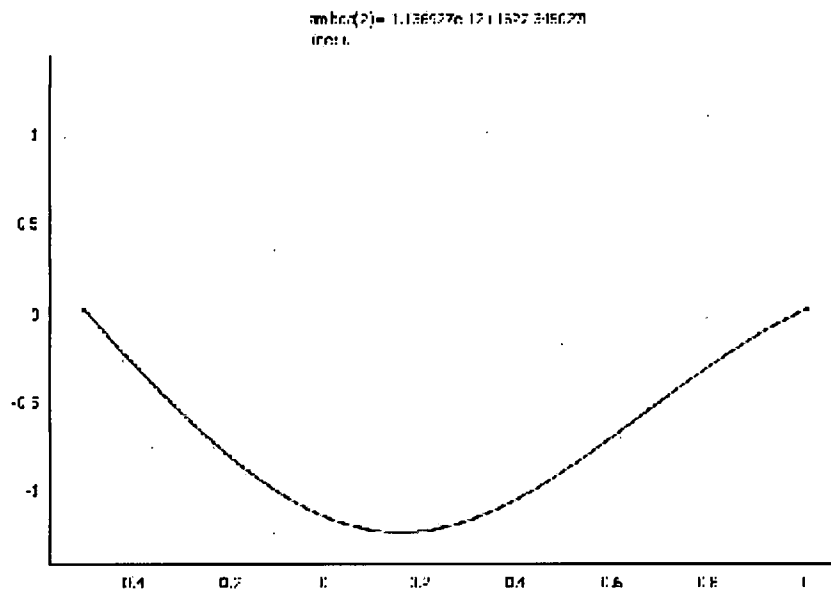
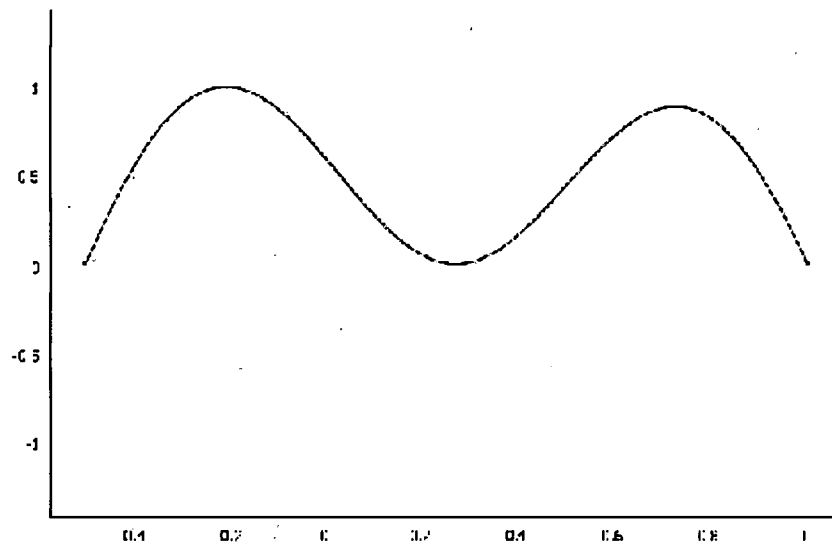


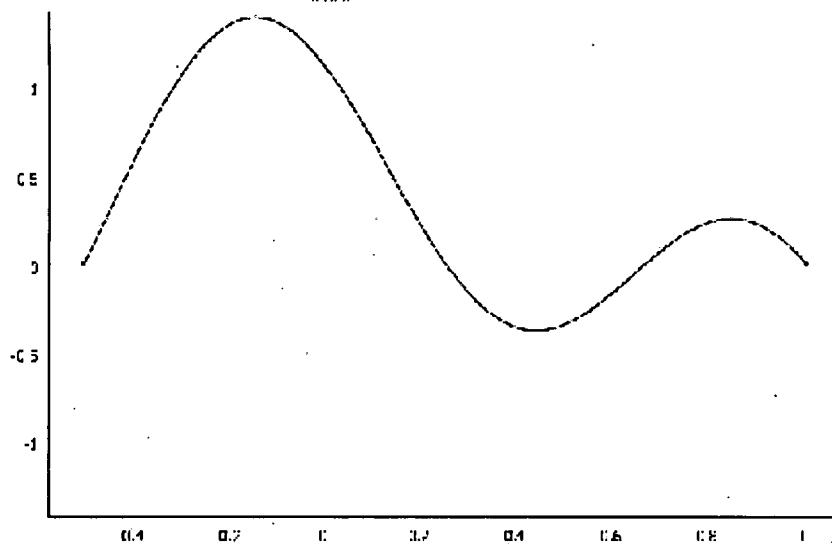
**Figure 7-35 Time Series of Convective Wave Equation for the First Mode,
Mach Number = 0.10**

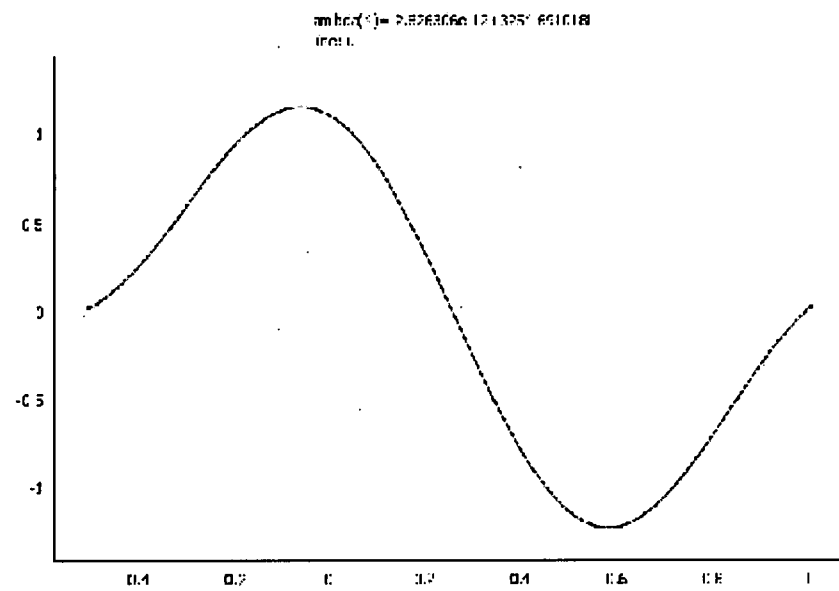
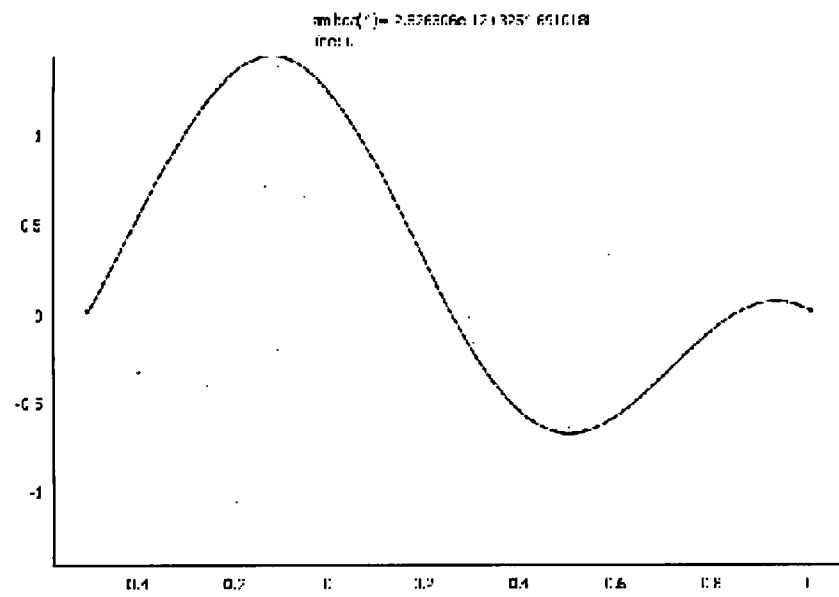
The plots in Figures 7-36 are the simulated time responses of the FEA model of the convective wave equation. In this series the second mode is excited and the Mach number was equal to 0.10. Like the comparison of Figures 7-33 to 7-35, the shape of the time response is very dissimilar to that of Figure 7-34. In all of the plots, the location of the minimum, maximum, and zero pressure move through the rig as time increases. The time response is no longer symmetric with respect to the center of the rig.

ambrq(*)= 0.576306e 12 1.325° 691018
inr:1.

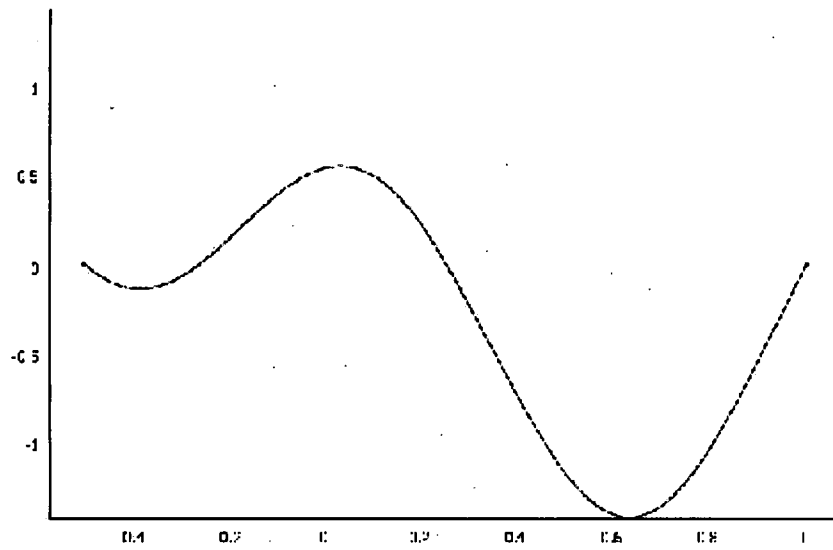


ambrq(*)= 0.576306e 12 1.325° 691018
inr:1.

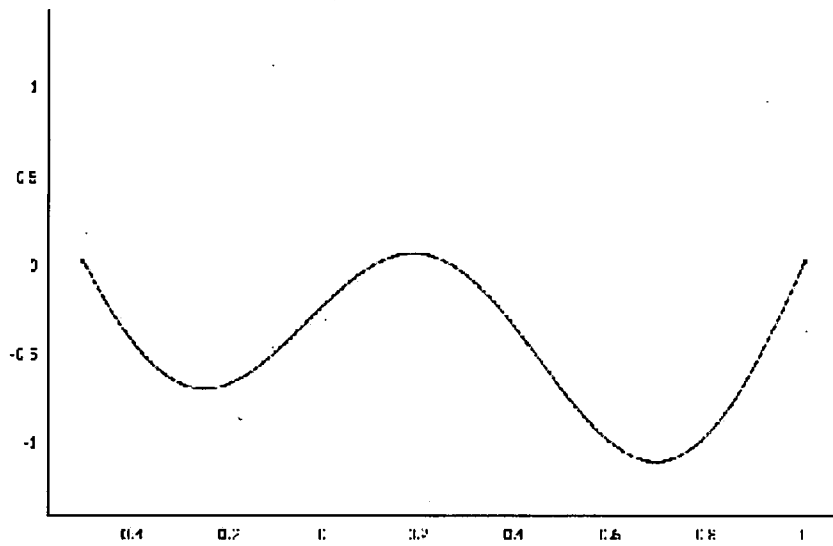




ambr(1) = 0.526306e 12 (325° 691018)
 ir(1)



ambr(1) = 0.526306e 12 (325° 691018)
 ir(1)



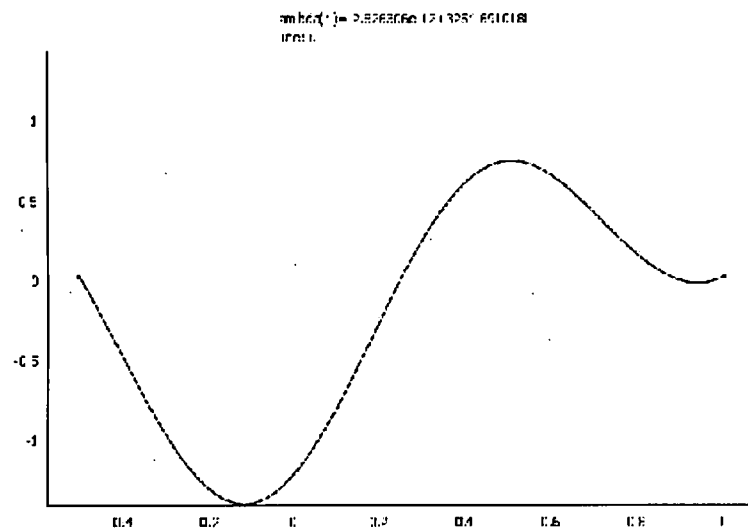
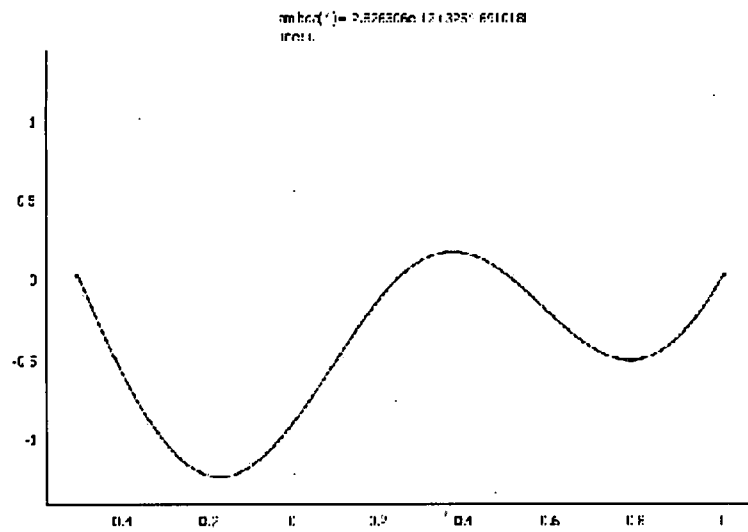
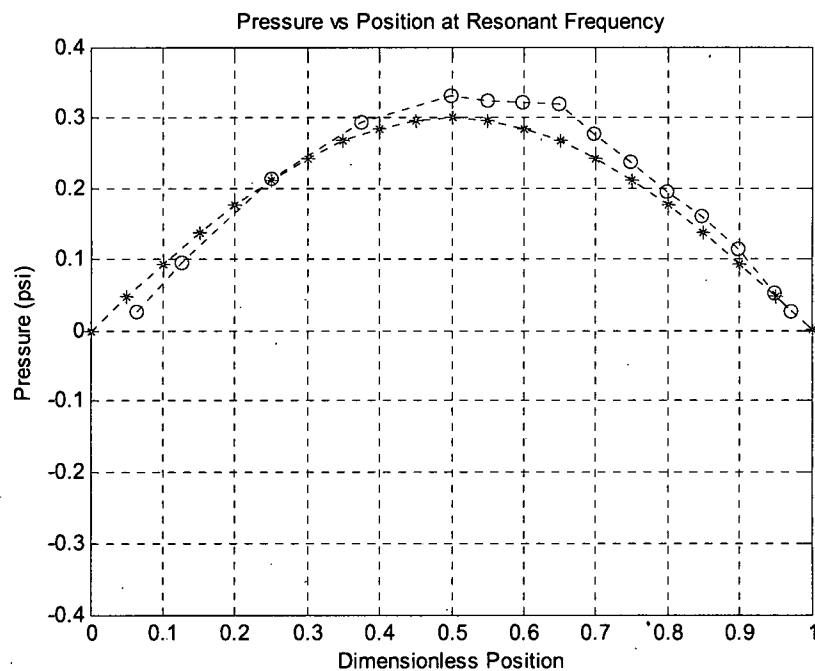
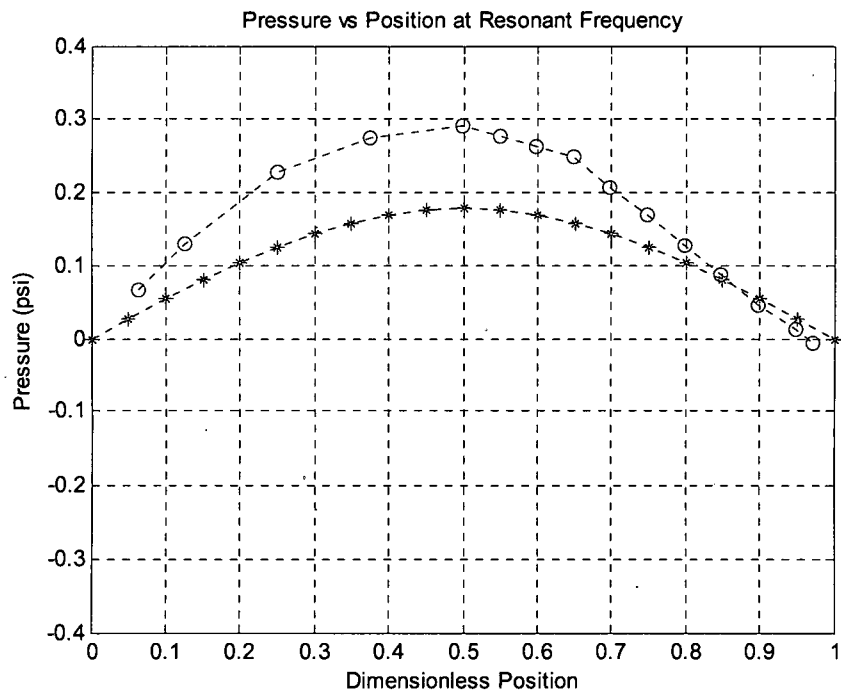
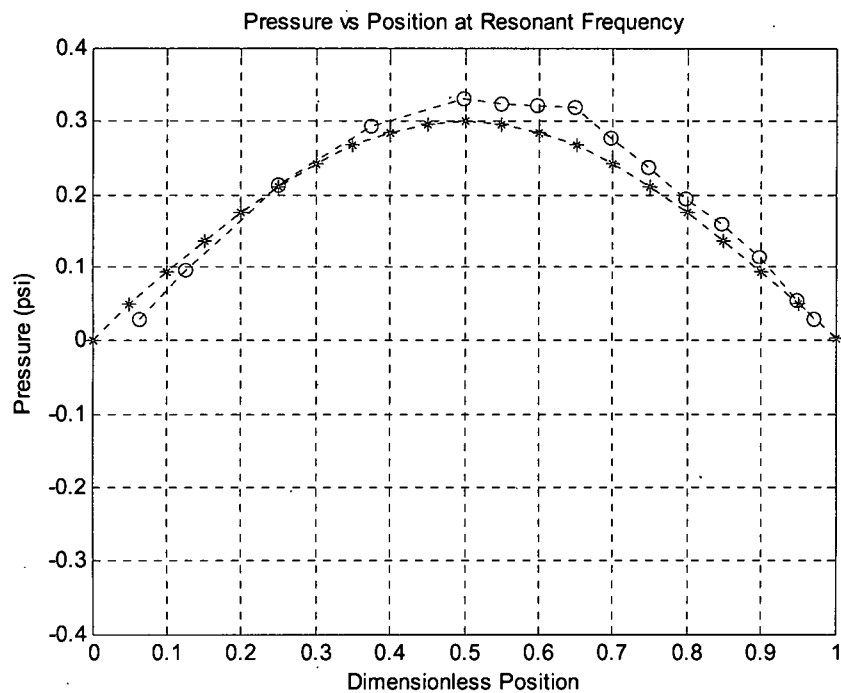
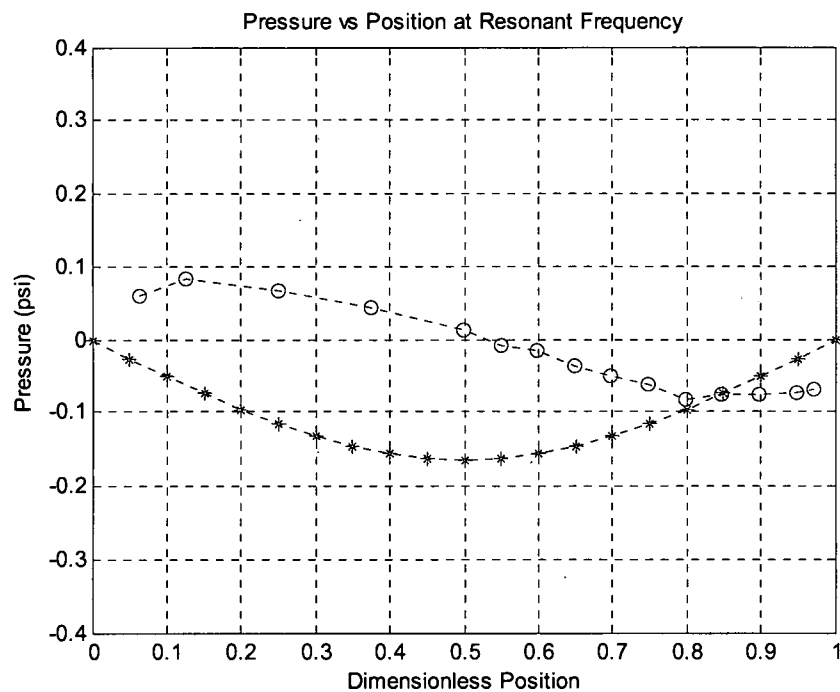
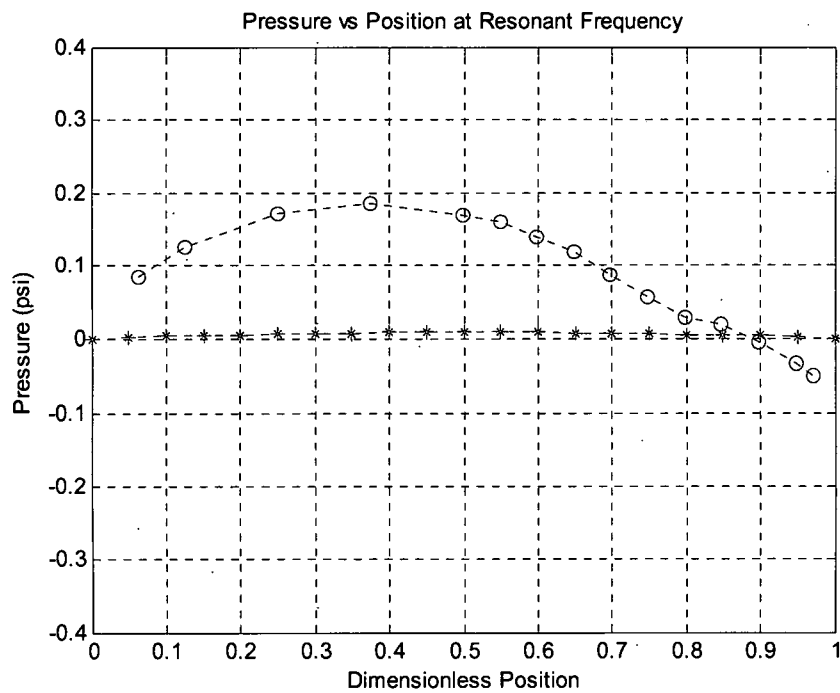


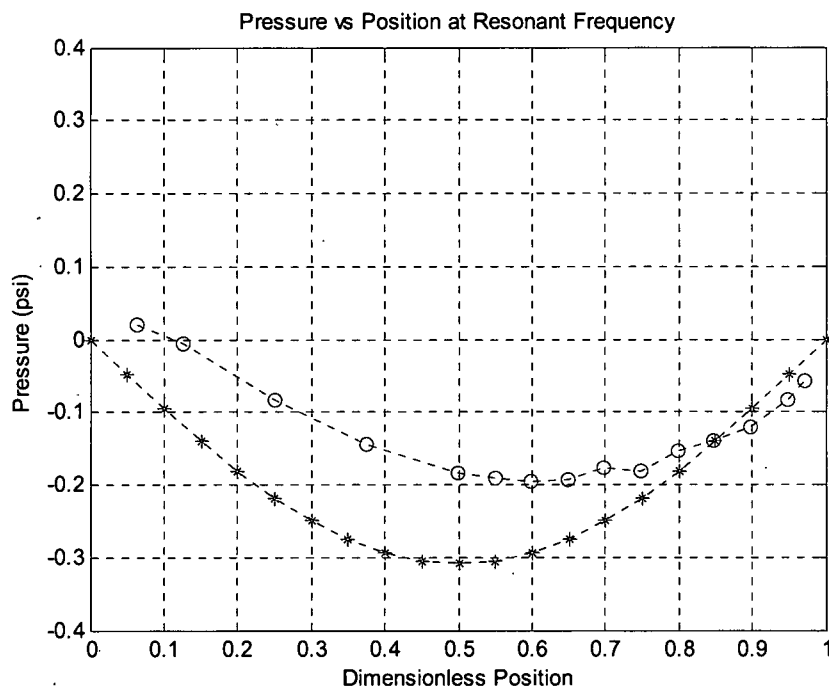
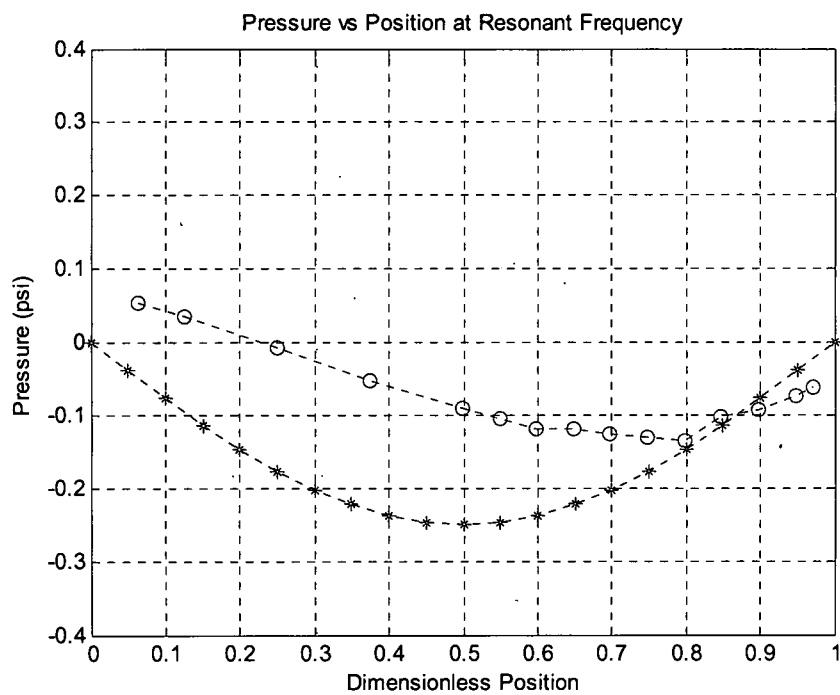
Figure 7-36 Time Series of Convective Wave Equation for the Second Mode,
Mach Number = 0.10

Figures 7-37 and 7-38 depict the response of the two inch experimental longitudinal rig to the sine wave exciting the first and second modes, respectively. The flow Mach number was 0.10. In both sets of plots, the blue line with the "o" marker is the experimental data. The red line with the "x" marker is the analytical solution for the acoustic wave equation for comparison. In Figures 7-37 the two nodes at the ends of the rig are clearly visible throughout the entire time series. Like the FEA simulation for the first mode (Figures 7-35), the location of the minimum, maximum, and zero are no longer stationary and move as time increases. Although the location of maximum pressure moves in time, averaged over time, the anti-node, still resides in the center of the experimental rig. This is clearly visible in the mode shape plot for the first mode, Figure 7-16.









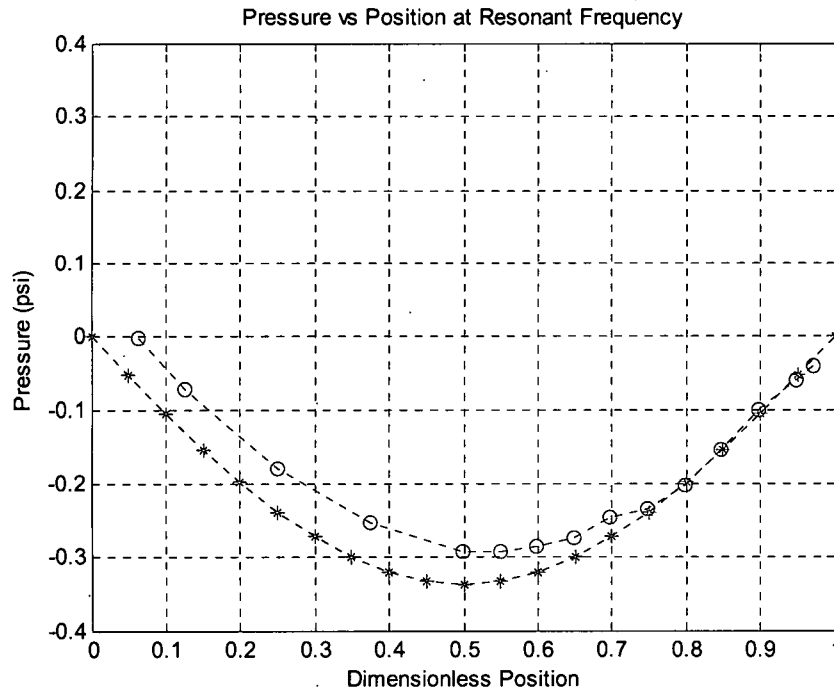
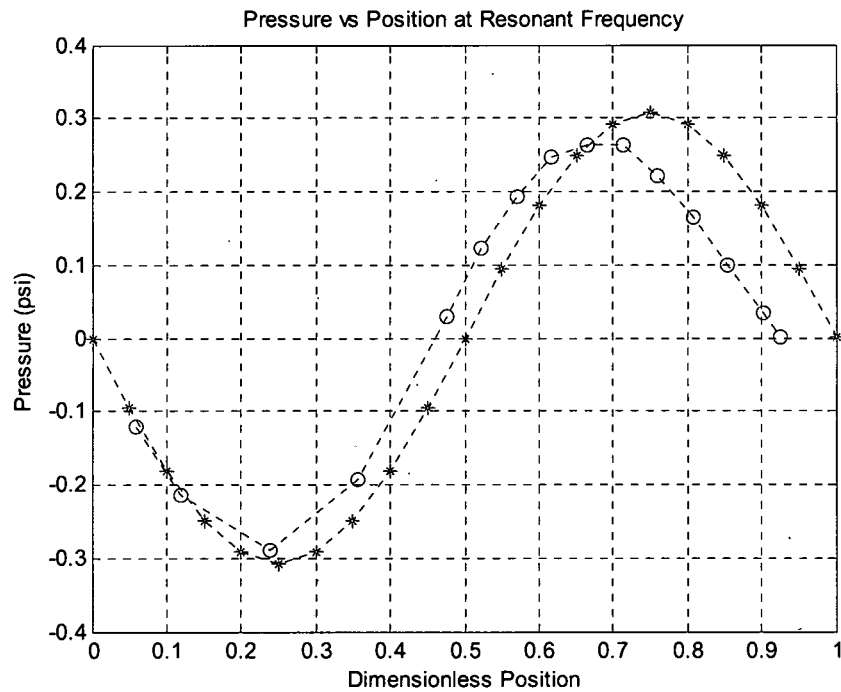
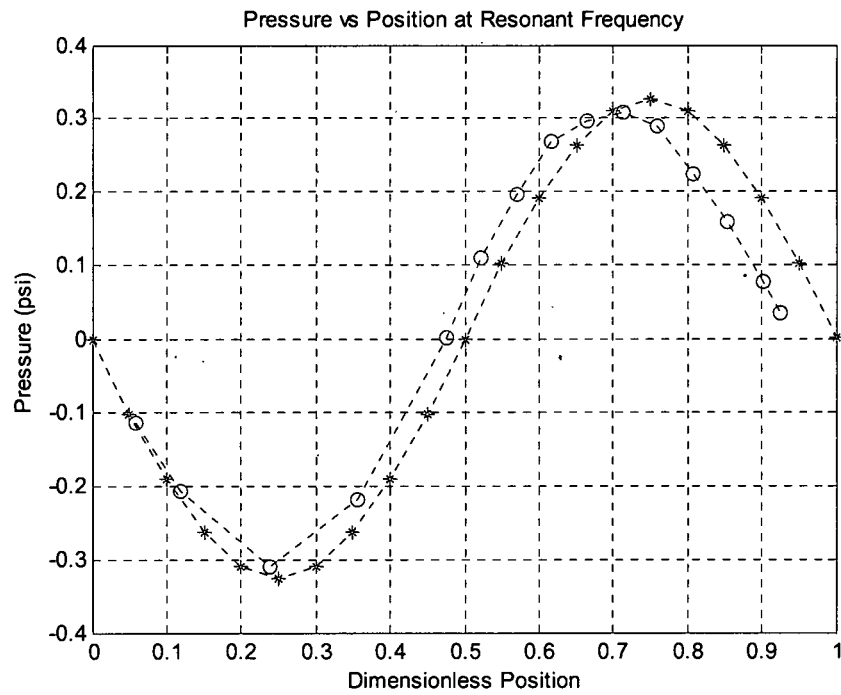
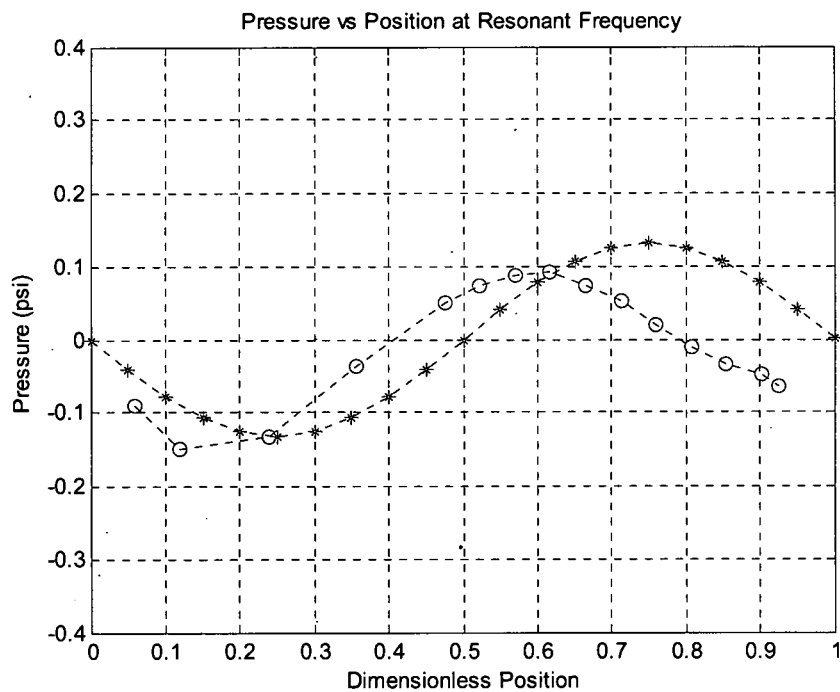
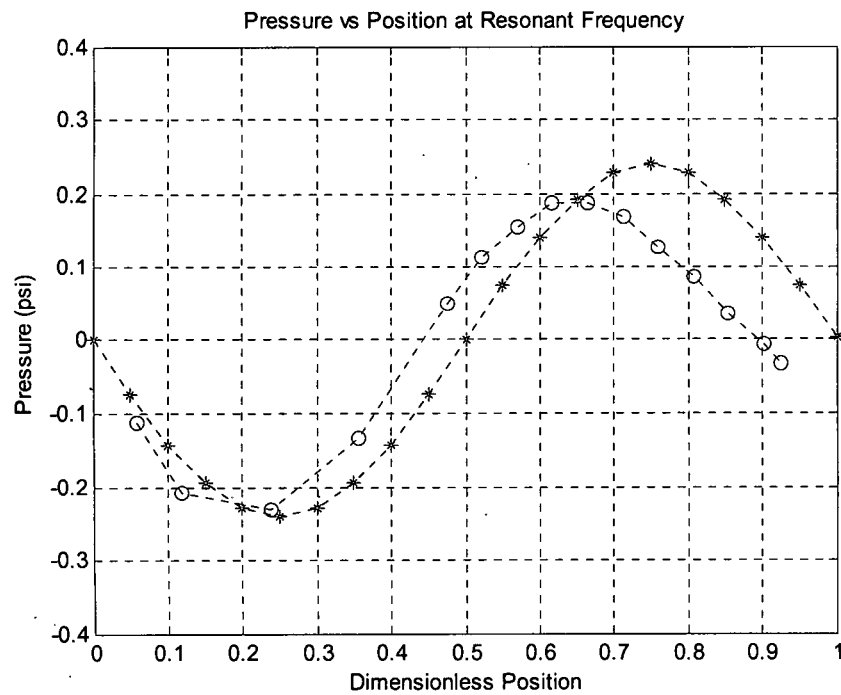
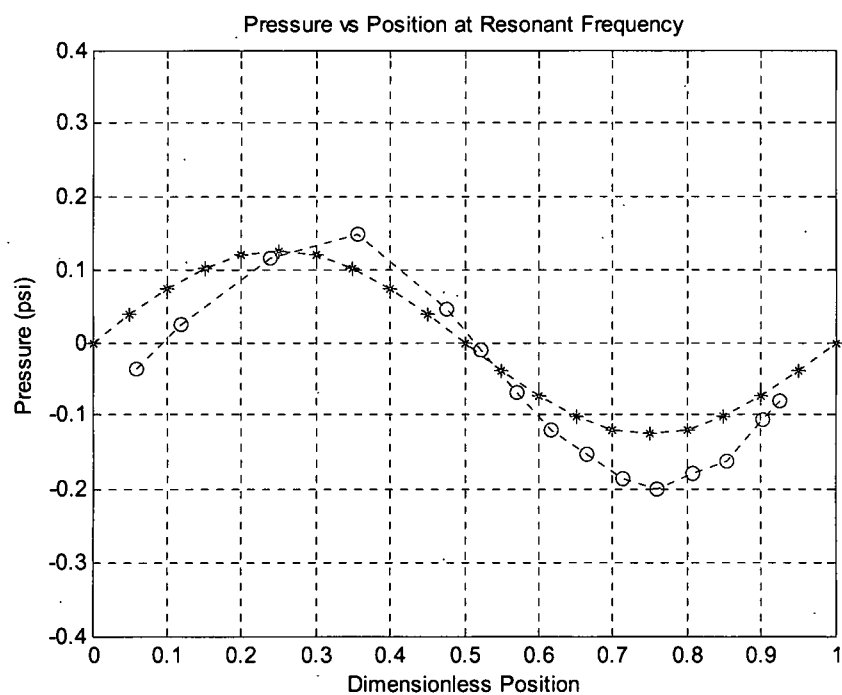
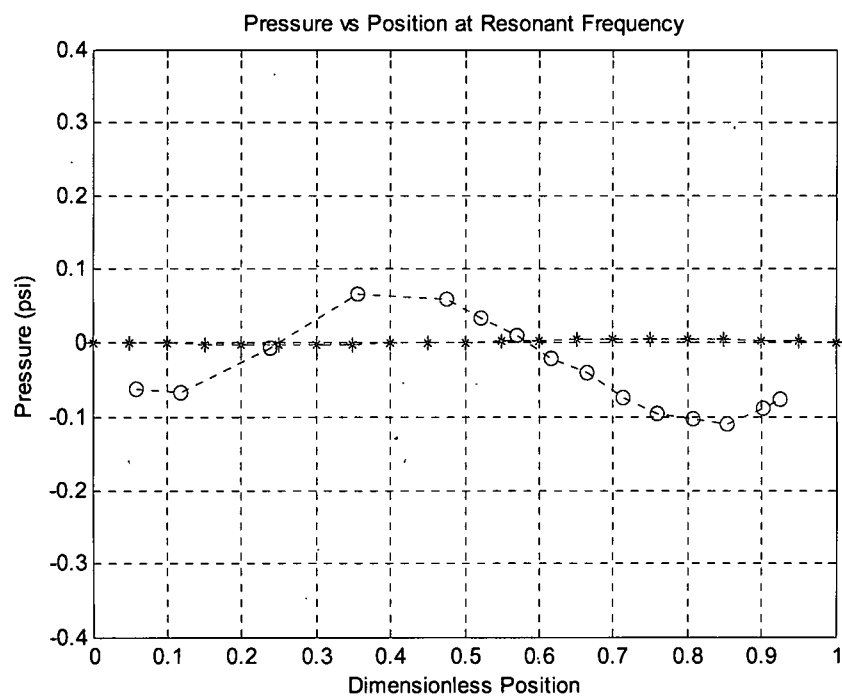


Figure 7-37 Experimental Time Series of the Longitudinal Rig for the First Mode, Mach Number = 0.10

The experimental time response for the second mode (Figure 7-38) is similar to the time response of the FEA model with convection (Figure 7-36). For the case with flow the ends remain stationary and are nodes. The location of the minimum, maximum, and zero pressure are no longer stationary and move as time increases. As with the first mode, even though the location of minimum, maximum, and zero pressure moves in time the anti-nodes still reside at the one-quarter and three-quarter locations of the experimental rig. This is clearly visible in the mode shape plot for the first mode, Figure 7-17.

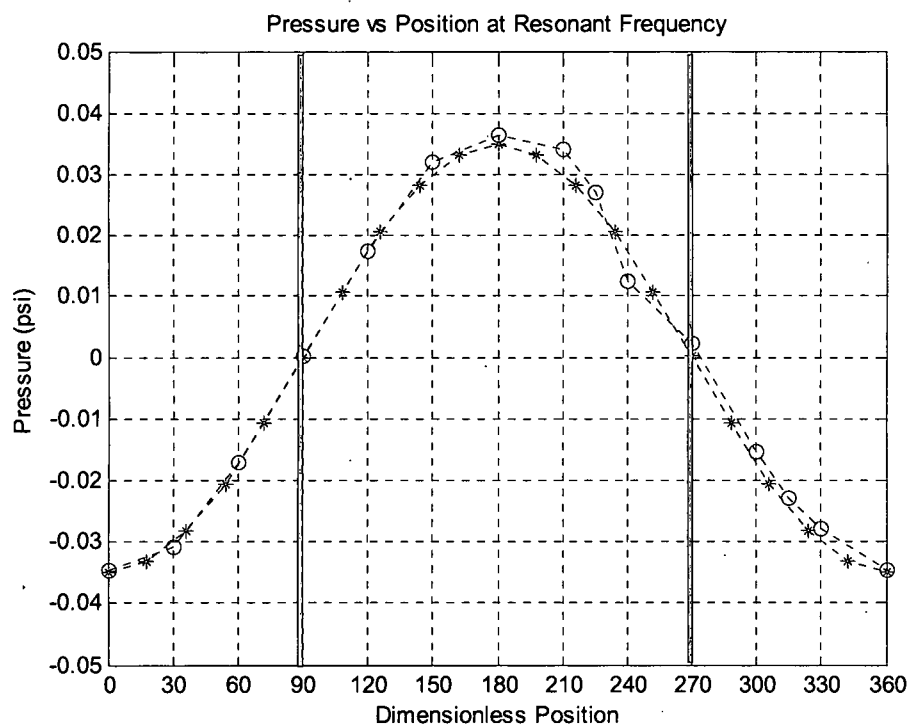
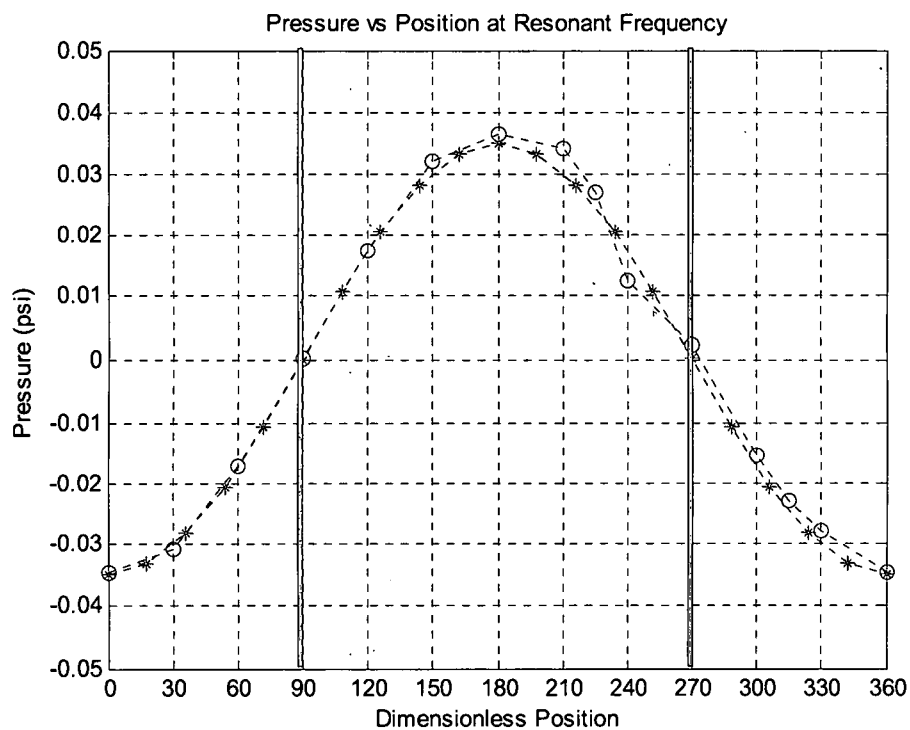


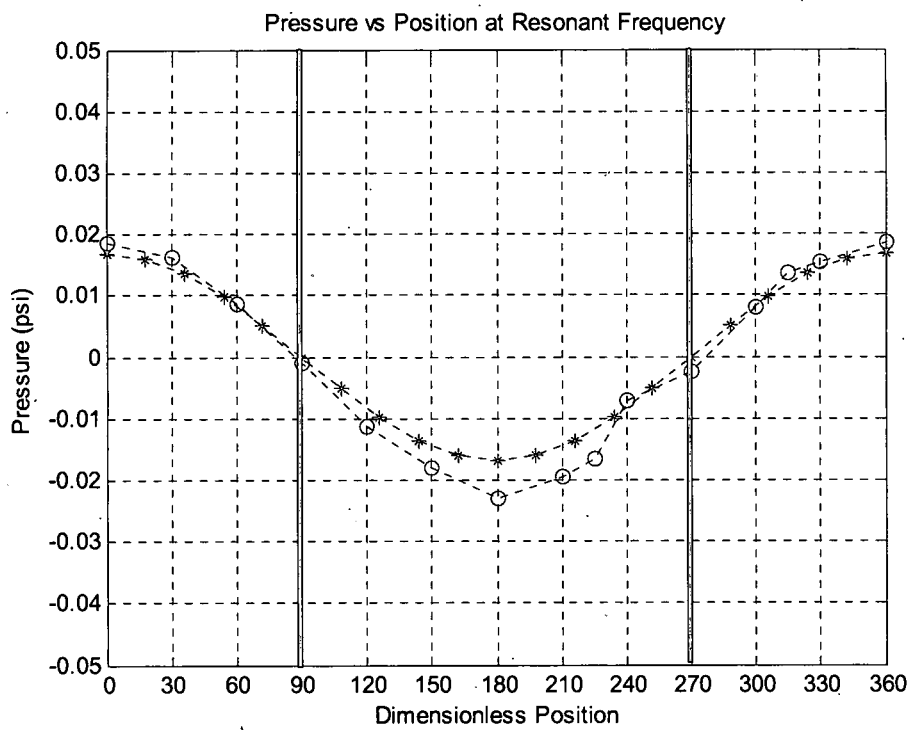
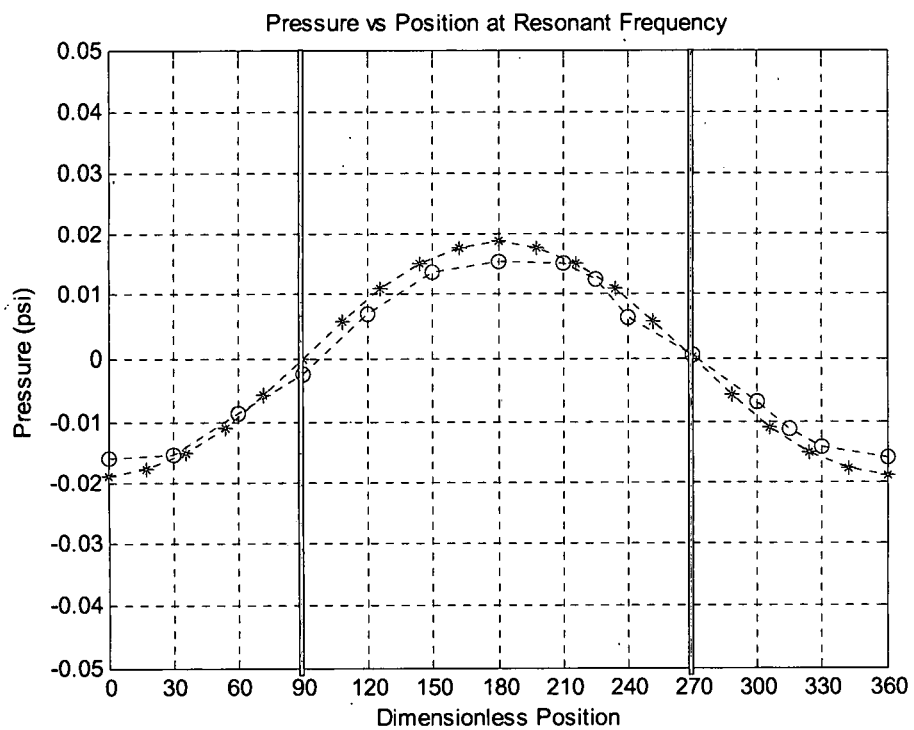




**Figure 7-38 Experimental Time Series of the Longitudinal Rig for the
Second Mode, Mach Number = 0.10**

Based on the longitudinal results, a circumferential experimental rig was designed and constructed. A shorter rig with a larger radius was modeled and constructed to test these new results on transverse, circumferential modes. A finite element model of the circumferential rig was also constructed and analyzed. Figure 7-39 depicts the experimental results for excitation of the third mode (the first circumferential mode) of the experimental rig with no flow. The mode was excited experimentally at the resonant frequency of 1700 Hz. This frequency was obtained from Figure 7-8. Along the x axis of the plots in Figure 7-39 is the circumferential position of the Kulite pressure transducer in degrees. Positions 0 degrees and 360 degrees are the same 12 o'clock position. Plotted in red with "x" markers are the experimental results. Plotted in blue with the "o" marker is the analytical solution for no flow. The experimental and analytical solutions are nearly identical. Note that the nodes, the thick purple lines, occur at the same location as the node in the FRF mode shape data in Figure 7-21.





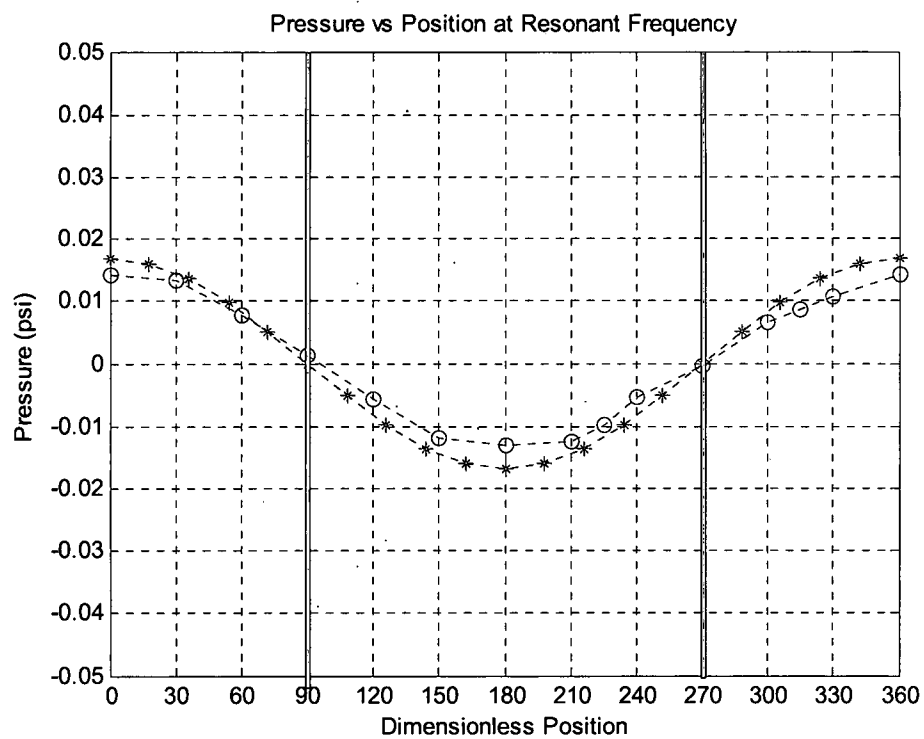
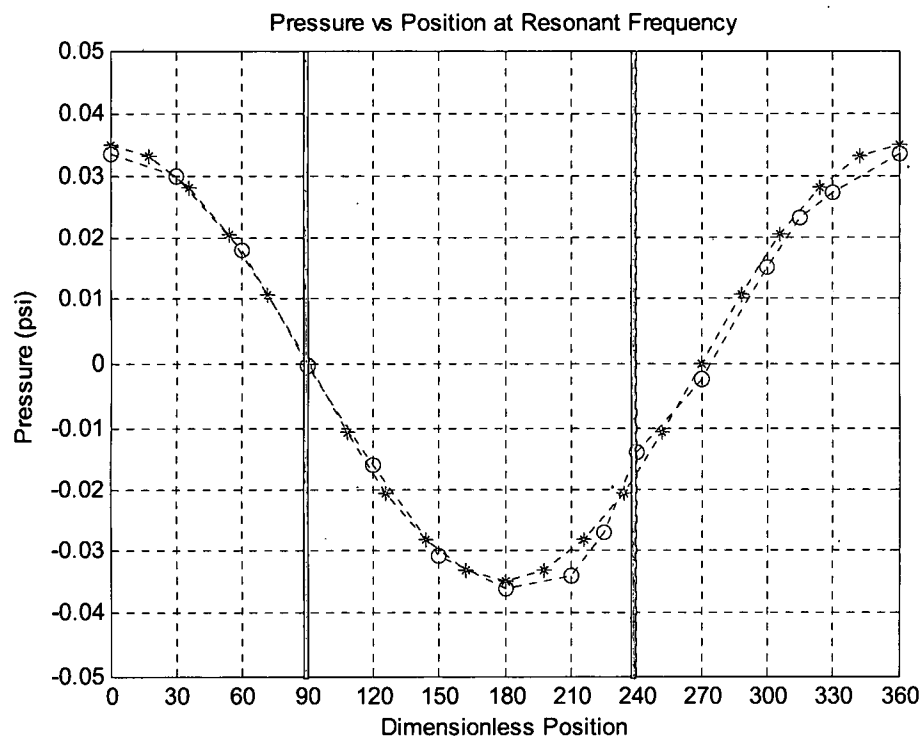
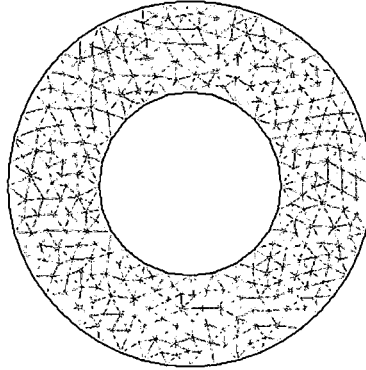


Figure 7-39 Experimental Time Series of the Circumferential Rig for the Fourth Mode With no Flow

Figure 7-40 the model representation of a slice through the circumferential rig at the axial location of the middle of the swirler. The model domain was grid with tetrahedrons. Equations 4-1, 4-2 and 4-3 were simulated in the two-



**Figure 7-40 Finite Element Model of the Circumferential Rig, Plane Slice
Through the Swirler**

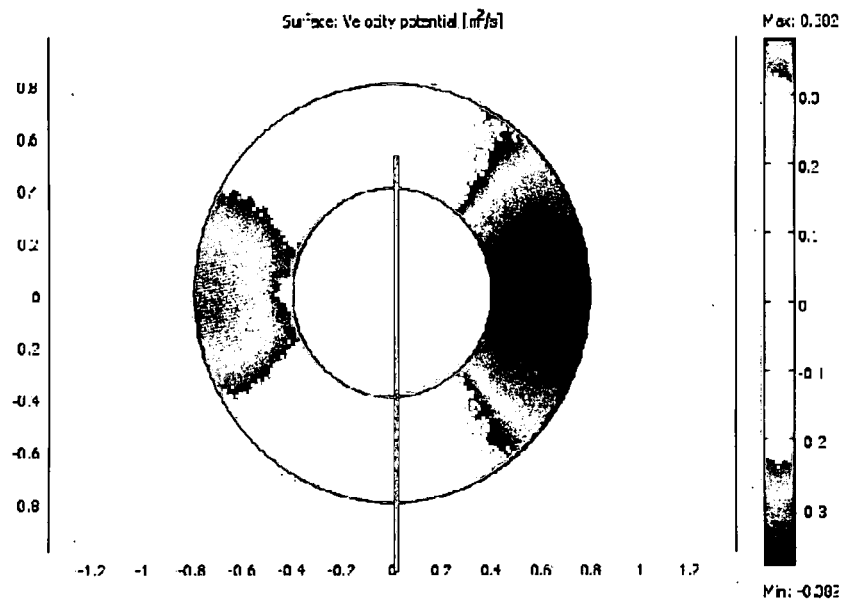
dimensional plane. A constant rotational velocity, V_{rot} was assumed. The rotational velocity was transformed into x and y coordinates by the transformation in Equations 7-9 and 7-10.

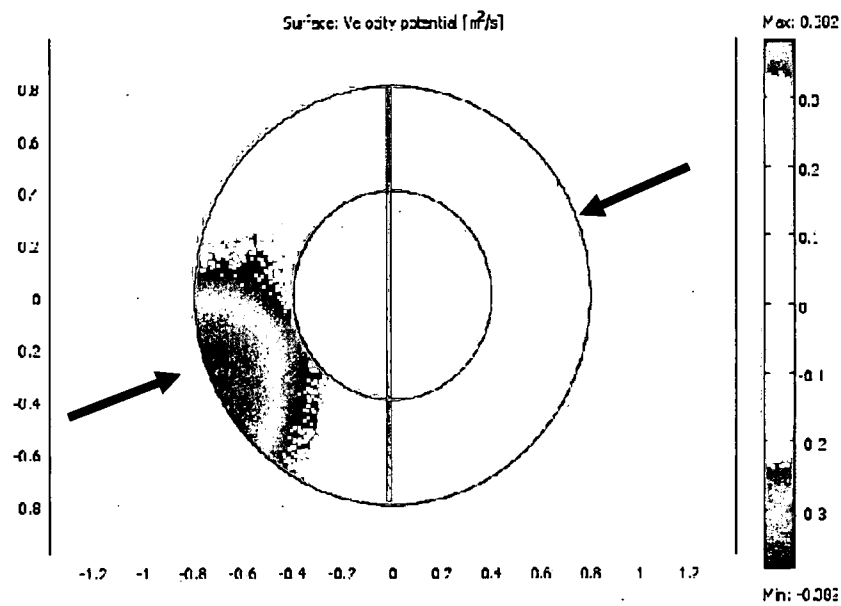
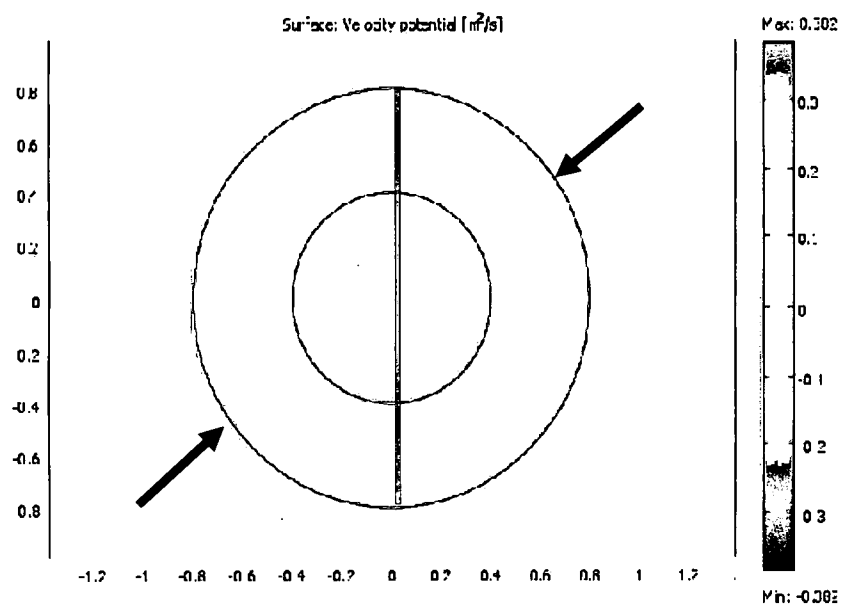
$$v_x = V_{rot} \frac{y}{\sqrt{x^2+y^2}} * \frac{\sqrt{x^2+y^2}}{R} = V_{rot} \frac{y}{R} \quad (7-9)$$

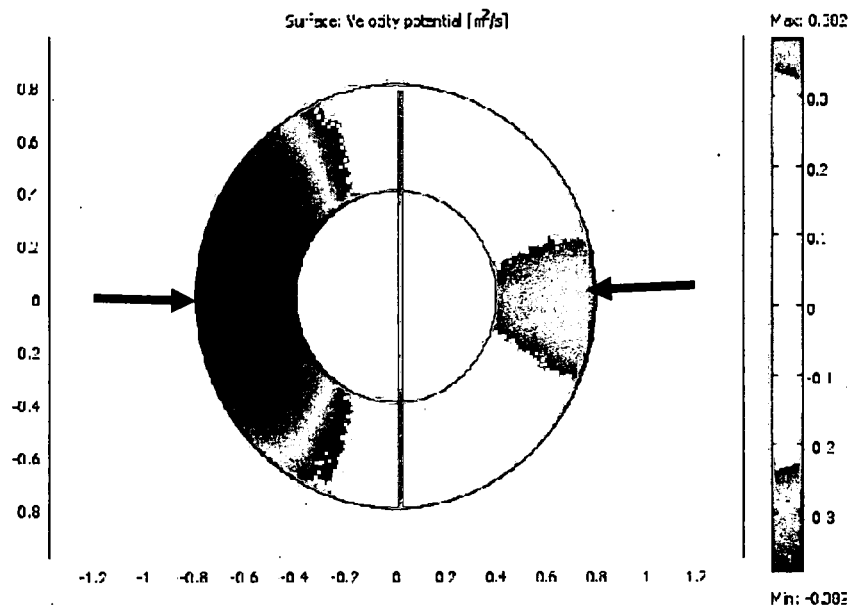
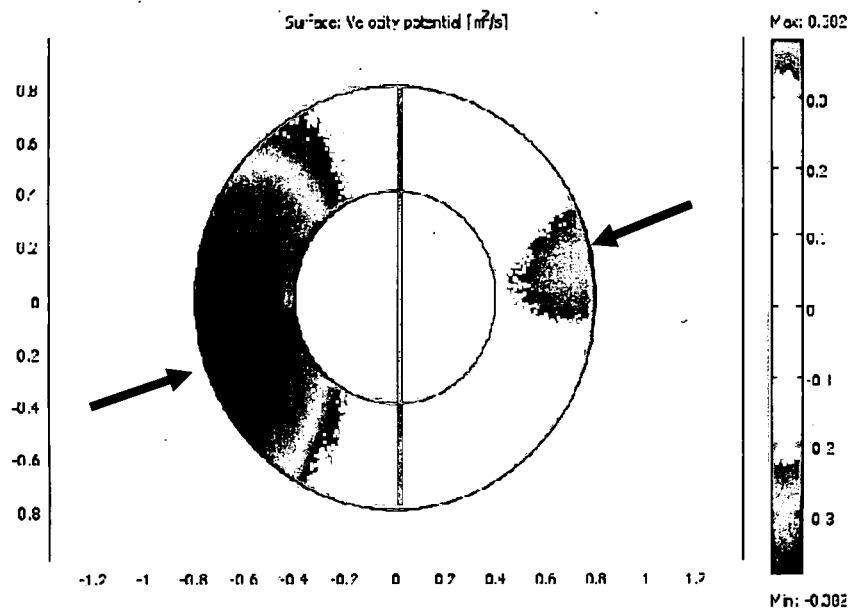
$$v_{xy} = V_{rot} \frac{x}{\sqrt{x^2+y^2}} * \frac{\sqrt{x^2+y^2}}{R} = V_{rot} \frac{x}{R} \quad (7-10)$$

The models were then solved in time domain using the transient analysis mode in COMSOL. Illustrated in Figure 7-41 are contours of pressure from the time domain solution of the finite element model for a blower mass flow of 0.054 kg/sec. Figure 7-41 depicts the model results of the effect of swirling flow on the 3rd (first circumferential) mode. Note in the second figure, the pressure increases

near the 1 o'clock position and decreases near the 7 o'clock position. As time increases, the location of the minimum, maximum and zero pressure rotates clockwise. At the last depicted instant in time, the maximum and minimum reach the 11 and 5 o'clock positions.







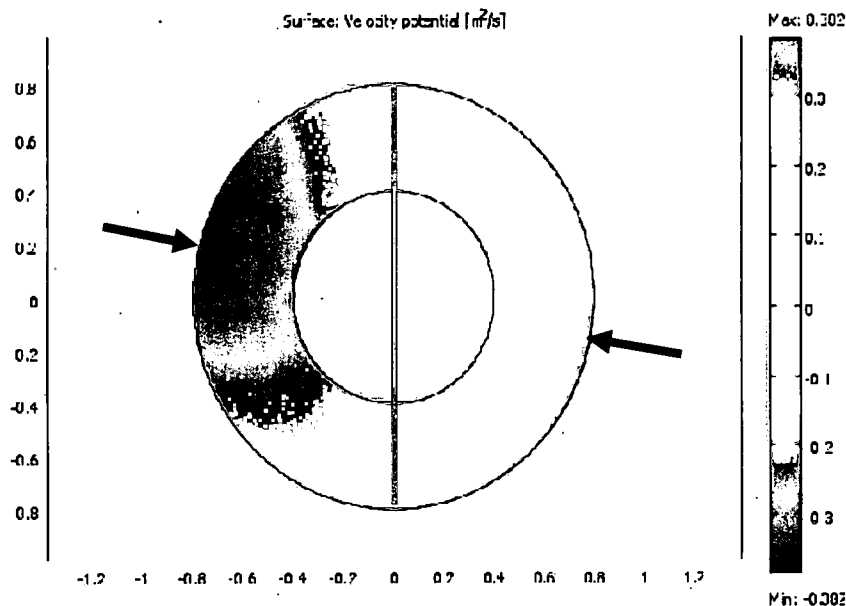
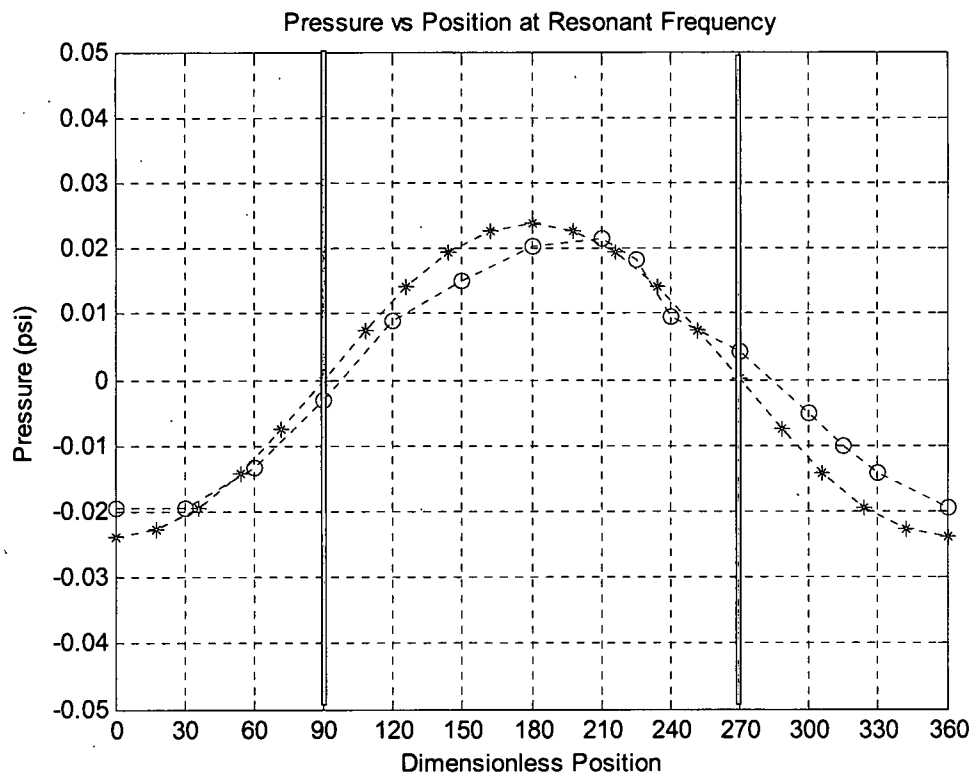
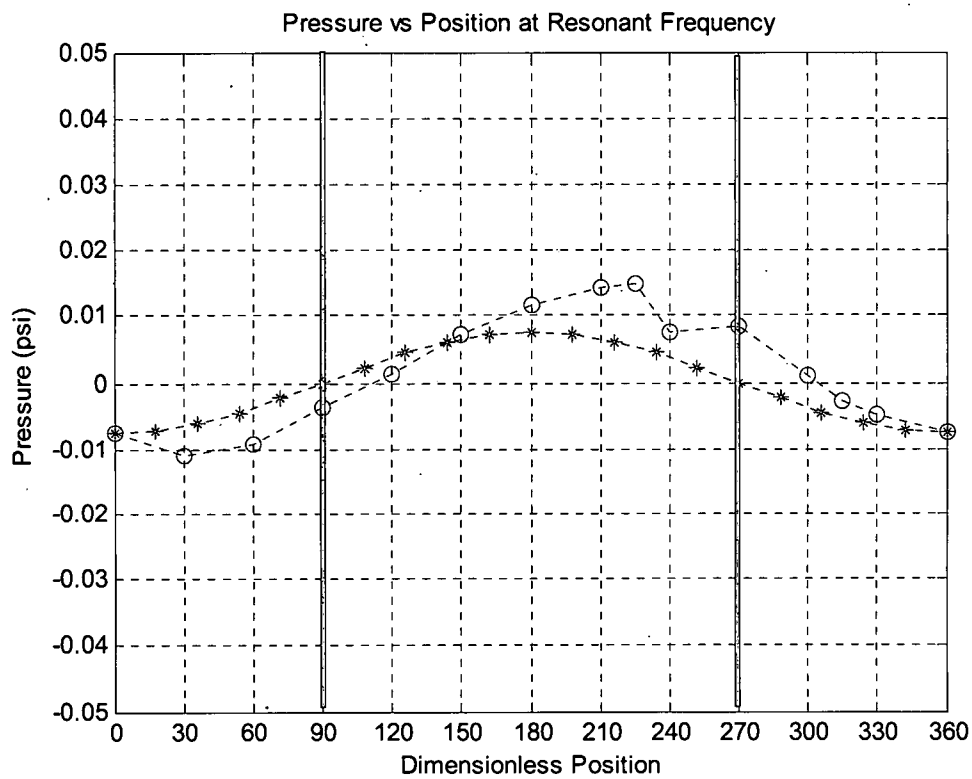
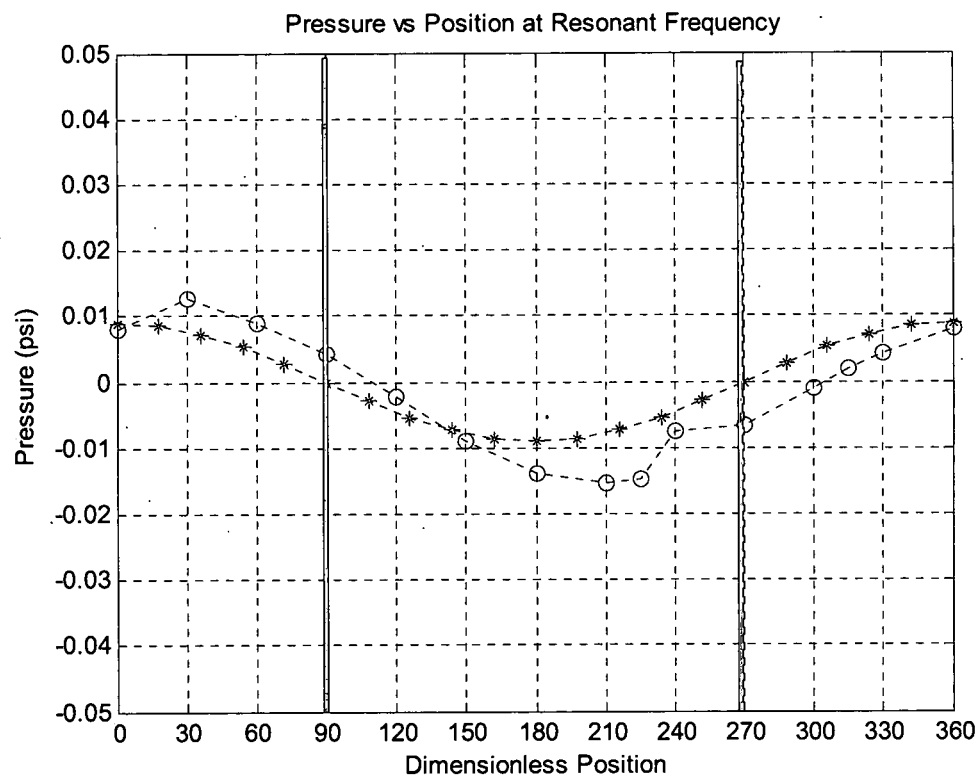
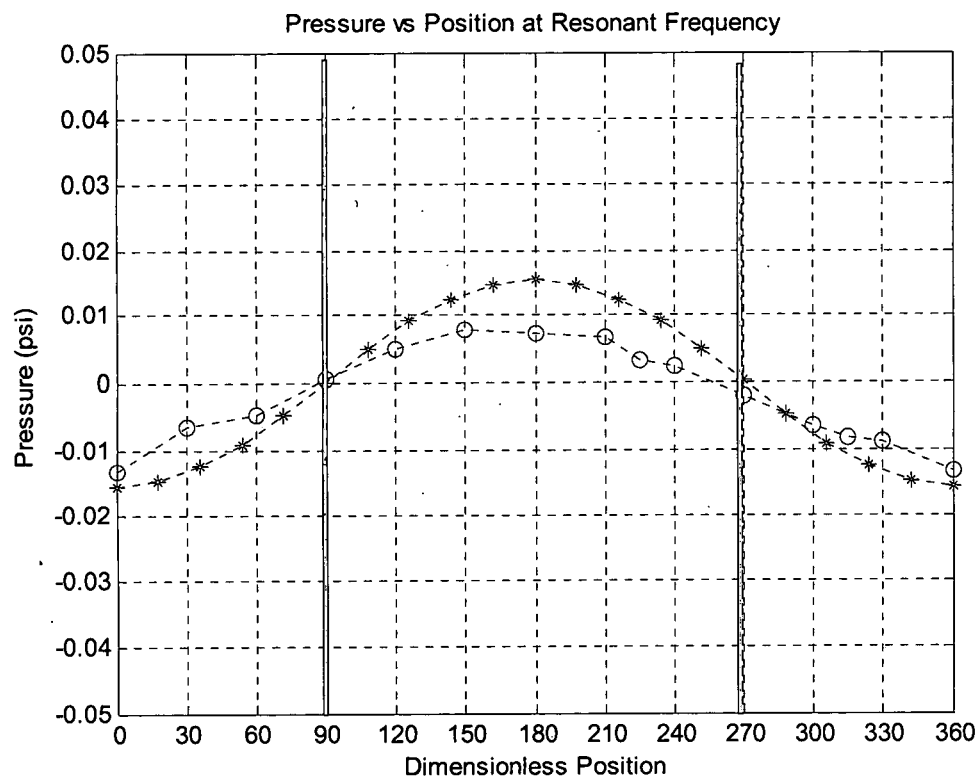


Figure 7-41 Numerical Time Series of the Circumferential Rig for the First Circumferential Mode (Mode 3), Mach Number = 0.10

Figures 7-42 and 7-43 are the results of the experimental time series for the circumferential experimental rig with flow. As detailed in Chapter 5, the circumferential experimental rig employed a swirler to spin the flow as it entered the experimental rig. The swirl velocity is proportional to the mass flow of the blower. In Figure 7-42 the blower mass flow was 0.054 kg/sec. The circumferential rig was excited at 1700 Hz, the resonant frequency for the third mode from Figure 7-9. In Figure 7-43 the blower mass flow was 0.090 kg/sec. For this flow rate the rig was excited at 1696 Hz, the resonant frequency for





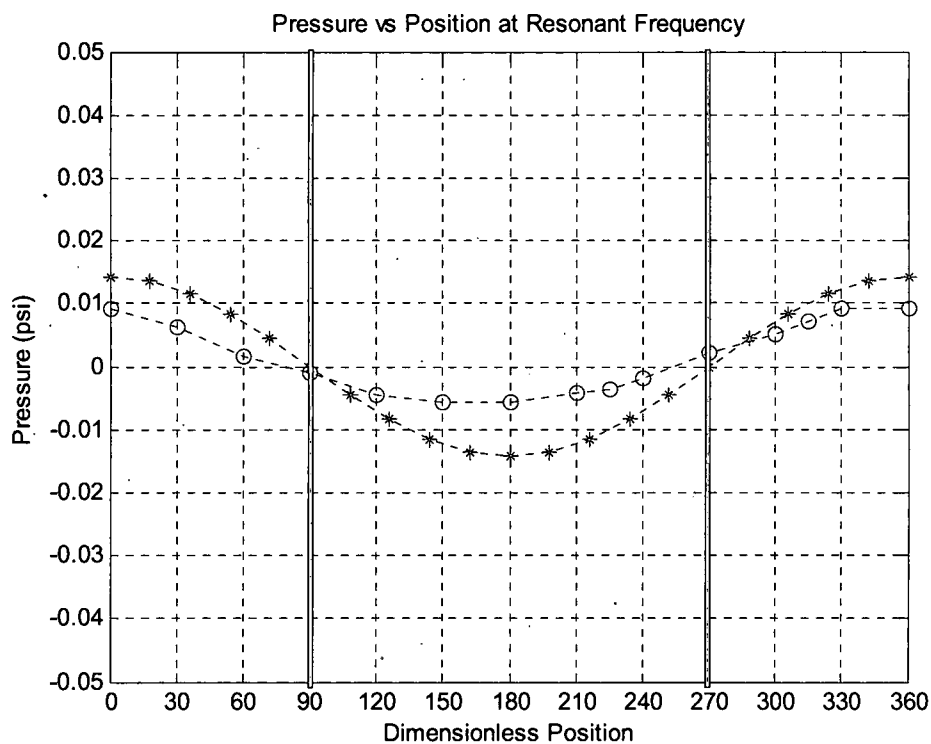
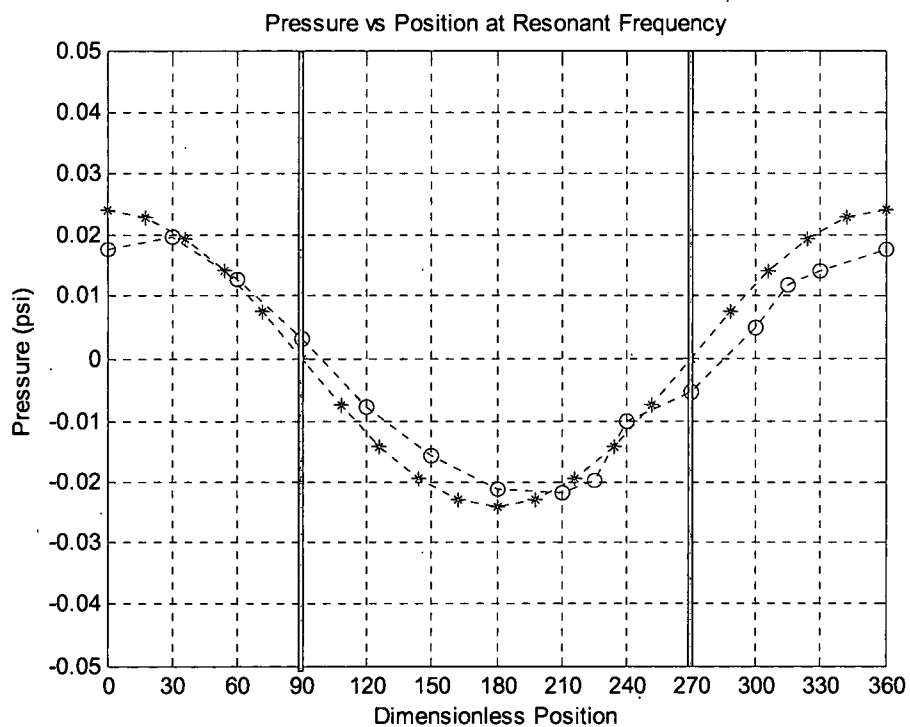
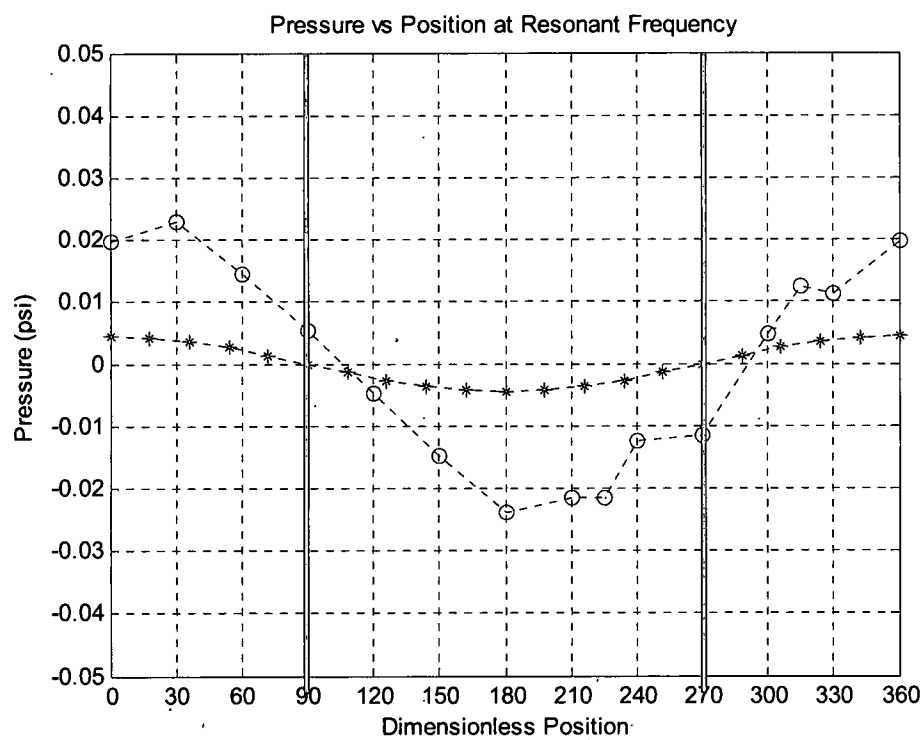
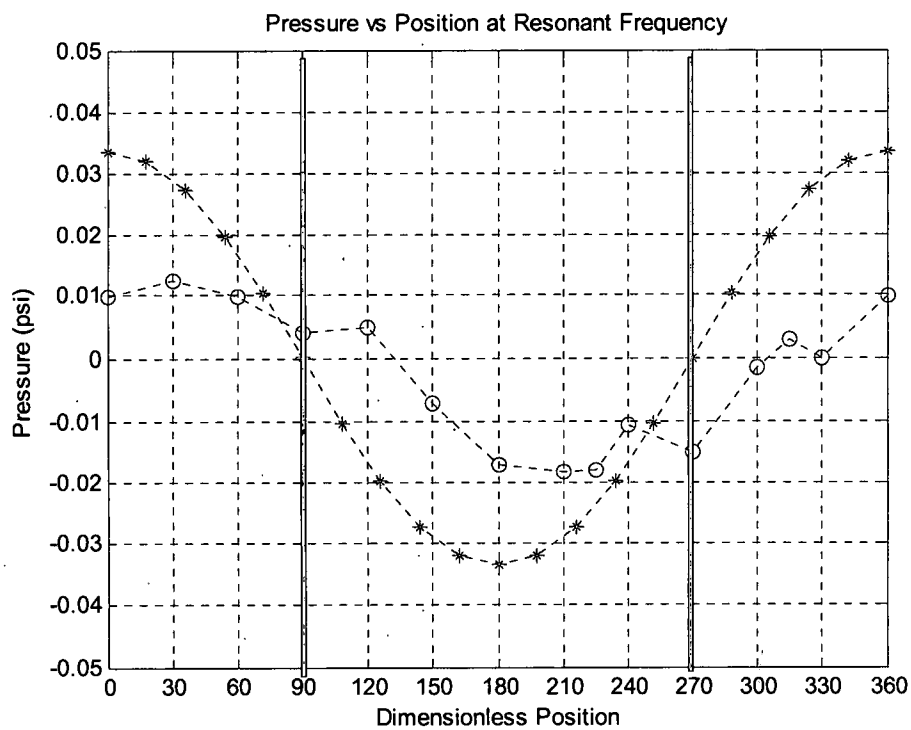
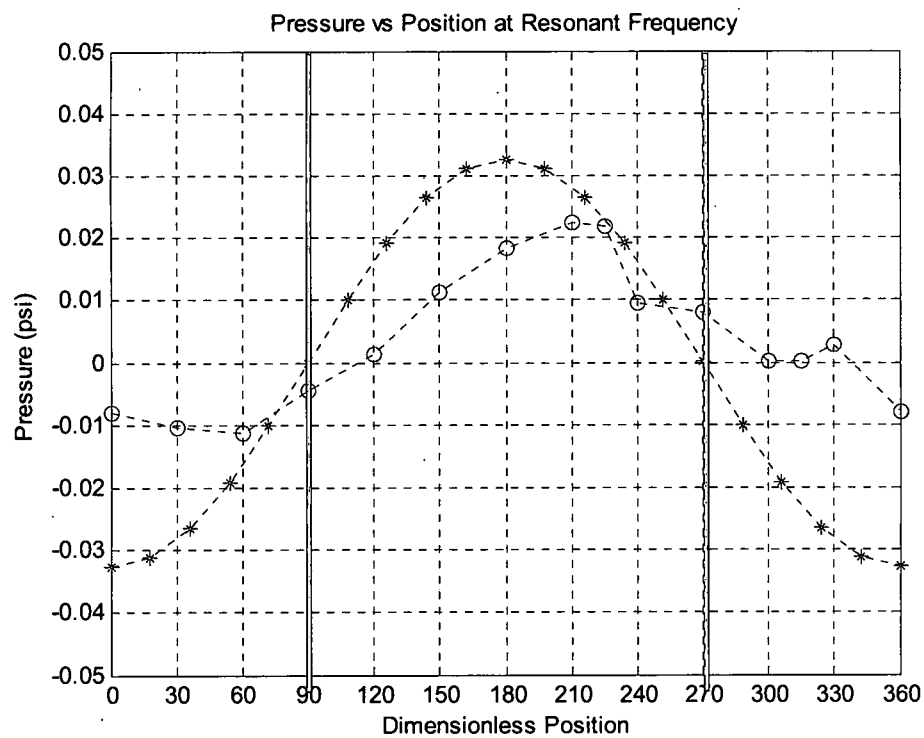
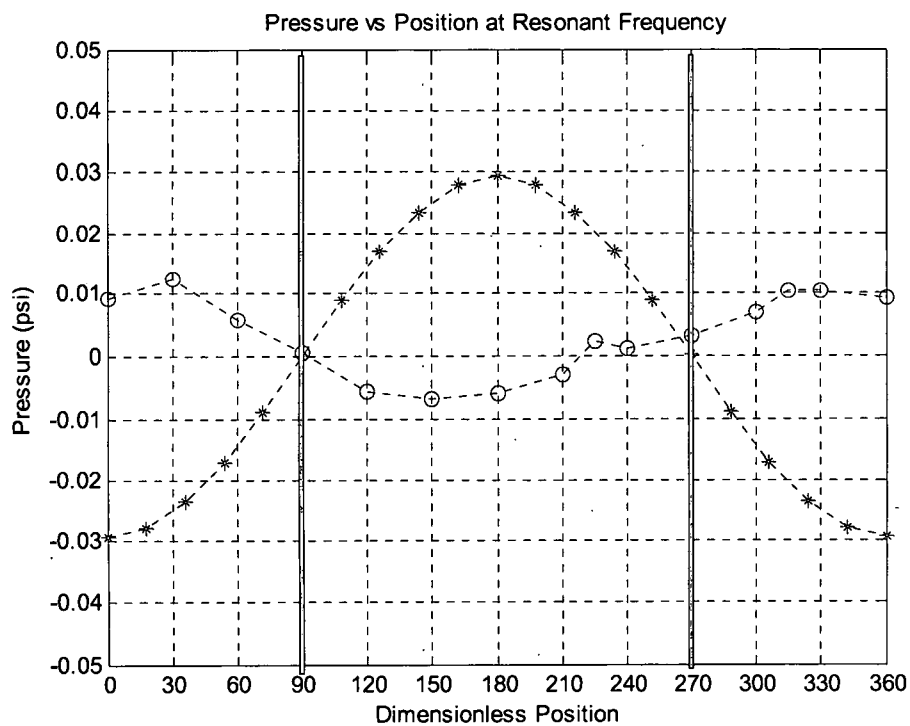


Figure 7-42 Experimental Time Series of the Circumferential Rig for the First Circumferential Mode (Mode 4), Blower Mass Flow of 0.054 kg/s





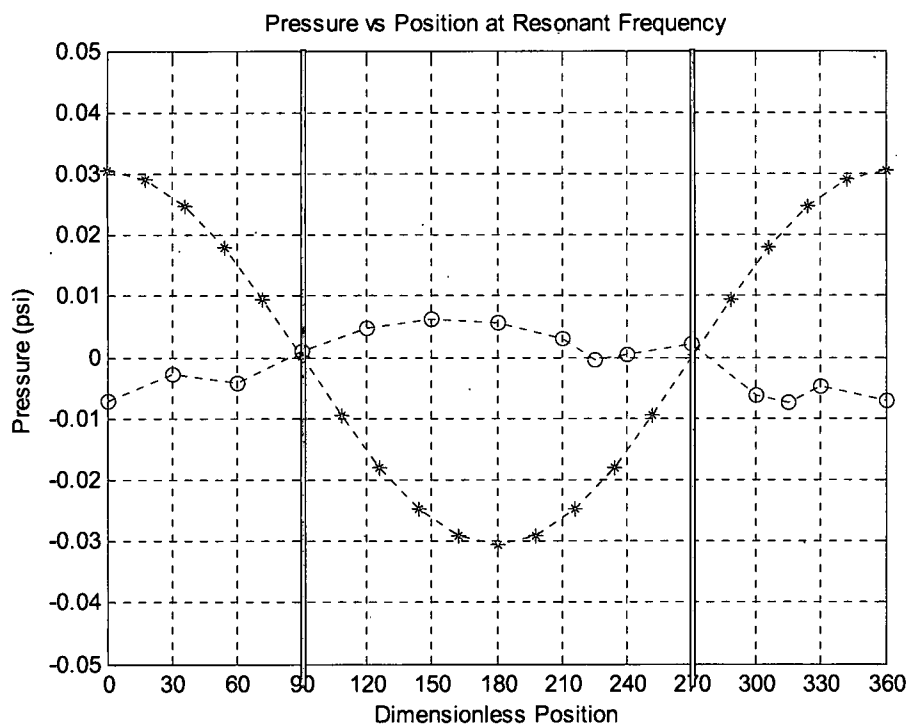
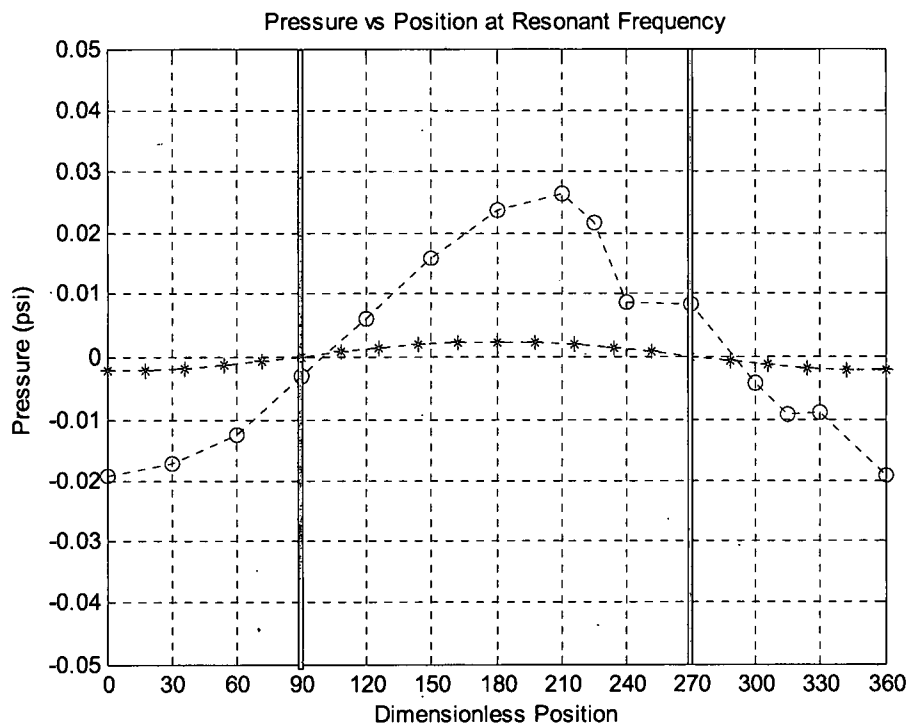


FIGURE 7-43 EXPERIMENTAL TIME SERIES OF THE CIRCUMFERENTIAL RIG FOR THE FIRST CIRCUMFERENTIAL MODE (MODE 4), BLOWER MASS FLOW OF 0.090 KG/S

the third mode from Figure 7-10. Depicted on the x axis of Figures 7-42 and 7-43 is the circumferential location of the Kulite transducers. The position on the x axis represents increasing clockwise location in degrees.

In Figures 7-42 and 7-43 the red with "+" marker is the analytical solution for no flow and the blue with the "o" marker is the analytical solution for no flow. In Figure 7-42 the maximum pressure is located at approximately 210 degrees, while the minimum pressure is located at 30 degrees for the same instant in time. As time increases the maximum pressure and minimums pressure move to the left on the x axis, decreasing position in degrees. This motion is counterclockwise in the circumferential domain. The maximum pressure crosses the location of the node at 90 degrees and the minimum pressure crosses the location of the node at 270 degrees between the third and fourth frames. The maximum pressure and minimum pressure cross the nodes again between the sixth and seventh frames. In the seventh frame the cycle begins to repeat. In the time series for the higher flow rate depicted in Figure 7-43, the nature of the motion of the maximum pressure and minimum pressure follow a similar pattern and is more pronounced than the motion in Figure 7-42.

VIII. CONCLUSIONS AND RECOMMENDATIONS

Conclusions

Many conclusions can be made about the effect of convection and shear on wave propagation. From the FRF magnitude data for both the experiments and the finite element models;

- Longitudinal and circumferential modes are in the shape of standing waves when no flow is present. This results in stationary node and anti-node locations.
- It is clear that the flow effects wave propagation by three means; viscosity, convection, and shear. Each of these contributes to causes the mode shapes to appear to be damped. As a result both the magnitude of the FRF and the resonant frequency of the modes decrease when compared to the magnitude and resonant frequency of the modes when flow is not present. The locations of the nodes and anti-nodes, however, do not change as flow is increased.
- The resonant frequency for pure convection, $w_{\text{resonant}} = w_n(1-M^2)$, is never achieved for any level of flow. Instead the effects of shear, viscosity, and convection combine to determine the value of the resonant frequency for all levels of flow.

- Damping caused by turbulent shear is frequency dependant. The turbulence cascade data suggests that turbulent shear extracts more energy at lower frequencies. Thus more energy is unavailable to the mean flow and acoustics at lower frequencies than at the higher frequencies. As a result the damped varies in the same way as the extracted turbulent energy.
- For the higher longitudinal mode numbers (third, fourth, and fifth), as the damping from the turbulent shear increases the resonant frequency increases, not decreases.
- The agreement between the model data for the center transducer, Figure 7-1, and the experimental data, Figure 7-21 are compelling. In both cases, the magnitude of the FRF increased at the resonant frequency of the second and fourth modes as the Mach number increases. For acoustic modes the center of the rig is a node for the second and fourth modes.

From the time series data, both experimental and modeled;

- The increase in the FRF magnitude at the center location, for the second and fourth modes (Figure 7-15, and 7-17) can be explained by examining the time response data. In the time response the anti-nodes are no longer anchored at the center for the second and forth modes. The movement of the anti-node(s) results in higher magnitude at the nodes on average.

- When flow is present, the location of minimum, maximum and zero pressure move as time increases. This is true even for flow Mach numbers < 0.10 .
- The moving minimum, maximum, and zero pressure change with a period of one divided by the resonant frequency of the excited mode.
- From the time series of the finite element models for both longitudinal and circumferential waves, the two convective terms:

$$2M(y)a \frac{\partial^2 p'}{\partial x \partial t}$$

$$M(y)^2 \frac{\partial^2 p'}{\partial x^2}$$

- is the only contributing factor for the movement of the minimum, maximum, and zero pressure locations with time. The analytical solutions also verify this conclusion.
- According to the analytical solutions, only convection affects the spatial portions of the solution, changing the effective wave number of the right and left propagating waves. This effect causes the minimum, maximum, and zero pressure points to move with time.
- The movement of the minimum, maximum, zero pressure locations due to convection is the reason for spinning modes in the circumferential domain reported in the Introduction Chapter.

Recommendations

The most important conclusion from this research is that flow greatly effects the propagation of longitudinal and transverse pressure waves. The effect of flow (shear, viscosity, and convection) is to damp the wave propagation. The flow (convection) also causes the minimum, maximum, and zero pressure locations to move in time, even at very low flow rates. As a result using the acoustic wave equation to model wave propagation in propulsion systems is ill advised. Instead the models must contain as a minimum the convective and shear terms as in Equation 2-18:

$$\begin{aligned} \frac{\partial^2 p'}{\partial t^2} + 2M(y)a \frac{\partial^2 p'}{\partial x \partial t} - a^2 [1 - M(y)^2] \frac{\partial^2 p'}{\partial x^2} \\ - a^2 \frac{\partial^2 p'}{\partial y^2} - 2\bar{\rho}a^3 \frac{\partial v'}{\partial x} \frac{\partial M(y)}{\partial y} = 0 \end{aligned} \quad (2-18)$$

Without these terms neither damping nor the motion of the anti-node(s) associated with spinning waves in circumferential rigs will not be resolved.

BIBLIOGRAPHY

Anderson, W., Ryan, H., and Santoro, R., 1995, "Combustion Instability Mechanisms in Liquid Rocket Engines Using Impinging Jet Injectors", AIAA 95-2357.

Boucheron, R., Bailliet, J., and Valiere, C., 2005, "Analytical Solution of Multimodal Acoustic Propagation in Circular Ducts with Laminar Mean Flow Profile", Journal of Sound and Vibration, Article in Press

Bibik, O., Lubarsky, E., Shcherbik, D., Hadjipanayis, M., and Zinn, B., 2008, "Rotational Traveling of Tangential Wave in LRE Combustor Simulator (0 KB) " AIAA-2008-1001, The 46th AIAA Aerospace Sciences Meeting and Exhibit, Reno, Nevada

Candel, S., 2002, "", Proceeding of the Combustion Institute, 29, 1-28.

Cantrell, R., et al., 1963, "Acoustic Damping in Cavities with Mean Velocity and Thermal Boundary Layers", Journal of the Acoustic Society of America, 35, 4, 500-509.

Denemeyer, R., (1968), Introduction to Partial Differential Equations and Boundary Value Problems, McGraw Hill.

Dowling, A.P., 1995, "The Generation of Thermoacoustic Oscillations", Journal of Sound and Vibration, 180(4), 557-581

Dowling, A.P. and Stow, S.R., 2003, "Acoustic Analysis of Gas Turbine Combustors", Journal of Propulsion and Power, 19(5), 751-764.

Dukomaci, E., 1995, "Sound Transmission in Narrow Pipes with a Superimposed Uniform Mean Flow and Acoustic Modeling for Automobile Catalytic Converters", Journal of Sound and Vibration, 182, 799-808.

Dukomaci, E., 1998, "The Transmission of Sound in Circular and Rectangular Pipes with Superimposed Mean Flow", Journal of Sound and Vibration, 210, 3, 375-389.

Dukomaci, E., 2002, "On the Propagation of Plane Sound Waves in Ducts Carrying an incompressible Axial Flow Having an Arbitrary Velocity Profile", Journal of Sound and Vibration, 249, 4, 824-827.

Eversman, W., 1970, "The Effect of Mach Number on the Tuning of an Acoustic Lining in a Flow Duct Lining", *Journal of the Acoustic Society of America*, 48, 2, 425-428.

Eversman, W., 1971a, "The Effect of on the transmission and Attenuation of Sound in an Acoustically treated Circular Duct", *Journal of the Acoustic Society of America*, 49, 5, 1372-1380.

Eversman, W., 1971b, "Signal Velocity in a Duct with Flow", *Journal of the Acoustic Society of America*, 50, 2, 421-425.

Hersh, a., and Catton, I., 1971, "Effects of Shear on Sound Propagation in Rectangular Ducts", *Journal of the Acoustical Society of America*, 5, 3, 992-1003.
Ghoniem, A., 1999, *Fundamentals and Modeling in Combustion*, 2. 280.

Gogate, G, and Munjal, M, 1992, "Analytical Solution of the Laminar Mean Flow Wave Equation in a Lined or Unlined Two-dimensional Rectangular Duct", *Journal of the Acoustical Society of America*, 92:5, 2915-2923.

Grenda, J., Venkateswaran, S., and Merkle, C., 1993, "Three-Dimensional Analysis of Combustion Rocket Instabilities in Liquid Rockets", AIAA-93-0235.

Hinze J.O., 1987, Turbulence, The McGraw Hill Company, New York.

Howe, M. S., 2003, *Theory of Vortex Sound*, Cambridge University Press, 1-3, 114-116.

Incorporera, F., and De Witt, D., 1985, Fundamentals of Heat and Mass Transfer, John Wiley and Sons, New York.

Ingard, U., and Singhal, V., 1973, "Upstream and Downstream Sound Radiation into a Moving Fluid", *Journal of the Acoustic Society of America*, Vol.54, No. 5, pp. 1343-1346.

Ingard, U., and Singhal, V., 1974, "Sound Attenuation in Turbulent Pipe Flow", *Journal of the Acoustic Society of America*, Vol.55, No. 3, pp. 535-538.

Ingard, U., and Singhal, V., 1975, "Effect of Flow on the Acoustic Resonances of an Open-ended Duct", *Journal of the Acoustic Society of America*, Vol.58, No. 4, pp. 788-793.

Karthik, B., Mohanraj, R., Ramakrishnan, R, and Sujith, R., 1999, "Exact Solution for Sound Propagation in Ducts with an Axial Mean Temperature Gradient and Particulate Damping", *Journal of the Acoustic Society of America*, 106, 2391-2395.

Karthik, B., Manoj Kumar, B., and Sujith, R., 2000, "Exact Solution to One-Dimensional Acoustic Fields with Temperature Gradient and Mean Flow", Journal of the Acoustic Society of America, 108, 38-43.

Kim, J. ., and Lee, D. J., 1998, "General Formulation and Application of Characteristic Boundary Conditions", AIAA/CEAS-98-2222.

Kolmogorov, A. N., 1941, "Dissipation of energy in locally isentropic turbulence", Proceedings of the USSR Academy of Science, 32, 16-18.

Kolmogorov, A. N., (1941), "The local structure of turbulence in incompressible fluid for very large Reynolds numbers", Proceedings of the USSR Academy of Science, 30, 299-303.

Kumar, B., and Sujith, R., 1998, "Exact Solution for One-dimensional Acoustic Fields in Ducts with Polynomial Mean Temperature Profiles", ASME Journal of Vibr. Acoustics, 120, 965-969.

Lovett, J., Chu, W., and Shah, S., (1999), Modeling of Combustion Chamber Acoustics and Control of Combustion Instabilities in Gas Turbines", 6th International Congress on Sound and Vibration, July 1999.

Lovett, J., Brogan, T., Philippona, D., Kiel, B., and Thompson, T. (2004), "Development Needs for Advanced Afterburner Design", AIAA 2004-1492.

Lubarsky, E., Shcherbik, D., Bibik, o., Zinn, B., and Hadjipanayis, m., 2008, "Control of Tangential Combustion Instability by Asymmetric Baffle" AIAA-2008-955, The 46th AIAA Aerospace Sciences Meeting and Exhibit, Reno, Nevada

Morse and Ingard, 1968, Theoretical Acoustics McGraw Hill, NY

Mungar, p., and Plumblee, H., 1969, "Propagation and Attenuation of Sound in a Soft-Walled Annular Duct Containing a Shear Flow", NASA SP-207, 305-327.

Mungar, p., and Gladwell, G., 1969, "Acoustic Wave Propagation in a Sheared Fluid Contained in a Duct", JSV, 9, 1, 28-48

Nallasamy, M., Sutliff, D., and Heidelberg, L., 2000, "Propagation of Spinning Acoustic Modes in Turbofan Exhaust Ducts", Journal of Propulsion and Power, Vol . 16, No. 5, pgs. 736-743.

Peat, K., and Kirby, R., 1999, "Acoustic Wave Propagation Along a Narrow Cylindrical Duct in the Presence of an Axial Mean Flow and Temperature Gradient", Journal of Sound and Vibration, 107, 4, 1859-1867.

Polifke, W. et al., 2006, "Partially Reflecting and Non-reflecting Boundary Conditions for the Simulation of Compressible Viscous Flows", Journal of Computational Physics, 214, 437-449.

Poinsot, T., Le Chatelier, C., Candel S. M., and Esposito, E., (1986), "Experimental Determination of the Reflection Coefficient of a Premixed Flame in a Duct", Journal of Sound and Vibration, vol. 107, no. 2, pps 265-278.

Pridmore-Brown, D., 1958, "Sound Propagation in a Fluid Through an Attenuating Duct", Journal of Fluid Mechanics, 4, 393-406.

Rayleigh, J. W. S., 1878, "The Explanation of Certain Acoustic Phenomena", Nature, 18:319-321

Rayleigh, J.W.S., 1945, Theory of Sound, Vol. II, Dover Publications, New York, pp. 223-234

Rice, E., 1969, "Propagation of Waves in an Acoustically Lined Duct with a Mean Flow", NASA SP-207,345-355.

Richardson, E. G., 1949, Sound, 2nd Edition, Edward Arnold and CO, London, p161-164.

Schauer, J, et al., 1978, "Sound Transmission Through Ducts", AFAPL-TR-78-25

Subrahmanyam, P., Sujith, R., and Lieuwen, T., 2003, "propagation of Sound in Inhomogeneous Media: Exact, Transient Solutions in Curvilinear Geometries", Journal of Vibration and Acoustics, 125, 133-136

Sujith, R., Waldherr, G., and Zinn, B., 1995, "An Exact Solution for One-Dimensional Acoustic Fields in Ducts with an Axial Temperature Gradient", Journal of Sound and Vibration, 184, 389-402.

Tam, C., 1971, "Transmission of Spinning Acoustic Modes in a slightly Non-Uniform Circular Duct", Journal of Sound and Vibration, Vol. 18, No. 3, pp. 339-351.

Tennekes, H., and Lumley, J., 1990, A First Course in Turbulence, MIT Press.

Tyler, J., and Sofrin, T., 1962, "Axial Flow Compressor Noise", SAE Transactions, Vol. 70, pp. 309-332.

Weinberg, H., (1965), A First Course in Partial Differential Equations with Complex Variables and Transform Methods, Diver Publications Inc, New York, NY.

White, F., 1986, Fluid Mechanics, Second Edition, McGraw-Hill, New York.
Xu, J., and Ko, S., 1990, "Computer Simulation of Film Cooling with Coolants from One and Two Rows of Holes", ASME Paper 90-WA/HT-7.

Wood, A. B., 1957, A Textbook of Sound, 3rd Edition, Neill and Co. LTD, London, p179-182.

Zaho, Y., and Morris, P., 2005, "The prediction of Fan Exhaust Noise Propagation", AIAA 2005-2815.

Zhang, X., Chen, X., Morfey, C., and Nelson, P., 2004, "Computation of Spinning Modal Radiation from an Unflanged Duct", AIAA Journal, Vol. 42, No, 9, pgs 1795-1801.

Zinn. B., and Lores, M., 1972, "Application of the Galerikin Method in the Solution of Non-linear Axial Combustion Instability Problems in Liquid Rockets", Combustion Science Technology, 4, 269-278.

APPENDICES

Appendix 1. Conservation of Mass

Mass conservation is expressed in differential conservative law form by:

$$\frac{\partial}{\partial t} \rho + \frac{\partial(\rho u_i)}{\partial x_i} = 0 \quad (\text{A1-1})$$

The two-dimensional continuity equation is represented by the PDE:

$$\frac{\partial \rho}{\partial t} + \frac{\partial(\rho u)}{\partial x} + \frac{\partial(\rho v)}{\partial y} = 0 \quad (\text{A1-2})$$

Applying the chain rule to the flux term results in:

$$\frac{\partial \rho}{\partial t} + \rho \frac{\partial u}{\partial x} + u \frac{\partial \rho}{\partial x} + \rho \frac{\partial v}{\partial y} + v \frac{\partial \rho}{\partial y} = 0 \quad (\text{A1-3})$$

Appendix 2. Conservation of Momentum

Momentum conservation in differential conservative law form is expressed as:

$$\frac{\partial(\rho u_i)}{\partial t} + \frac{\partial(\rho u_j u_i)}{\partial x_j} = \rho F_i - \frac{\partial p}{\partial x_i} + \frac{\partial \tau_{ij}}{\partial x_j} \quad (\text{A2-1})$$

Assuming no body forces and inviscid flow, Equation A2-1 reduces to:

$$\frac{\partial(\rho u_i)}{\partial t} + \frac{\partial(\rho u_j u_i)}{\partial x_j} = -\frac{\partial p}{\partial x_i} \quad (\text{A2-2})$$

In x spatial dimension Equation A2-2 reduces to:

$$\frac{\partial(\rho u)}{\partial t} + \frac{\partial(\rho u u)}{\partial x} + \frac{\partial(\rho u v)}{\partial y} = -\frac{\partial p}{\partial x} + \nu f_1(u, v) \quad (\text{A2-3})$$

Applying the chain rule to both derivatives on the left hand side of the equation

$$\rho \frac{\partial u}{\partial t} + u \frac{\partial \rho}{\partial t} + \rho u \frac{\partial u}{\partial x} + u \frac{\partial(\rho u)}{\partial x} + \rho v \frac{\partial u}{\partial y} + u \frac{\partial(\rho v)}{\partial y} = -\frac{\partial p}{\partial x} + \nu f_1(u, v)$$

$$\rho \frac{\partial u}{\partial t} + \rho u \frac{\partial u}{\partial x} + \rho v \frac{\partial u}{\partial y} + u \left[\frac{\partial \rho}{\partial t} + \frac{\partial(\rho u)}{\partial x} + \frac{\partial(\rho v)}{\partial y} \right] = -\frac{\partial p}{\partial x} + \nu f_1(u, v)$$

From continuity the bracketed term is zero resulting in:

$$\rho \frac{\partial u}{\partial t} + \rho u \frac{\partial u}{\partial x} + \rho v \frac{\partial u}{\partial y} = -\frac{\partial p}{\partial x} + \nu f_1(u, v) \quad (\text{A2-4})$$

In y spatial dimension Equation A2-2 reduces to:

$$\frac{\partial(\rho v)}{\partial t} + \frac{\partial(\rho v u)}{\partial x} + \frac{\partial(\rho v v)}{\partial y} = -\frac{\partial p}{\partial y} + \nu f_2(u, v) \quad (\text{A2-5})$$

Applying the chain rule to both derivatives on the left hand side of the equation

$$\rho \frac{\partial v}{\partial t} + v \frac{\partial \rho}{\partial t} + \rho u \frac{\partial v}{\partial x} + v \frac{\partial(\rho u)}{\partial x} + \rho v \frac{\partial v}{\partial y} + v \frac{\partial(\rho v)}{\partial y} = -\frac{\partial p}{\partial y} + \nu f_2(u, v)$$

$$\rho \frac{\partial v}{\partial t} + \rho u \frac{\partial v}{\partial x} + \rho v \frac{\partial v}{\partial y} + v \left[\frac{\partial \rho}{\partial t} + \frac{\partial(\rho u)}{\partial x} + \frac{\partial(\rho v)}{\partial y} \right] = -\frac{\partial p}{\partial y} + \nu f_2(u, v)$$

From continuity the bracketed term is zero resulting in:

$$\rho \frac{\partial v}{\partial t} + \rho u \frac{\partial v}{\partial x} + \rho v \frac{\partial v}{\partial y} = -\frac{\partial p}{\partial y} + \nu f_2(u, v) \quad (\text{A2-6})$$

Appendix 3. Separation of Variables Solution to the Acoustic Wave Equation

In this appendix solutions for the acoustic wave equation will be derived. Starting with Equation 2-19, the acoustic wave equation can be derived by assuming Mach number was zero. This results in the acoustic wave equation:

$$\frac{\partial^2 p}{\partial t^2} - a^2 \frac{\partial^2 p}{\partial x^2} = 0 \quad (\text{A3-1})$$

For the wave equation many mathematical and acoustics texts offer the solution of Equation A3-1 by applying separation of variables. It is assumed that the solution of the Equation A3-1 can be separated into time and spatial portions by:

$$p(x,t) = X(x)T(t) \quad (\text{A3-3})$$

Substituting this solution back into Equation A3-1 yields:

$$X(x) \frac{\partial^2 T(t)}{\partial t^2} - a^2 T(t) \frac{\partial^2 X(x)}{\partial x^2} = 0 \quad (\text{A3-4})$$

Separating the variables of Equation A3-4 yields

$$-\frac{\frac{\partial^2 T(t)}{\partial t^2}}{a^2 T(t)} = -\frac{\frac{\partial^2 X(x)}{\partial x^2}}{X(x)} = \beta^2 \quad (\text{A3-5})$$

where β is a constant. Equation A3-5 can then be separated into two ODEs:

$$\frac{\partial^2 T(t)}{\partial t^2} + \beta^2 a^2 T(t) = 0$$

$$\frac{\partial^2 X(x)}{\partial x^2} + \beta^2 X(x) = 0$$

(A3-6 & A3-7)

The solutions of these two ODE's are respectively:

$$T(t) = A \cos(\beta a t) + B \sin(\beta a t) \quad (\text{A3-8})$$

$$X(x) = C \cos(\beta x) + D \sin(\beta x) \quad (\text{A3-9})$$

For an open-open system there is a node at the inlet and exit at all instances in time. Applying the boundary conditions for a for an open-open system to Equations A3-9;

$$0 = X(0) = C$$

$$0 = X(L) = D$$

Beta must be selected such that Equation A3-9 is non-trivial, thus:

$$\beta = \pm \frac{n\pi}{L} = k_n$$

and

$$\omega_n = \beta a = \pm \frac{n\pi a}{L}$$

Above ω_n is termed the "nth natural frequency" of the system. Equation A3-9 becomes:

$$X_n(x) = \sin(k_n x)$$

or

$$X_n(x) = \sin(-k_n x)$$

(A3-10)

The nth solution for T(t) is

$$T_n(t) = A_n \cos(\pm \omega_n t) + B_n \sin(\pm \omega_n t) \quad (\text{A3-11})$$

Substituting Equations A3-10 and A3-11 into Equation A3-3, the nth solution to the wave Equation is:

$$p_n(x, t) = \sin(\pm k_n x) [A_n \cos(\pm \omega_n t) + B_n \sin(\pm \omega_n t)] \quad (\text{A3-12})$$

Equation A3-12 represents the n normal modes that satisfy the wave equation.

The sum of the n solutions is the exact solution to the homogenous wave equation over a finite interval.

Appendix 4. Derivation of the Solutions for the Damped Wave Equation

In this appendix solutions for the damped acoustic wave equation will be derived. The damped acoustic wave equation can be derived by assuming Mach number is zero resulting in Equation 2-29.

$$\frac{\partial^2 p}{\partial t^2} + R_2 \frac{\partial p'}{\partial t} - a^2 \frac{\partial^2 p}{\partial x^2} = 0 \quad (\text{A4-1})$$

Solutions to equation A4-1 are also found by applying separation of variables.

The first step in finding the solution is to make the assumption that the solution is of the form:

$$p(x, t) = e^{-R_2 t} v(x, t) \quad (\text{A4-2})$$

Substituting into Equation A4-1 yields:

$$\frac{\partial^2 v(x, t)}{\partial t^2} - R_2^2 v(x, t) - a^2 \frac{\partial^2 v(x, t)}{\partial x^2} = 0 \quad (\text{A4-3})$$

Assuming that solution of the Equation A4-3 can be separated into time and spatial portions by:

$$v(x, t) = X(x)T(t) \quad (\text{A4-4})$$

Substituting this solution back into Equation A4-4 yields:

$$X(x) \frac{\partial^2 T(t)}{\partial t^2} - R_2^2 X(x)T(t) - a^2 T(t) \frac{\partial^2 X(x)}{\partial x^2} = 0 \quad (\text{A4-5})$$

Dividing by Equation $X(x)T(t)$ and separating the variables:

$$-\frac{\frac{\partial^2 T(t)}{\partial t^2}}{T(t)} = -R_2^2 - a^2 \frac{\frac{\partial^2 X(x)}{\partial x^2}}{X(x)} = \beta^2 \quad (\text{A4-6})$$

where β is a constant. Equation A3-6 can then be separated into two ODEs:

$$\begin{aligned} \frac{\partial^2 T(t)}{\partial t^2} + \beta^2 T(t) &= 0 \\ \frac{\partial^2 X(x)}{\partial x^2} + \frac{\beta^2 + R_2^2}{a^2} X(x) &= 0 \end{aligned} \quad (\text{A4-7 \& A4-8})$$

Define the constant k such that

$$k^2 = \frac{\beta^2 + R_2^2}{a^2} \quad (\text{A4-9})$$

Equation A4-8 becomes:

$$\frac{\partial^2 X(x)}{\partial x^2} + k^2 X(x) = 0 \quad (\text{A4-10})$$

The solution Equation A4-10 was derived previously in Appendix 4 for open-open boundaries:

$$X_n(x) = \sin(kx) \quad (\text{A4-11})$$

where:

$$k_n = \pm \frac{n\pi}{L} \quad (\text{A4-12})$$

But k was defined before in Equation A4-9. Rearranging and solving for β :

$$\beta^2 = \left(\frac{n\pi a}{L} \right)^2 - R_2^2$$

$$\begin{aligned}\beta^2 &= \omega_n^2 - R_2^2 \\ \beta^2 &= \omega_n^2 \left(1 - \frac{R_2^2}{\omega_n^2}\right)\end{aligned}\quad (\text{A4-13})$$

Solving the equation for time as in Appendix 4:

$$\frac{\partial^2 T(t)}{\partial t^2} + \beta^2 T(t) = 0$$

The nth solution for T(t) is

$$T_n(t) = A_n \cos\left(\pm \omega_n \left(1 - \frac{R_2^2}{\omega_n^2}\right) t\right) + B_n \sin\left(\pm \omega_n \left(1 - \frac{R_2^2}{\omega_n^2}\right) t\right) \quad (\text{A4-14})$$

Substituting A4-11 and A4-14 into Equation A4-4 results in:

$$v_n(x, t) = \sin(\pm k_n x) \left[A_n \cos\left(\pm \omega_n \left(1 - \frac{R_2^2}{\omega_n^2}\right) t\right) + B_n \sin\left(\pm \omega_n \left(1 - \frac{R_2^2}{\omega_n^2}\right) t\right) \right] \quad (\text{A4-15})$$

Substituting Equations A4-15 into Equation A4-2, the nth solution to the wave

Equation is:

$$p(x, t) = e^{-R_2 t} \sin(\pm k_n x) \left[A_n \cos\left(\pm \omega_n \left(1 - \frac{R_2^2}{\omega_n^2}\right) t\right) + B_n \sin\left(\pm \omega_n \left(1 - \frac{R_2^2}{\omega_n^2}\right) t\right) \right] \quad (\text{A4-16})$$

Equation A4-16 is the solution to Equation A4-1, the damped acoustic wave equation. This solution is in agreement with Dennemeyer (1968) and Weinberger (1965).

Appendix 5. Derivation of the Solutions for the Convective Wave Equation

In this appendix solutions for the convective wave equation will be derived. The convective wave equation can be derived by assuming constant axial mean flow, resulting in Equation 2-29.

$$\frac{\partial^2 p}{\partial t^2} + 2Ma \frac{\partial^2 p}{\partial x \partial t} - a^2 (1 - M^2) \frac{\partial^2 p}{\partial x^2} = 0 \quad (\text{A5-1})$$

When solving this equation we can use the previous solutions derived for the acoustic wave equation and the damped acoustic wave equation and the FRF results from the SIMULINK model to derive solutions. In the results from the SIMULINK model, as well as from Ingard () and Dowling (2003) the frequency of the resonant modes with convection takes the form:

$$\omega_{conv}^2 = \omega_n^2 (1 - M^2)$$

A separable solution, then, takes the form:

$$p(x, t) = e^{\pm \omega_n (1 - M^2) t} X(x) \quad (\text{A5-2})$$

Substituting Equation A5-2 with a positive exponent into A5-1 results in:

$$\begin{aligned} \omega_n^2 (1 - M^2)^2 e^{\omega_n (1 - M^2) t} X(x) + 2Ma \omega_n (1 - M^2) e^{\omega_n (1 - M^2) t} \frac{\partial X(x)}{\partial x} \\ - a^2 (1 - M^2) e^{\omega_n (1 - M^2) t} \frac{\partial^2 X(x)}{\partial x^2} = 0 \end{aligned} \quad (\text{A5-3})$$

Dividing by $e^{\omega_n (1 - M^2) t} X(x)$ results in:

$$\omega_n^2 (1 - M^2)^2 + 2Ma \omega_n (1 - M^2) \frac{\frac{\partial X(x)}{\partial x}}{X(x)} - a^2 (1 - M^2) \frac{\frac{\partial^2 X(x)}{\partial x^2}}{X(x)} = 0 \quad (\text{A5-4})$$

Rearranging and multiplying by $-X(x)/a^2(1-M^2)$:

$$\frac{\partial^2 X(x)}{\partial x^2} - 2M \frac{\omega_n}{a} \frac{\partial X(x)}{\partial x} - \frac{\omega_n^2}{a^2} (1-M^2) X(x) = 0 \quad (\text{A5-5})$$

Define:

$$k_n \equiv \frac{\omega_n}{a} = \frac{n\pi}{L} \quad (\text{A5-6})$$

Substituting Equation A5-6 into A5-5 results in:

$$\frac{\partial^2 X(x)}{\partial x^2} - 2Mk_n \frac{\partial X(x)}{\partial x} - k_n^2 (1-M^2) X(x) = 0 \quad (\text{A5-7})$$

Solutions to equation A5-7 are found by defining the characteristic equation of Equation A5-7. The characteristic equation is defined as:

$$n^2 - 2Mk_n n - k_n^2 (1-M^2) = 0 \quad (\text{A5-8})$$

Solving Equation 6-8 for n results in:

$$n = \frac{2Mk_n \pm \sqrt{(2Mk_n)^2 + 4k_n^2(1-M^2)}}{2}$$

Which reduces to:

$$n = Mk_n \pm k_n = k_n (M \pm 1)$$

$$k_x^+ = k_n (1+M)$$

$$k_x^- = -k_n (1-M)$$

Solutions to Equation A5-7 take the form:

$$X(x) = A_1 e^{k_x^+ x} + A_1 e^{-k_x^- x} \quad (\text{A5-9})$$

Substituting Equation A5-9 into Equation A5-2:

$$X(x) A_1 e^{k_x^+ x} + A_1 e^{-k_x^- x} \quad (\text{A5-10})$$

R70203480Z

Likewise the solution:

$$p(x,t) = e^{\omega_n(1-M^2)t} \left[A_1 e^{k_x^+ x} + A_2 e^{-k_x^- x} \right]$$

$$p(x,t) = A_1 e^{\omega_n(1-M^2)t + k_n(1+M)x} + A_2 e^{\omega_n(1-M^2)t - k_n^-(1-M)x} \quad (\text{A5-10})$$

Equation A5-10 can also be rearranged in the form:

$$p(x,t) = e^{-M^2 \omega_n t} \left[A_1 e^{\omega_n t + k_x^+ x} + A_2 e^{\omega_n t - k_x^- x} \right]$$

$$p(x,t) = e^{-M^2 \omega_n t} \left[A_1 e^{\omega_n t + k_n(1+M)x} + A_2 e^{\omega_n t - k_n^-(1-M)x} \right] \quad (\text{A5-11})$$